The Dissertation Committee for Colin Russell Heye
certifies that this is the approved version of the following dissertation:

Adaptive and Convergent Methods for Large Eddy Simulation of Turbulent Combustion

Committee:

Venkatramanan Raman, Supervisor

Noel Clemens

Ofodike Ezekoye

David Goldstein

Phillip Varghese

Adaptive and Convergent Methods for Large Eddy Simulation of Turbulent Combustion

by

Colin Russell Heye, B.S.M.E.

DISSERTATION

Presented to the Faculty of the Graduate School of

The University of Texas at Austin

in Partial Fulfillment

of the Requirements

for the Degree of

DOCTOR OF PHILOSOPHY

THE UNIVERSITY OF TEXAS AT AUSTIN

August 2014

Acknowledgments

There are many who have provided inspiration throughout my PhD studies. I first thank my adviser, Prof. Venkat Raman, for his unwavering support and continuous supply of opportunities to prove myself in the scientific community. I owe many of my unique and empowering collaborative studies to his willingness to send me to a number of conferences and workshops.

I would also like to thank my collaborators and colleagues. In particular, Dr. Colleen Kaul for her insights and continued discussion of advanced numerical methods for reacting flows, as well as Prof. David Blunck, Prof. Assaad Masri and their respective research teams for allowing me to leverage their expertise in experimental methods in order to gain insight into the complex physical processes at play in the configurations I aimed to investigate.

Finally, I thank my family and friends for their endless support throughout this process. You all have provided respite from and motivation to overcome my greatest challenges along the way. Of course, special mention goes to my parents who provided the means to pursue every opportunity I have ever desired.

Adaptive and Convergent Methods for Large Eddy Simulation of Turbulent Combustion

Publication No. _____

Colin Russell Heye, Ph.D.
The University of Texas at Austin, 2014

Supervisor: Venkatramanan Raman

In the recent past, LES methodology has emerged as a viable tool for modeling turbulent combustion. LES computes the large scale mixing process accurately, thereby providing a better starting point for small-scale models that describe the combustion process. Significant effort has been made over past decades to improve accuracy and applicability of the LES approach to a wide range of flows, though the current conventions often lack consistency to the problems at hand. To this end, the two main objectives of this dissertation are to develop a dynamic transport equation-based combustion model for large-eddy simulation (LES) of turbulent spray combustion and to investigate grid-independent LES modeling for scalar mixing.

Long-standing combustion modeling approaches have shown to be successful for a wide range of gas-phase flames, however, the assumptions required

to derive these formulations are invalidated in the presence of liquid fuels and non-negligible evaporation rates. In the first part of this work, a novel approach is developed to account for these evaporation effects and the resulting multi-regime combustion process. First, the mathematical formulation is derived and the numerical implementation in a low-Mach number computational solver is verified against one-dimensional and lab scale, both non-reacting and reacting spray-laden flows. In order to clarify the modeling requirements in LES for spray combustion applications, results from a suite of fully-resolved direct numerical simulations (DNS) of a spray laden planar jet flame are filtered at a range of length scales. LES results are then validated against two sets of experimental jet flames, one having a pilot and allowing for reduced chemistry modeling and the second requiring the use of detail chemistry with *in situ* tabulation to reduce the computational cost of the direct integration of a chemical mechanism.

The conventional LES governing equations are derived from a low-pass filtering of the Navier-Stokes equations. In practice, the filter used to derive the LES governing equations is not formally defined and instead, it is assumed that the discretization of LES equations will implicitly act as a low-pass filter. The second part of this study investigates an alternative derivation of the LES governing equations that requires the formal definition of the filtering operator, known as explicitly filtered LES. It has been shown that decoupling the filtering operation from the underlying grid allows for the isolation of subfilter-scale modeling errors from numerical discretization errors. Specific to combustion

modeling are the aggregate errors associated with modeling sub-filter distributions of scalars that are transported by numerical impacted turbulent fields. Quantities of interest to commonly-used combustion models, including sub-filter scalar variance and filtered scalar dissipation rate, are investigated for both homogeneous and shear-driven turbulent mixing.

Table of Contents

List of Tables

List of Figures

Chapter 1

Introduction

1.1 Simulation in Engineering Design

Turbulent reacting flows play an important role in the performance of a wide range of engineering devices, the analysis of which is required for effective design and production. With ever-increasing computational power comes the ability to simulate certain aspects of these flows as either a supplement or replacement for much more expensive experimental studies. These simulations, however, require the accurate characterization of flow physics that include length and time scales that span orders of magnitude as well as strong coupling between turbulent energy transfer and heat release due to chemical reactions.

In order to describe the different physical phenomena present in complex combustion devices a wide range of physical length and time scales must be accounted for. Approaches have been developed to include the full resolution of all turbulent scales, as in direct numerical simulation (DNS), or to truncate the range of resolved scales. These approaches require models to account for unresolved turbulent energy and fall into the category of either Reynolds averaged Navier-Stokes (RANS), where all turbulent scales are modeled, or large eddy simulation (LES), where large turbulent scales are resolved

and small scales with universal characteristics are modeled.

1.1.1 Direct Numerical Simulation

To avoid the need for averaging and approximations, the Navier-Stokes equations can be solved directly using DNS. However, due to prohibitive computational expense, applying this approach is feasible only for canonical configurations. For instance, the simulation of homogeneous turbulence requires on the order of $Re^{3/4}$ grid points in each direction, resulting in computational expense that scales as $Re^{9/4}$. Most practical applications involve high Reynolds number ($Re > 10^6$), leaving the range of length scales between combustor and Kolmogorov scale (smallest coherent turbulent structure) beyond the limits of current computational power. The use of liquid fuels and the presence of multiphase flows in these engineering applications complicates the concept of a fully-resolved simulation even further. There remains no clear definition of the smallest scales due to the internal flow within droplets of the dispersed phase and phase interface dynamics impacted by countering shear turbulence and surface tension.

1.1.2 Reynolds Averaged Navier-Stokes

The other extreme in simulating turbulent flows are the Reynolds Averaged Navier-Stokes (RANS) equations, in which flow realizations are ensemble averaged and additional transport equations for turbulent quantities are solved to provide closure. With the general approach including only the solution of

stationary mean flows as impacted by turbulent fluctuations, RANS methods have proven to be highly computationally efficient. By using RANS methods, however, one loses information about various unsteady processes such as separation. Phenomena involving high unsteadiness, including high vorticity flows and transient flows such as fuel injection encountered in liquid atomization and sprays, are typical areas where RANS methods are severely limited. The fundamental assumption of Reynolds-averaging (time- or ensemble- averaging), as well as the imperfections of models themselves ($k - \epsilon$ and problems with highly swirling flows for instance) remain significant sources of error.

1.1.3 Large Eddy Simulation

Alternatively, the turbulent flow field may be partially resolved using large eddy simulation (LES) techniques, where the large, energy containing scales are numerically resolved, whereas the effect of the small, unresolved scales, must be modeled. Theoretically, the LES formulation can be considered as a spatially filtered solution to the Navier-Stokes equation. In LES, the flow variables are decomposed into the sum of a resolved component and the residual sub-filter component. Thus the models incorporate the effect of unresolved scales on the resolved scale motion. Ideally, the filtering is applied in such a way that the sub-filter scales are universal in character [1] and carry only a small portion of the total turbulent kinetic energy, allowing for the development of reliable and widely applicable models. Due to the dependence of combustion and multi-phase dynamics on the large scale fluid-dynamic fields,

LES is expected to provide a more accurate solution than RANS at a much more reasonable computational cost than DNS.

1.2 LES of Reacting Flows

In turbulent reactive flows, it is the mixing of the reactants on the molecular level through diffusion that enables chemical reactions. Thus, due to the inherent lack of resolution of turbulent scales in either RANS or LES based simulations, the chemical source term must be modeled. The overarching goal in combustion modeling for LES is to accurately characterize the filtered chemical source term (reaction rate), which is strongly dependent on fluctuations in composition values at unresolved length scales. Thus, models account for the subfilter correlations of the thermo-chemical composition vector used to describe a set of chemical reactions. These correlations are generally described by a one-time one-point probability density function (PDF) for the composition values. Many approaches have been developed to locally determine the form of this distribution.

1.2.1 Laminar Chemistry Assumption

The simplest approach is to neglect the sub-grid scale fluctuations and assume perfect mixing below the filter scale. The filtered reaction rate can then be expressed purely in terms of filtered composition values. This implicitly assumes that the turbulent sub-grid time scales are much shorter than all of the chemical time scales. This may not be true in most combustion applications

and has been shown to produce significant errors [2].

1.2.2 Presumed PDF Approach

A widely used approach assumes the shape of the PDF, independent of local flow conditions. In the case of non-premixed combustion, where fuel and oxidizer are injected into a system separately, the steady laminar flamelet (SLF) approach [3, 4] can be used. This approach maps all thermo-chemical quantities of interest to a single conserved scalar known as the mixture fraction and its dissipation rate. In this way, only the joint subfilter PDF for mixture fraction and dissipation rate need to be determined. It has been shown that the marginal-PDF of mixture fraction is well-characterized by a beta-function [5] and the conditional-PDF of dissipation rate is generally assumed to be a delta-function. By limiting the mapping to low-order moments of the respective PDF's, the SLF approach provides a computationally efficient approach to accounting for turbulence-chemistry interactions and has been successfully validated against many experimental configurations [6, 7, 8, 9]. Note that validation is limited to cases containing mostly continuous flame fronts (i.e. minimal local extinction) and to quantities whose chemistry is relatively fast. These limitations have been previously investigated by Desjardin and Frankel [10] and Goldin and Menon [11].

1.2.3 Transported PDF Approach

For more complex flows involving slow chemistry, high Mach numbers or in this particular work, liquid fuels, the subfilter PDF of the thermochemical composition is unable to be determine *a priori*. Instead, a transport equation for the PDF can be used. Transport equations have been developed for a variety of joint PDF approximations, including velocity and composition [12, 13, 14, 15] as well as velocity, composition and frequency [16]. A general methodology that combines LES and the transported PDF approach was developed by Gao and O'Brien [17] for simulating reacting flow problems. This work involved further development of these methods for application to multiphase spray-laden reacting flows.

1.3 Sources of Error in LES

Errors and uncertainties in LES solutions generally come from one of two sources: numerical error and modeling error. Numerical error is rooted in the discrete approximations required to solve the non-linear Navier-Stokes equations. Whether it be the finite-differencing of a derivative or the truncation of an integral, the lack of an exact, continuous solution implies a lack of information. This error is present in single applications of a discrete approximation, though it can additionally compound or aggregate through the spatial and temporal evolution of a solution. Alternately, modeling errors are caused by assumptions made in defining a local or global description for non-linear flow behavior. Due to the need for computational efficiency, models are

required to be simplistic. As such, they must take advantage of universalities present in canonical flows and at asymptotically high Reynolds numbers, while the usage of these models to simulation practical engineering systems rarely abide by these constraints.

In order to address each of these sources of error independently, the current work is two-fold. The first portion investigates spray combustion applications and proposes a dynamic combustion model to account for the additional complexities imposed by local fuel evaporation. The second addresses the challenge of removing finite-differencing error from the solution of the Favre-filtered Navier-Stokes equations utilized in LES.

1.4 Dissertation Research Thrusts

1.4.1 LES of Spray Combustion Applications

Turbulent spray combustion is an integral part of liquid-fuel based combustion devices, in particular, aircraft engines. The dispersion, evaporation, mixing and combustion of fuel droplets in turbulent flows dictates the performance, efficiency, and emission characteristics of the device. The presence of liquid droplets alters the combustion dynamics, with multiple flame regimes possible depending on the local flow conditions and droplet distribution [18]. Further, the interaction of the droplets with gas phase is highly scale-dependent, and the dispersion of the droplets is strongly affected by the flame dynamics as well as the turbulent flow field [19]. Predictive computational models for such flows are indispensable for robust design and optimization,

particularly as new and varied fuels are beginning to emerge.

In LES, the large scale motions are directly evolved while small scale physics is modeled. A cut-off length scale, termed as the filter width, is used to demarcate the resolved scales from the unresolved small scales. Since turbulent combustion in practical devices, with or without sprays, occurs exclusively at scales close to the dissipation length scale, detailed sub filter models are required for describing the flame processes. Spray combustion models are typically derived from equivalent single-phase models. In LES, mixture-fraction based models, such as flamelet [20, 7, 21] or conditional moment closure [22, 23] have been commonly used due to their reduced computational cost. To account for the existence of the droplets, an extended flamelet approach has been proposed[24, 25], where a mixture-fraction/enthalpy formulation is used by remapping one-dimensional flamelet solutions in terms of an enthalpy-based progress variable [26]. Regardless of the combustion model used, a description of the subfilter scalar distribution through a one-point one-time probability density function (PDF) is necessary to obtain filtered LES fields [20]. While a beta-function could be used to model mixture fraction PDF in single-phase flows [5, 27], the presence of evaporating droplets render such simplifications invalid in two-phase flows [18]. The PDF associated with reacting scalars are highly flow-dependent, and cannot be presumed a priori.

An alternate approach to spray combustion modeling is the transported-PDF approach [15, 28, 29, 24, 30]. Here, a transport equation for the PDF of the variables used to describe gas phase combustion is evolved along with

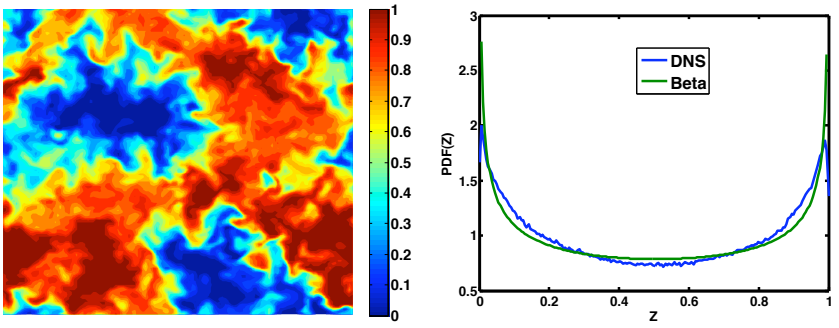

(a)

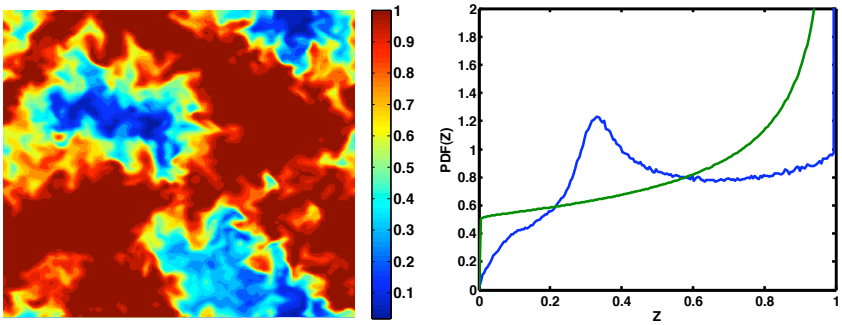

(b)

Figure 1.1: Instantaneous contours of mixture fraction (left) and associated distribution of values (right) from homogeneous mixing (a) without droplet evaporation and (b) with evaporation

the LES flow equations. This transported PDF approach could be coupled to a flamelet-based description of gas-phase [24] or the entire thermochemical composition vector could be used [29, 14, 13]. The transport equation for the gas-phase PDF of a single scalar in a two-phase flow has been formulated by Demoulin and Borghi [31] and Mortensen and Bilger [32]. In both these works, only the mixture-fraction PDF was considered. Demoulin and Borghi [31] obtain the PDF transport equation starting from the transport equation for

mixture fraction while Mortensen and Bilger [32] obtain the identical equation through a two-phase statistical representation. He and Gutheil [24] formulated a RANS/PDF approach for multiple scalars, along with a Lagrangian algorithm for solving the high-dimensional PDF transport equation. However, the PDF equation proposed in that work will not produce the correct transport equation for the scalar moments, which is crucial for consistency. Further, the use of the transported-PDF approach in LES requires special numerical considerations due to the inherent unsteadiness of the computations [21, 29, 28]. Jones and Sheen [33] developed a LES/PDF approach, where a single-phase stochastic approach is modified to account for spray source terms.

1.4.2 Numerical Error and Grid-Indepedence in LES

Although LES models have been widely used to simulate all regimes of combustion, there is considerable uncertainty in the simulations due to the link between LES filter width and grid size. LES is based on the concept of filtering, in which all scales larger than the filter width are considered resolved and directly solved on a computational grid whereas the small scales are explicitly modeled using the large scale information. While it is not difficult to define a filter width in theory, the practical implementation of this spatial cut-off is incredibly difficult and is the source of ambiguity regarding LES performance.

The governing equations of LES are derived by convolving the conservation equations with a low-pass filter kernel that contains the filter width as a parameter. In this sense, solutions to the filtered equations should not contain

scales smaller than the filter scale. These filtered equations are then discretized on a computational mesh, which introduces the grid spacing (grid size) as another parameter. In almost all LES applications, the filter width is taken to be identical to the grid size, leading to the grid-filtered LES formulation. Since scales smaller than the grid spacing cannot be resolved on these meshes, the use of the computational mesh acts as an effective filter. However, there are several issues that arise in this approach. First, numerical errors in the evaluation of gradients using finite differencing are higher at higher wavenumbers, which implies that scales close to the filter width, implicitly defined as the local mesh size, are severely contaminated. Since subfilter models routinely use gradient-based formulations, the performance of such models are suspect given these numerical errors [34, 35]. These errors are particularly detrimental in combustion applications, where key quantities such as scalar dissipation rate or scalar variance are modeled using the square of the scalar gradient [34].

Second, an important aspect of computational modeling is the demonstration of grid convergence, whereby the effect of numerical discretization is progressively reduced through refinement of the grid spacing. In grid-filtered LES, such refinement will also change the filter width, which is a physical model parameter, leading to a different range of scales being evolved. Consequently, conventional measures of grid convergence are not appropriate. This issue has several unintended consequences. For instance, validation experiments based on turbulent jets involve shear layers with large velocity and scalar gradients, where the grid is often refined in these regions in order to better capture the

strong gradients, effectively reducing the local filter width. Consequently, the importance of subfilter modeling itself diminishes. Since the focus of validation is in fact to test the subfilter models, this grid-filter link often reduces the strength of the validation tests, leaving the open challenge of separating the filter length scale from the grid spacing.

The filter width could be separated from the grid through two different approaches. In the first approach, the subfilter model is used to effectively damp scales below a cutoff length scale [36]. The subfilter models typically involve filter width as a parameter, and by specifying a value, the model could be made to act at the prescribed length scale. Due to the nature of the subfilter models, such increased dissipation will affect the resolved scales as well.

An alternate approach is to directly apply an explicit filtering operation at each time step to limit the range of scales in the solution [37, 38, 39]. Prior experience shows that applying this operation to terms in the evolution equation that generate small-scale energy is a better option than directly filtering the velocity or scalar fields [37, 40]. By properly constructing the explicit filter kernel, a ratio between the filter length scale and the grid size can be prescribed [37]. As this filter-to-grid ratio (FGR) is increased, the wavenumber content of filtered quantities is limited and finite differencing errors should decrease. Bose et al. [40] performed explicitly filtered LES of channel flow and demonstrated that as the FGR is increased, turbulent statistics converge. This behavior has been replicated in all other explicit-filtering studies. Brandt [41] observed that the use of explicit filtering increased the total error of the simulation with

regard to predicting the statistics of a comparable direct numerical simulation (DNS). In other words, as numerical errors were removed, the performance of the LES approach actually worsened.

Balaras et al. [42] combined explicit filtering with adaptive mesh refinement, which requires transfer of information between varying levels of grid refinement. The subfilter modeling was split into two components, the subfilter and subgrid terms. The subgrid terms are unresolvable and were modeled using conventional eddy viscosity type closure, while the subfilter resolved component represented the contribution from scales between the filter and grid scales. This latter component was modeled using a reconstruction approach. In general, it was observed that explicit filtering and reconstruction improved LES results. Radhakrishnan and Bellan [43] conducted explicit filtering analysis of a compressible temporal shear layer. This study confirmed that refining the grid independent of the filter quickly led to convergence. More importantly, it was found that different subfilter models exhibit different convergence behavior. For instance, certain models showed no appreciable change due to grid refinement while others showed very large changes. Radhakrishnan and Bellan [43] also conclude that the nature of the subfilter model for turbulent stresses is inconsequential as long as the model provides the right amount of energy dissipation at the small scales.

These studies, by and large, focused on the simulation of turbulent flows. Only the work of Radhakrishnan and Bellan [43] considers scalar transport in the form of energy transport equation since their formulation is based

on the compressible form of Navier-Stokes equations. However, this study is limited to understanding subfilter flux terms that appear in the energy equation. In combustion applications using LES, the use of conserved scalar models is very common. In this approach, a transport equation for the filtered mixture fraction along with models for subfilter variance and dissipation rate are solved. Prior studies [34, 35, 44] have indicated that most of these models are severely contaminated by numerical errors. The ability to mitigate this source of error through explicit filtering (or any other means) would be immensely useful from a practical standpoint.

1.5 Objectives

With this background, the focus of this work is two-fold. First, a consistent PDF transport equation is developed for multi-scalar problems. A Lagrangian solution methodology specifically suited for low-Mach number combustion is then formulated. This work is supported by fully-resolved verification studies as well as experimental validation. The work with explicitly filtered LES focuses on the evaluation of numerical errors in large eddy simulation of turbulent mixing. We use explicit filtering as a tool to understand the interaction of numerical errors with models for small scale mixing.

1.6 Outline

Based on this framework, the outline of the dissertation is as follows. Chapter 2 introduces the governing equations for multiphase flows and the

LES approximation and resulting model requirements. In Chapter 3, the development of the novel joint PDF transport equation is derived and verified for canonical configurations. Chapter 4 provides justification and verification of model requirements taken from a fully-resolved turbulent spray flame study, followed by the presentation of validation results of the LES/PDF solver in Chapters 5 and 6 for piloted and lifted experimental jet flames, respectively. Chapter 7 then elaborates on the modifications to the governing equations for explicitly filtered LES and explains the model development for this work. Chapter 8 then analyzes two sets of explicitly filtered LES results of scalar mixing, namely a homogeneous isotropic turbulence (HIT) configuration and a temporal shear layer, are considered. Finally, conclusions and future directions are discussed in Chapter 8.

Chapter 2

Development of a Joint-Scalar Transported PDF Model for LES of Spray Combustion

2.1 Transport Equations for Multiphase Flow

This chapter presents an overview of the governing equations and LES modeling requirements for spray-laden reacting flows. For multiphase flows, the Navier-Stokes equations are written as

$$\frac{\partial \rho}{\partial t} + \frac{\partial \rho u_j}{\partial x_j} = \dot{S}^m \tag{2.1}$$

$$\frac{\partial \rho u_i}{\partial t} + \frac{\partial \rho u_i u_j}{\partial x_j} = -\frac{\partial p}{\partial x_i} + \frac{\partial \tau_{ij}}{\partial x_j} + \rho g_i + \dot{S}_i^v \tag{2.2}$$

In these equations, ρ, u_i, p and g_i represent the density, velocity components, hydrodynamic pressure and gravitational body force, respectively. The evaporation mass and drag source terms are approximated as $\dot{S}^m$ and $\dot{S}_i^v$, though these terms are only valid in a spatially filtered sense as will be seen below. Viscous effects are accounted for in the transport of momentum through the term

$$\tau_{ij} = \mu \left(\frac{\partial u_i}{\partial x_j} + \frac{\partial u_j}{\partial x_i} \right) - \frac{2}{3} \mu \frac{\partial u_k}{\partial x_k} \delta_{ij} \tag{2.3}$$

where μ is the fluid mixture viscosity.

For reacting flows, species and enthalpy transport equations must also be considered. In the same framework, the species transport equation appears as

$$\frac{\partial \rho \phi_\alpha}{\partial t} + \frac{\partial \rho u_i \phi_\alpha}{\partial x_i} = \frac{\partial}{\partial x_i}\left(\rho D_\alpha \frac{\partial \phi_\alpha}{\partial x_i}\right) + \rho \omega_\alpha(\boldsymbol{\phi}) + \phi_\alpha^f \dot{S}^m \tag{2.4}$$

Individual species mass fractions are represented as ϕ_α with the associated reaction rate source term denoted as ω_α, which is itself dependent on the entire thermochemical composition, $\boldsymbol{\phi}$. This is assumed to abide by the Arrenhius formulation

$$\omega_m = W_m \sum_{k=1}^{M} \left(\nu''_{m,k} - \nu'_{m,k}\right) A_k T^{\alpha_k} \exp(-(E_k/R_u T)) \prod_{n=1}^{N} \left(\frac{X_n P}{R_u T}\right)^{\nu'_{n,k}} \tag{2.5}$$

The enthalpy transport equation is then considered in the form

$$\frac{\partial \rho \phi_h}{\partial t} + \frac{\partial \rho u_i \phi_h}{\partial x_i} = \frac{\partial}{\partial x_i}\left(\rho D_{th} \frac{\partial \phi_h}{\partial x_i}\right) + \rho \omega_h(\boldsymbol{\phi}) + \frac{Dp}{Dt} + \tau_{ij} S_{ij} + A(\boldsymbol{\phi}) + \dot{S}^h \tag{2.6}$$

Analogous to fluid viscosity, D and D_{th} represent the species and thermal diffusivities, respectively. The terms Dp/Dt and $\tau_{ij}S_{ij}$ represent the pressure derivate and viscous dissipation effects, while $A(\boldsymbol{\phi})$ represents differential diffusivity effects. In this work, a unity Lewis number assumption is imposed, implying that $D_\alpha = D_{th} = D$. In this limit, differential diffusion effects are negated. Energy source terms, including latent heat, due to fuel vaporization are denoted as $\dot{S}^h$.

2.2 LES Gas-Phase Transport Equations

In LES, the large-scale motions are resolved while the small-scale physics are modeled. Both spray-gas phase interactions and chemical reactions occur

at the small-scales and need to be exclusively modeled. Typically spray combustion is described by coupling a spray population tracking method to a turbulent combustion model [19, 45]. It should be noted that these models have been directly derived from the corresponding Reynolds-Averaged Navier-Stokes (RANS) approach based formulations. A Lagrangian approach [46, 47, 48, 19] is typically used to model the spray evolution. Turbulent combustion is currently modeled using single-phase models such as the flamelet model [4], conditional moment closure [49], surface-density model [50] or the linear-eddy model [45]. While most of these models are designed to handle a single combustion regime determined by the nature of fuel inflow, PDF methods can be applied to combustion in multiphase systems where multiple types of combustion are present. Below, the individual components, namely, the LES model, the spray population evolution, and the PDF model are described.

The basis of LES is the filtering operation that separates the large and small scales. For a variable-density flow, the Favre-filtering operation on a field variable, Q, is written as

$$\widetilde{Q}(\mathbf{x},t) = \frac{1}{\overline{\rho}} \int_{-\infty}^{\infty} \rho(\mathbf{y},t) Q(\mathbf{y},t) G(\mathbf{y}-\mathbf{x}) d\mathbf{y}, \tag{2.7}$$

where Q is the Favre-filtered variable, while ρ and $\overline{\rho}$ are the true and filtered densities, respectively. G is a filtering kernel that typically has finite spatial support, implying that the integration need to be carried out on a finite domain. Typically, the filtering kernel is assumed to be a box filter [51]. To obtain the LES equations of motion, this filtering operation is applied to the

momentum, continuity, and energy equations with added assumption that the filtering operation commutes with differentiation. The filtered continuity and momentum transport equations for two phase reacting flows can be written as

$$\frac{\partial \overline{\rho}}{\partial t} + \frac{\partial \overline{\rho}\widetilde{u}_j}{\partial x_j} = \overline{\rho}\widetilde{\dot{S}^m}, \tag{2.8}$$

where $\widetilde{u}_j$ is the filtered velocity component, and $\widetilde{\dot{S}^m}$ is the filtered mass source term ($\dot{S}^m$) that accounts for mass addition due to droplet evaporation. Numerical consideration of these filtered quantities will be discussed in Sect. 2.4.1.

$$\frac{\partial \overline{\rho}\widetilde{u}_i}{\partial t} + \frac{\partial \overline{\rho}\widetilde{u}_i\widetilde{u}_j}{\partial x_j} = -\frac{\partial \overline{p}}{\partial x_i} + \frac{\partial \mathcal{M}^u_{ij}}{\partial x_j} + \widetilde{\dot{S}^v_i}, \tag{2.9}$$

where $\mathcal{M}^u_{ij}$ denotes the sum of the modeled and resolved deviatoric components of the stress tensor, $\overline{p}$ denotes the sum of the filtered pressure and the isotropic components of the resolved and modeled stress tensor, and $\widetilde{\dot{S}^v_i}$ is the filtered i-th component of the force induced by droplet evaporation and drag on the gas phase.

The model quantity in the momentum transport equation, $\mathcal{M}^u_{ij}$ is exactly described as

$$\mathcal{M}^u_{ij} = \overline{\rho}(\widetilde{u}_i\widetilde{u}_j - \widetilde{u_i u_j}) \tag{2.10}$$

which is then closed using a Smagorinsky eddy-viscosity model

$$\mathcal{M}^u_{ij} - \frac{1}{3}\delta_{ij}\mathcal{M}^u_{kk} = -2\mu_t\left(\widetilde{S}_{ij} - \frac{1}{3}\delta_{ij}\widetilde{S}_{kk}\right) \tag{2.11}$$

where $\widetilde{S}_{ij}$ represents components of the Favre-filtered strain rate tensor and μ_t represents the turbulent viscosity, modeled as $\mu_t = C_s\overline{\rho}\Delta^2|\widetilde{S}|$. The coefficient C_s is determined locally using a dynamic scale similarity model [52].

In this formulation, the transport of species mass fractions and enthalpy appear as

$$\frac{\partial \overline{\rho}\widetilde{\phi}_\alpha}{\partial t} + \frac{\partial \overline{\rho}\widetilde{u}_i\widetilde{\phi}_\alpha}{\partial x_i} = \frac{\partial}{\partial x_i}\left(\rho D_\alpha \frac{\partial \widetilde{\phi}_\alpha}{\partial x_i}\right) + \overline{\rho}\widetilde{\omega_\alpha(\boldsymbol{\phi})} + \frac{\partial \mathcal{M}_j^{\phi_\alpha}}{\partial x_j} + \phi_\alpha^f \widetilde{\dot{S}^m} \tag{2.12}$$

$$\frac{\partial \overline{\rho}\widetilde{\phi}_h}{\partial t} + \frac{\partial \overline{\rho}\widetilde{u}_i\widetilde{\phi}_h}{\partial x_i} = \frac{\partial}{\partial x_i}\left(\rho D_{th} \frac{\partial \widetilde{\phi}_h}{\partial x_i}\right) + \overline{\rho}\widetilde{\omega_h(\boldsymbol{\phi})} + \frac{Dp}{Dt} + \tau_{ij}S_{ij} + \frac{\partial \mathcal{M}_j^h}{\partial x_j} + \widetilde{\dot{S}^h} \tag{2.13}$$

where $\mathcal{M}_j^{\phi_\alpha}$ and $\mathcal{M}_j^h$ are the subfilter scalar fluxes, modeled using a turbulent diffusivity analogous to the turbulent viscosity described above [53]. The subfilter contributions from the pressure derivative and viscous dissipation terms in Eq. 2.13 are neglected [54, 55, 56].

For applications in turbulent reacting flows, the closure of the chemical source term $\widetilde{\omega_\alpha(\boldsymbol{\phi})}$ proves to be the primary challenge due to the inability to characterize it purely based on the filtered composition quantities. Thus, the approach used here is to describe the subfilter distribution of species mass fractions according to a one-time one-point joint PDF. This novel approach for spray-laden flows is presented in Section 2.4.1.

2.3 Lagrangian Spray Model

In order to provide filtered evaporation source terms to the LES solver, a Lagrangian method is used to describe spray evolution, where the spray number density is evolved using a notional droplet ensemble [46, 47, 19]. Here, the notional droplets with weights corresponding to the mass of the droplets are injected into the computational domain. These particles carry droplet

property values and evolve in physical space using a set of ordinary differential equations[46]. The k-th notional particle in the ensemble carries a state-vector consisting of the position ($\mathbf{X}_k^p$), velocity ($V_{k,j}^p$), homogeneous temperature (T_k^p), and a size characteristic such as radius (R_k^p).

2.3.1 Droplet Momentum Transport Equations

In modeling the spray field, the assumption is made that the Kolmogorov scale is of the same order or larger than the largest droplets. Therefore, the interaction between the gas and liquid phases can be governed by laminar fluid dynamics and the spatial transport equations can be written as

$$\frac{d\mathbf{X}_k^p}{dt} = \mathbf{V}_k^p \tag{2.14}$$

$$\frac{dV_{k,i}^p}{dt} = \frac{1}{\tau_k}\left(\widetilde{u}_j(\mathbf{X}^p,t) - V_{k,i}^p\right) \tag{2.15}$$

where $V_{k,i}^p$ represents the $i-th$ component of the droplet velocity and $\widetilde{u}_j(\mathbf{X}^p,t)$ is the LES filtered velocity interpolated to the droplet location. The particle motion also exerts reverse force on the gas-phase evolution. This interaction appears as source terms in the gas-phase equations (Eq. 2.9). It should be noted that both the forward interpolation and the backward source term evaluation are computationally non-trivial. Here, we use the algorithm proposed by Reveillon and Vervisch [19]. The relaxation time τ_k is described by Faeth [57] as

$$\tau_k = \frac{1}{18}\frac{\rho_k^p (D_k^p)^2}{f_1 \mu_g} \tag{2.16}$$

where ρ_k^p is the liquid density, D_k^p is the respective droplet diameter and μ_g is the local gas phase viscosity. This includes a deviation from Stokes drag (f_1) related to the local blowing velocity [58]

$$f_1 = \frac{1 + 0.0545Re_k + 0.1Re_k^{1/2}\left(1 - 0.03Re_k\right)}{1 + a|Re_k|^b} \tag{2.17}$$

$$a = 0.09 + 0.077\exp(-0.4Re_k), \quad b = 0.4 + 0.77\exp(-0.04Re_k)$$

where Re_k is the droplet Reynolds number based on diameter and slip velocity. This timescale is a result of a spherical droplet drag assumption, made valid by the use of point particles and the use of fully atomized fuels. Additional forces, including Basset force and the Magnus effect, are neglected due to the relatively small droplet size and local volume fraction implied by the dilute spray combustion regime considered in this work.

2.3.2 Droplet Mass Transfer Equations

The governing equation for droplet mass conservation is given by

$$\frac{dm_k^p}{dt} = \dot{m}_k^p \tag{2.18}$$

$$\dot{m}_k^p = -\frac{Sh}{3Sc_g}\left(\frac{m_k^p}{\tau_k}\right)\ln(1 + B_M) \tag{2.19}$$

where $Sc_g = \mu_g/\rho_g$ is the local Schmidt number taken from the gas phase and Sh is the Sherwood number, empirically modified for convective corrections to mass transfer, given by

$$Sh = 2 + 0.552Re_k^{1/2}Sc_g^{1/3}. \tag{2.20}$$

The final term in Eq. 2.19, $\ln(1+B_M)$ represents the driving potential force for mass transfer (analogous to temperature difference for heat transfer). The Spalding transfer number for mass (B_M) is defined as

$$B_M = \frac{Y_s - Y_g}{1 - Y_s}. \tag{2.21}$$

with the free stream fuel mass fraction Y_g as interpolated from the LES solver and the fuel mass fraction at the droplet surface (Y_s), given by the equation

$$Y_s = \frac{\chi_s}{\chi_s + (1-\chi_s)\theta_2} \tag{2.22}$$

where χ_s is the fuel vapor mole fraction at the surface and $\theta = W_C/W_V$ is the ratio of molecular weights of the carrier gas species (subscript C) to the fuel vapor (subscript V). This vapor mole fraction is related to the saturation pressure P_{sat} through the Clausius-Clapeyron equation [59]

$$\chi_{s,eq} = \frac{P_{sat}}{\widetilde{P}_g} = \frac{P_{atm}}{\widetilde{P}_g} \exp\left[\frac{L_V}{\bar{R}/W_V}\left(\frac{1}{T_b} - \frac{1}{T_k^p}\right)\right] \tag{2.23}$$

where T_b is the droplet boiling temperature and $\bar{R}$ is the universal gas constant. This represents the entire evaporation model for the consideration of droplets in equilibrium (i.e. uniform internal temperature). Additional considerations have been proposed [60] and assessed in this work for non-equilibrium conditions. Many formulations of varying computational expense are available, however, for our purposes, the following description for a non-equilibrium vapor mole fraction is defined

$$\chi_{s,neq} = \chi_{s,eq} - \frac{L_K \beta}{D_k^p/2} \tag{2.24}$$

where L_K is the Knudsen layer thickness and β is a non-dimensional evaporation parameter, each given by

$$L_K = \frac{\mu_g \sqrt{2\pi T_k^p \bar{R}/W_V}}{Sc_g \widetilde{P}_g} \tag{2.25}$$

$$\beta = -\left(\frac{3}{2} Pr_g \tau_k\right) \frac{\dot{m}_k^p}{m_k^p} \tag{2.26}$$

These additional considerations are included by using $\chi_{s,neq}$ in Eq. 2.22.

2.3.3 Droplet Temperature Equations

Based on a uniform temperature model, the evolution of droplet temperature can be described by

$$\frac{dT_k^p}{dt} = \frac{f_2 Nu}{3Pr_g}\left(\frac{\theta_1}{\tau_k}\right)(T_g - T_k^p) + \left(\frac{L_V}{C_L}\right)\frac{\dot{m}_k^p}{m_k^p} \tag{2.27}$$

where $\theta_1 = C_{p,g}/C_L$ is the ratio of heat capacities for the surrounding gas and liquid fuel, T_g is the surrounding gas phase temperature, L_V is the latent heat of vaporization, and Nu is the gas phase Nusselt number, empirically correlated using

$$Nu = 2 + 0.552 Re_k^{1/2} Pr_g^{1/3} \tag{2.28}$$

The heat transfer correction coefficient, f_2 has been approximated in many ways [61, 62], however, the quasi-steady solution of the gas field equations coupled to the drop surface boundary conditions leads directly to an analytic expression for heat transfer reduction due to evaporation

$$f_2 = \frac{\beta}{e^{\beta} - 1} \tag{2.29}$$

giving a proper zero evaporation limit value of $f_2 \to 0$ as $\beta \to 1$.

Considerations for the contribution of droplet radiation on temperature evolution could also be considered. It has been shown [63] that even during exposure to extreme gas phase temperatures (¿ 2000 K), evaporation rates decrease by only 5%. While this may be relevant to more practical configurations, such as diesel engines and aircraft augmenters, the current studies are isolated to jet flames, where droplets rarely penetrate the fully-burning flame front. With this in mind, radiation effects have been neglected.

2.4 PDF Approach for Spray Combustion

In order to compute the filtered scalar composition, the one-point one-time PDF of the gas phase thermochemical composition is defined as a statistical quantity, obtained by averaging the one-point one-time distributions obtained from an ensemble of fully-resolved fields that have identical filtered LES fields. The PDF is defined as a mass density function [13, 14, 21, 29] as follows:

$$\overline{\rho}(\mathbf{x},t) = \int P(\boldsymbol{\psi},\eta;\mathbf{x},t)d\boldsymbol{\psi}, \tag{2.30}$$

where P stands for the one-time one-point joint PDF. $\{\boldsymbol{\psi},\eta\}$ denote the sample space variables corresponding to the random thermochemical composition vector $\{\boldsymbol{\phi},e\}$. The moments of the PDF provide filtered moments of the scalar composition. For instance,

$$\widetilde{\phi_\alpha^q \phi_\beta^r} = \frac{1}{\overline{\rho}} \int \psi_\alpha^q \psi_\beta^r P d\boldsymbol{\psi} d\eta, \tag{2.31}$$

where α and β denote components of the composition vector $\{\boldsymbol{\phi}, h\}$. Since the PDF itself is a function of space and time, and is highly problem dependent, it needs to be evolved along with the LES flow equations by solving a PDF transport equation.

2.4.1 Joint Scalar PDF Transport Equation

Details and derivation of the transport equation for the joint-PDF of the composition can be found in Appendix A. The exact PDF transport equation is then written as

$$\begin{aligned}
&\frac{\partial P}{\partial t} + \frac{\partial}{\partial x_i}\left(\widetilde{u_i|\boldsymbol{\psi}}, \eta P\right) = \\
&\quad - \frac{\partial}{\partial \psi_\alpha}\left(\left[\frac{1}{\overline{\rho}}\overline{\frac{\partial}{\partial x_i}\left(\rho D \frac{\partial \phi_\alpha}{\partial x_i}\right)|\boldsymbol{\psi}, \eta} + \omega_\alpha(\boldsymbol{\psi}, \eta) + (\phi_\alpha^f - \psi_\alpha)\dot{W}_c\right] P\right) \\
&\quad - \frac{\partial}{\partial \eta}\left(\left[\frac{1}{\overline{\rho}}\overline{\frac{\partial}{\partial x_i}\left(\rho D \frac{\partial \phi_\eta}{\partial x_i}\right)|\boldsymbol{\psi}, \eta} + \omega_e(\boldsymbol{\psi}, \eta) + (\dot{S}_c^e - \eta \dot{W}_c)\right] P\right) \\
&\quad + \dot{W}_c P. \qquad (2.32)
\end{aligned}$$

In the above equation, derivatives in physical space and time have been written on the left-hand side, whereas derivatives in sample space are on the right-hand side. Further, note that the reaction source term ω_α and ω_η are in closed form while all conditionally averaged terms now need to be modeled. The first of these terms is $\widetilde{\boldsymbol{u}|\boldsymbol{\psi}}, \eta$, and represents sub filter velocity-scalar correlations. A gradient-diffusion model has been used to describe the unresolved scalar flux component similar to single-phase flows [14, 21, 64], such that

$$\frac{\partial \widetilde{u_i|\boldsymbol{\psi}}, \eta P}{\partial x_i} = \frac{\partial \widetilde{u}_i P}{\partial x_i} - \frac{\partial}{\partial x_i}\left(\overline{\rho} D_T \frac{\partial P/\overline{\rho}}{\partial x_i}\right) \qquad (2.33)$$

where D_T is the turbulent diffusivity, thus providing the direct analogy to the LES filtered scalar transport equation.

The first term on the right hand side of Eq. 2.32 is conditional diffusion term for each species (and enthalpy variable), which can be further simplified as

$$-\frac{\partial}{\partial\psi_\alpha}\left[\frac{1}{\overline{\rho}}\overline{\frac{\partial}{\partial x_i}\left(\rho D\frac{\partial\phi_\alpha}{\partial x_i}\right)|\boldsymbol{\psi},\eta}\right]=\frac{\partial}{\partial x_i}\left(\overline{\rho}D\frac{\partial P/\overline{\rho}}{\partial x_i}\right)-\frac{\partial}{\partial\psi_\alpha}[(\widetilde{\mathcal{M}_\alpha|\psi_\alpha},\eta)P] \tag{2.34}$$

where $\widetilde{\mathcal{M}_\alpha|\psi_\alpha},\eta$ represents the modeled sub filter conditional mixing term. Models for this term are also called micro-mixing models, and have been the focus of research in PDF methods for single-phase flows [51, 65, 66]. Fox [67] provides a detailed discussion about subfilter mixing, and based on several physical requirements, specifies constraints that the corresponding models need to satisfy. While several micro-mixing models are available, none of the currently available models satisfy all of these constraints. One of the most widely used models for micro-mixing is the interaction by exchange with the mean (IEM) model [68, 14, 21, 65]. This model is used in the present work, where it assumes a linear relaxation of the scalar towards its mean value, written as

$$\widetilde{\mathcal{M}_\alpha|\psi_\alpha},\eta=\frac{C_\phi}{\tau_\phi}\left(\psi_\alpha-\widetilde{\phi}_\alpha\right), \tag{2.35}$$

where C_ϕ is a model parameter, τ_ϕ is a flow time-scale, and $\widetilde{\phi}_\alpha$ is the local filtered scalar value. Conditional diffusion can be similarly closed for the energy term. In addition to this term, the conditional evaporation terms $(\dot{W}_c,\dot{S}_c^e)$ will be modeled equal to the unconditional evaporation rate, which

in effect neglects the correlation between the gas phase species and spray evaporation. This is equivalent to a linear distribution of evaporated fuel to the gas phase based on the difference between the evaporated droplet composition and the local gas phase composition.

The final model terms in the PDF transport equation are $\dot{W}_c = \widetilde{\dot{S}^m|\boldsymbol{\psi}}$, representing the conditional evaporation rate. Similarly, the energy source term is also a conditional average, $\dot{S}_c^e = \widetilde{\dot{S}^e|\boldsymbol{\psi}}$. Approximations for this conditional source term are considered in two forms for this work. The first is termed unconditional evaporation, where it is assumed that $\widetilde{\dot{S}^m|\boldsymbol{\psi}} = \widetilde{\dot{S}^m}$ and that there is dependence on sub filter variations in composition. Secondly, conditional dependence can be implemented based on the local sub filter joint PDF. This approach is addressed in Sect. 5.1.2.

2.5 Numerical Implementation

The LES/FDF approach is a temporally accurate hybrid method that involves three different solvers that exchange mean field information at each time step. A flowchart of the solvers and the data exchanged is shown in Fig. 2.1.

The flows considered here fall in the low-Mach number regime but with variable density induced by boundary conditions and combustion-related energy release. Hence, a low-Mach number fractional time-stepping based LES solver is employed [69, 70, 26]. The essential components of the low-Mach number algorithm are the velocity advancement and pressure-based velocity

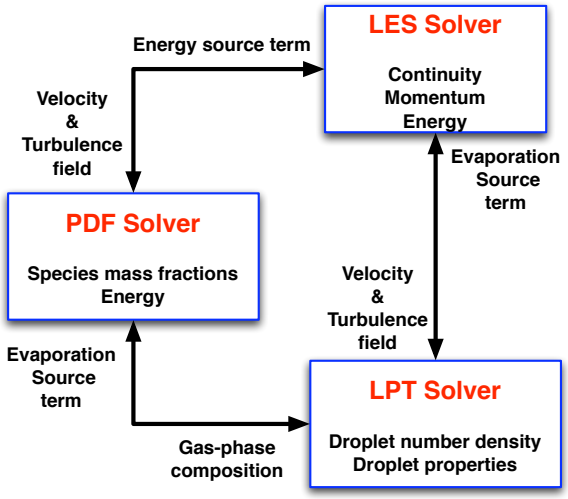

Figure 2.1: Flowchart showing the interaction of the three solvers used in the LES/PDF approach.

correction to enforce the continuity equation. In order to increase the time-step used, the viscous terms and the convection terms in the radial and azimuthal directions are treated implicitly [71]. To reduce computational expense, an iterative algorithm is used to solve the resulting nonlinear discretized equation [69, 70]. A second-order central scheme is used for spatial discretization, while a third-order upwinded scheme [72] is used to discretize the nonlinear terms in the scalar transport equations. Further details of the LES algorithm are provided in [71]. The turbulent diffusivity and viscosity terms are modeled using a dynamic Smagorinsky approach [53].

The droplet population is described using a Boltzmann-type equation governing dilute dispersed phase [73]. A Lagrangian method is used to solve this equation using a set of notional droplets [19, 74]. The droplet evolution

equations are solved using a third-order Runge-Kutta temporal scheme. The gas phase properties are interpolated on to particle locations using first-order linear interpolation scheme. The Lagrangian solver is advanced before the LES solver at each time step.

The high-dimensionality of the PDF transport equation renders conventional finite-volume/finite-difference type discretization approaches intractable. A variety of alternate methodologies including stochastic [15, 51, 14, 21, 29, 33] and deterministic [75, 56] approaches have been developed for single phase flows. The stochastic approach can be further divided into Lagrangian [14, 21, 76, 77] and Eulerian [78, 79] techniques. In this work, the Lagrangian Monte-Carlo approach is modified to consistently solve the PDF transport equation (Eq. 2.32).

The Lagrangian approach [15, 51] evolves an ensemble of notional particles using a specific set of stochastic differential equations. Each particle, i, in this ensemble carries a property vector consisting of weight (w_i), position ($\mathbf{x}_i$), composition ($\boldsymbol{\phi}_i$), and enthalpy (h_i) . The weight of the particle is determined in such a way that the sum of the weights of all particles inside a filter volume corresponds to the local gas phase density [15, 14, 21, 80].

$$\sum_{i=1}^{N} w_i = \overline{\rho}\nu, \tag{2.36}$$

where ν is the volume of the filter and N denotes the number of particles within a filter volume. It should be noted that N will fluctuate with time.

Similarly, the filtered scalar fields are obtained by a weighted average.

$$\frac{\sum_{i=1}^{N} w_i \boldsymbol{\phi}_i}{\sum_{i=1}^{N} w_i} = \widetilde{\boldsymbol{\phi}}. \tag{2.37}$$

In order to solve the PDF transport equation, stochastic differential equations are constructed that evolve the property vector in physical and composition spaces. While such equations are widely available for single-phase flows [15], special care is needed in developing equivalent equations for two-phase flows to account for the inter-phase mass transfer. The transport in physical space, which updates the position vector is described as follows [14, 15]:

$$d\mathbf{x}_i = \left[\widetilde{U}_i + \frac{1}{\overline{\rho}}\frac{\partial}{\partial x_i}\overline{\rho}(D + D_T)\right]\Delta t + \sqrt{2(D + D_T)}dW_i, \tag{2.38}$$

where Δt is the time step and dW_i is the Weiner diffusion term in the i-th direction. The velocity and diffusivity fields are obtained from the LES solver, and interpolated onto the particle location using a linear-interpolation algorithm.

The transport in composition space is through mixing, reaction, and evaporation. Similar to single-phase PDF approach, the mixing and reaction steps are described as follows:

$$d\boldsymbol{\phi}_i = \frac{1}{\tau}\left(\boldsymbol{\phi}_i - \widetilde{\boldsymbol{\phi}}_i\right)\Delta t + \mathbf{S}(\boldsymbol{\phi}_i)\Delta t. \tag{2.39}$$

Typically, a fractional time-stepping approach is used to separate mixing from reaction, and stiff ODE solvers are used to advance the composition due to the highly nonlinear reaction source terms [81, 82, 29].

The presence of the conditional evaporation source term ($\dot{W}_c$ in Eq. 2.32) requires additional equations to ensure that the weights and and scalar means evolve accurately. The discrete equations that need to be satisfied can be written as

$$\sum_{i=1}^{N} w_i^{n+1} - \sum_{i=1}^{N} w_i^n = \overline{\rho}\dot{W}_c \nu \Delta t, \tag{2.40}$$

and

$$\sum_{i=1}^{N} w_i^{n+1}\phi_{\alpha i}^{n+1} - \sum_{i=1}^{N} w_i^n \phi_{\alpha i}^n = \overline{\rho}\dot{W}_c \phi_\alpha^f \nu \Delta t, \tag{2.41}$$

where $\phi_{\alpha i}$ is the mass fraction of scalar α for the i-th particle. In order to satisfy the above equations and remain consistent with the higher moments of the filtered scalar transport equation (Eq. 2.4), the following evolution equations are proposed for the weights and the scalars.

$$w_i^{n+1} = w_i^n \left(1 + \frac{\dot{W}_c \nu \Delta t}{\sum_{i=1}^{N} w_i^n}\right), \tag{2.42}$$

and

$$\phi_{\alpha i}^{n+1} = \phi_{\alpha i}^n + \frac{w_i^n \dot{W}_c \nu \Delta t}{w_i^{n+1} \sum_{i=1}^{n} w_i^n} \left(\phi_\alpha^f - \phi_{\alpha i}^n\right). \tag{2.43}$$

In the limit of zero evaporation rate, the weights remain unaltered at each time step, while the scalar fields change only through mixing and reaction. Derivation of the filtered scalar moment equations can be found in Appendix B.

2.6 Verification Studies

2.6.1 1-D Evaporation Coupling Verification

The numerical implementation presented in the previous section is formulated for coupling with a low-Mach number, variable density flow solver. In

order to verify the approach and determine the convergence characteristics, a 1-D configuration with an analytic source term, analogous to evaporation, is tested.

The configuration consists of a unit length domain with a truncated Gaussian source term for both mass and scalar values, as seen in Fig. 2.2. Contuinity and momentum transport are solved in an Eulerian framework with pressure correction utilized to enforce mass conservation. Filtered scalar transport is solved using the proposed PDF transport equation and consistent evaporation source terms given in Eq. 2.42 and 2.43.

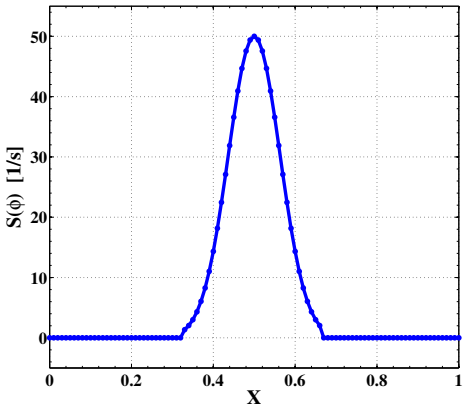

Figure 2.2: Mass and scalar source term for 1-D verification test case.

Two test cases are considered. The first proof of concept involves no convective transport and constant density, reducing the processes to diffusion and source terms. The resulting density and scalar fields are seen in Fig. 2.3. Due to the mass source term and the pressure corrective measures to enforce continuity, outward velocities are induced, driving particles away from the

central cells. Without the corrective terms for particle weight and scalar, the density as predicted by Eq. 2.36 is drastically under predicted. With the inclusion of the mass source term, the density resides within statistical error of the exact solution and the scalar values agree very well with the finite volume solution.

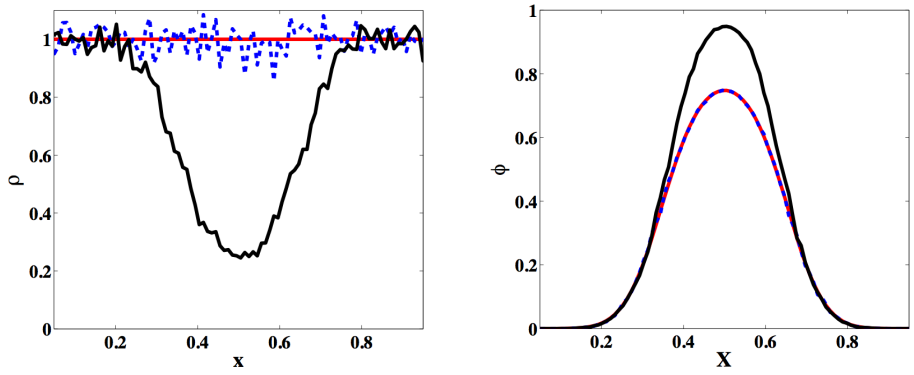

Figure 2.3: Density (left) and scalar (right) profiles for the isolated diffusion case. Lines indicate finite volume (red line), PDF solution without correction terms (black line) and PDF solution with correction (blue dashed line).

In order to address the converge characteristics of the numerical approach, a second test case includes convective transport of the notional particles. In this configuration, the source term continually generates an increase in value, but an asymptote appears as the outflow is reached as seen in Fig. 2.4. The PDF solution in this case is not nearly as accurate as in the previous result due to the combination of errors in both stochastic Weiner diffusion and the interpolation of filtered velocity values.

Figure 2.5 displays the rates of convergence for each of the three quantities of interest for this method: particle number density, grid size and time

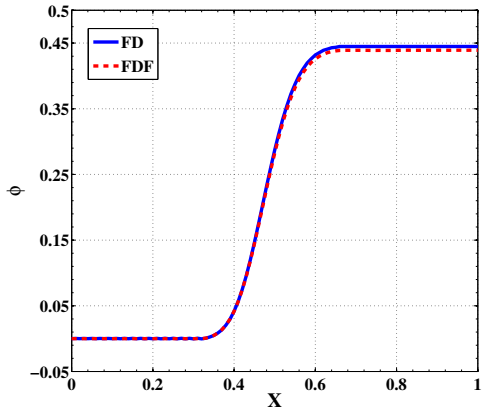

Figure 2.4: Scalar profiles for the convective test case from the finite volume (blue line) and PDF solution with corrective terms (red dashed line).

step. The errors are calculated for the scalar profile with respect to a highly-resolved finite volume result assumed to be the "true" solution. The order of accuracy for each quantity is as expected from previous studies with PDF methods of this nature [83, 84, 85]. For the convergence with time-step, fully-converged solutions did not show a change in error norm, thus an intermediate transient solution was required. The plateau in error with grid size comes from the coupled dependence of the finite volume momentum transport and the scalar evolution.

2.6.2 Finite Volume Simulation of a Spray-Laden Jet Flow

The Lagrangian approach for solving the PDF transport equation was verified using the spray jet experiment from University of Sydney [86]. The experimental setup consists of a turbulent droplet-laden jet issuing into a coflow. The liquid fuel (acetone) is atomized prior to injection and dispersed into the

air carrier stream. The liquid droplet loading is 5.2% of the carrier mass flow rate, which allows dilute spray assumptions to be valid. In the experiment, significant evaporation occurs before the jet exits the nozzle with only 16% of the fuel issuing in the droplet phase at the nozzle exit. A range of spray droplet sizes are observed with the biggest droplet class consisting of droplets with a mean size of 50 μm, which is significantly smaller than the LES grid size used.

The LES computation tracked the momentum and evaporated scalar mass fraction in the gas phase. The liquid phase was evolved using the Lagrangian particle tracking approach. The PDF method was also coupled to the LES solver, and evolves the scalar mass fraction. Since no chemical reactions are involved, the LES filtered mass fraction and the PDF-based filtered mass fraction should evolve identically, providing a means of verifying the PDF solver. All the equations are solved in cylindrical coordinate system. The computational domain extends 52D in streamwise direction, and 10.5D in the radial direction, where D is the diameter of the jet. The computational grid consists of $512\times160\times64$ points in streamwise, radial, and azimuthal directions, respectively. The jet nozzle is resolved using 24 uniform points in the radial direction. A separate periodic LES of a pipe flow is used to generate the inflow conditions. Instantaneous velocity planes from the fully-developed pipe flow is used to ensure that adequate temporal characteristics are supplied to the jet LES. The pipe flow is simulated by considering the net mass flow rate that includes both the carrier flow rate and the evaporated droplet

flow rate. This leads to a bulk velocity of 26 m/s in the simulations compared to the 24.815 m/s velocity based on the mass flow rate reported for the carrier phase in the experiments. The droplet size is prescribed based on a log-normal distribution with a mean of 9 μm and standard deviation of 8 μm. The PDF calculations used 10 particles per computational cell, with particle clustering/splitting techniques [21] used to control particle number density.

Figure 2.6 shows the streamwise velocity while Fig. 2.7 shows the RMS profiles in the radial direction for four different droplet classes defined by a mean droplet size. It should be noted that the droplet velocity is substantially different from the gas phase velocity even for the smallest droplets, indicating significant inertial effect. In general, the mean profiles are predicted well by the LES solver but the RMS velocities are lower across all droplet classes. The LES computations do not account for the subfilter scale effect of the turbulent flow on the droplets, which can introduce such deviations. Since the experiments themselves contain some amount of error, further analysis is required in order to understand the source of this discrepancy.

Figure 2.8 shows the instantaneous snapshot of mixture fraction from both the LES and PDF solvers. Both fields are nearly identical, indicating that the PDF evolution is accurate. It can also be seen that the mixture fraction is nonzero at the inlet, corresponding to the droplet evaporation inside the inlet nozzle. Figure 2.8 also shows the streamwise velocity superimposed with the droplet number density. It can be seen that the droplets persist until the end of the domain, indicating evaporation occurs over time scales

compared to the integral time scale in this particular geometry. Consequently, subfilter fluctuations in gas phase properties have only limited impact on the overall evolution of the droplets. This explains the good agreement between experiments and simulations even though the simulations neglect the subfilter effects. Figure 2.9 shows the time-averaged mean scalar profiles along the radial direction at different axial locations. Again, both the LES and PDF solvers produce nearly identical results. However, the RMS of scalar mass fraction is found to be significantly higher in the PDF results as compared to the LES data. Increasing the number of particles per cell in the PDF solver did not seem to affect the results. This indicates that although the instantaneous pictures look nearly identical, the PDF solution is numerically more diffusive in comparison with the LES solution.

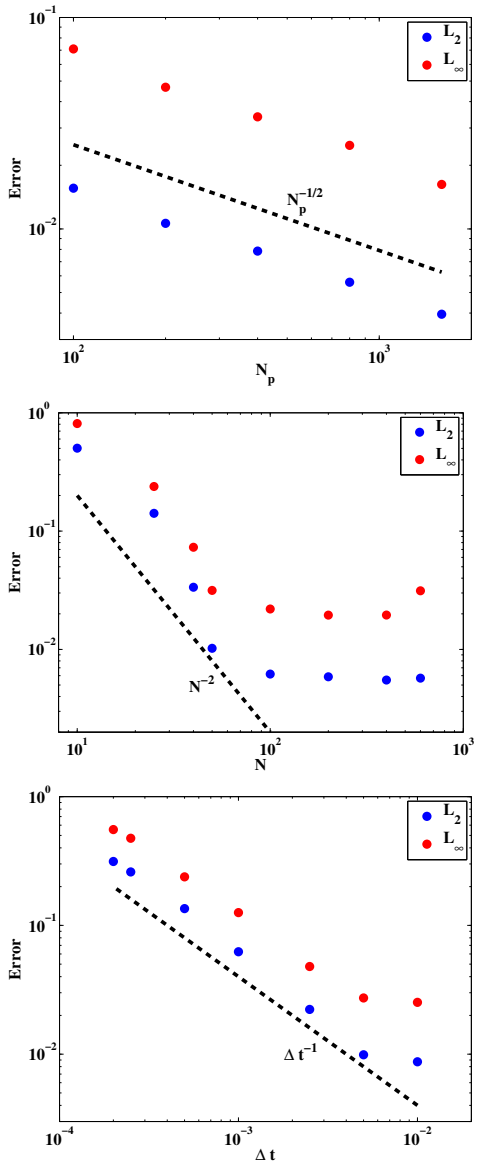

Figure 2.5: Convergence characteristics from the convective test case with respect to particle number density (top), grid cell size (middle) and time step (bottom).

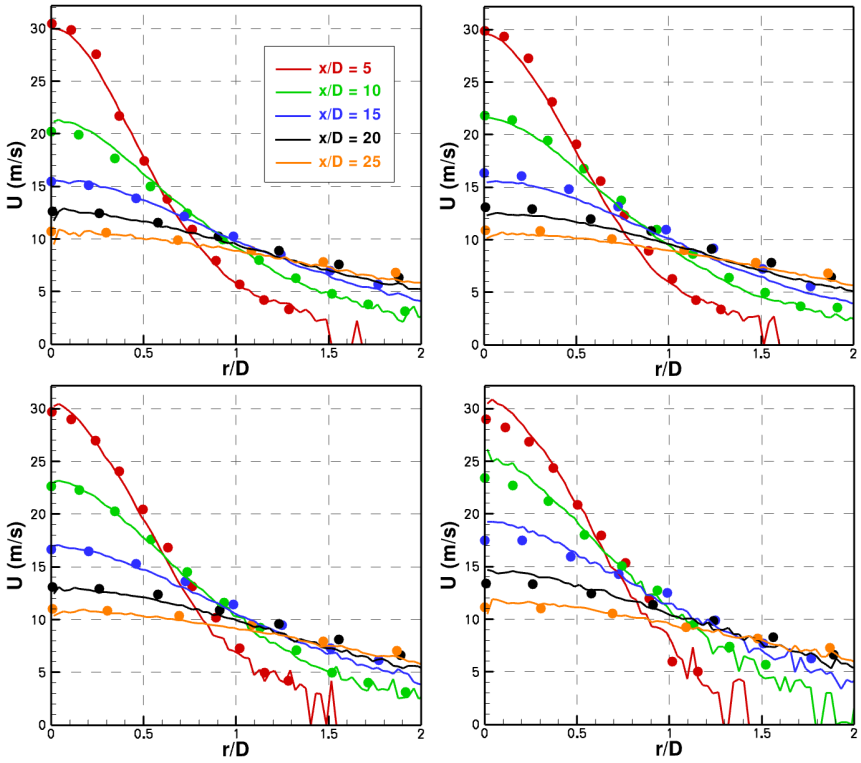

Figure 2.6: Mean streamwise velocity of different droplet classes for five different downstream locations compared to the experiment. (Top left) $d < 5\mu m$, (Top right) $10\mu m < d < 20\mu m$, (bottom left) $20\mu m < d < 30\mu m$, and (bottom right) $30\mu m < d < 40\mu m$. Computational results are plotted as solid lines, while measured values in the experiment are marked in symbols.

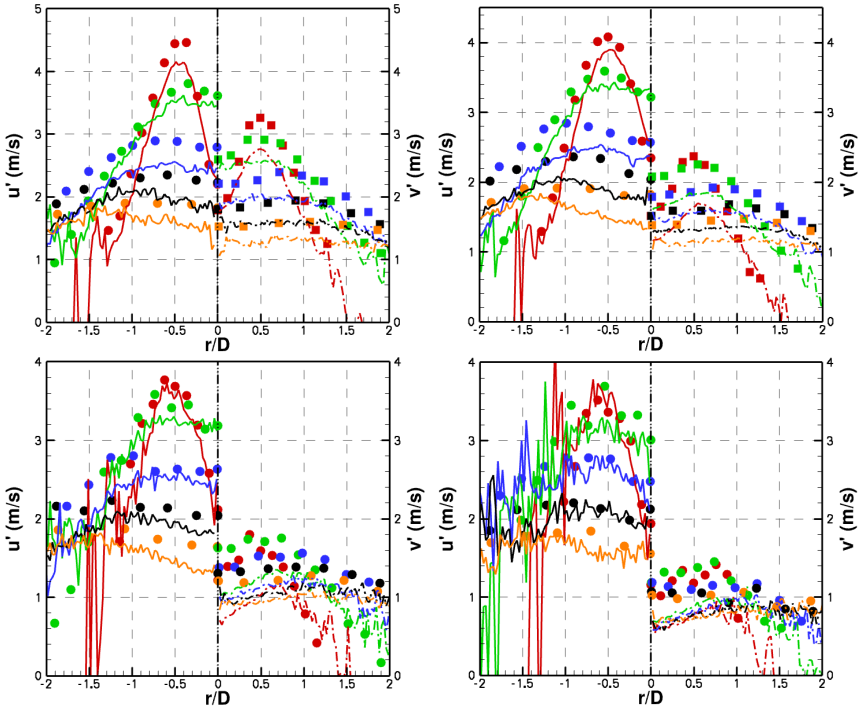

Figure 2.7: Rms velocity components in streamwise and radial directions of each droplet categories for five different downstream locations, compared to the experiment (symbols). (Top left) $d < 5\mu m$, (Top right) $10\mu m < d < 20\mu m$, (bottom left) $20\mu m < d < 30\mu m$, and (bottom right) $30\mu m < d < 40\mu m$.

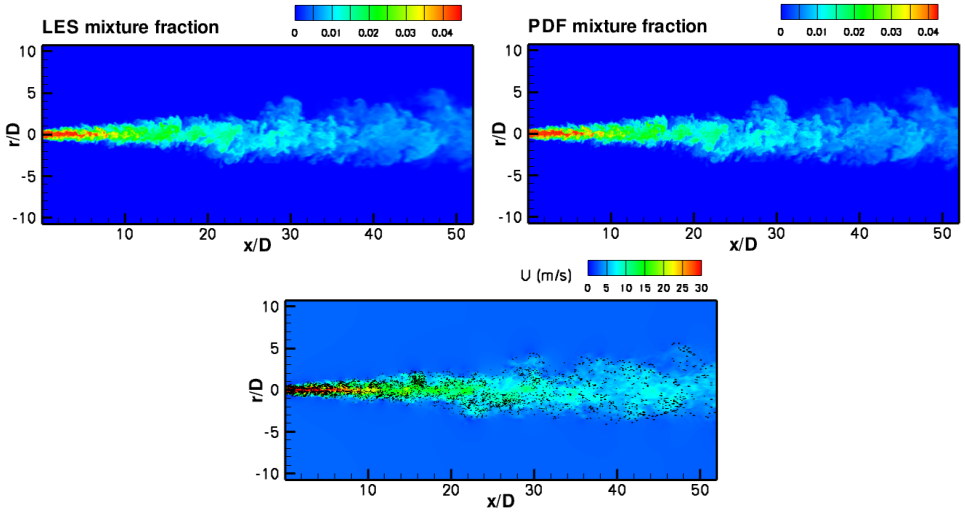

Figure 2.8: Instantaneous mixture fraction contours from (top left) LES and PDF (top right) methods. (Bottom) instantaneous streamwise velocity contour superimposed with droplet number density.

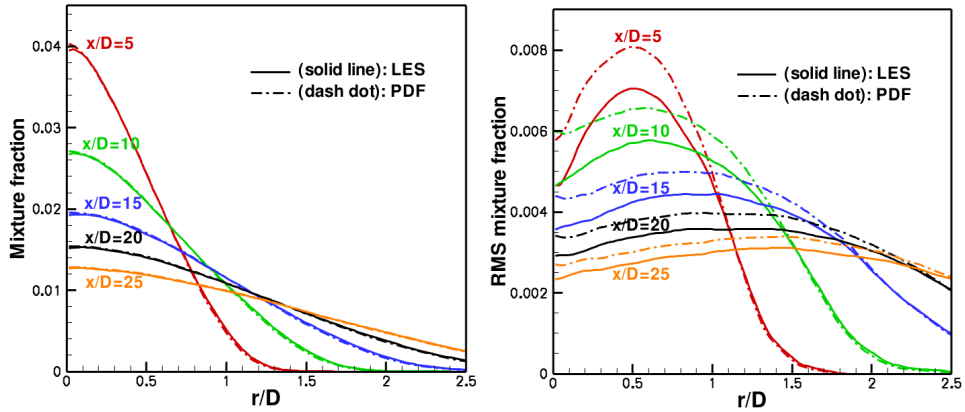

Figure 2.9: Mean (left) and RMS (right) of filtered mixture fraction from LES and PDF at different axial locations.

Chapter 3

DNS-based analysis of spray modeling issues

The PDF method described above does not require any closure for the chemical source term but the conditional mixing term needs to be modeled. In order to develop such models, fundamental insight into the spray combustion process is necessary. In this section, we discuss the development of two DNS databases, one for a fully gaseous flame and the other for a spray flame, and provide comparisons of the flame evolution for the two cases.

3.1 Database Construction

Two different DNS configurations are considered: 1) A gas phase piloted planar jet flame with n-heptane fuel issuing in gas phase into an air coflow and 2) a piloted planar jet spray flame with the same fuel issuing in the liquid phase. The configurations are designed in such a way that the mass flow rates of the fuel and oxidizer are identical in both cases. It should be noted that a similar set of configurations have been studied by Baba and Kurose [87]. A schematic of the DNS inflow configuration is shown in Fig. 3.1. The jet width, w_j, is 1.5 cm with pilot jets of width $0.1w_j$ on either side. The different streams are separated by walls with a thickness of $0.06w_j$. The

computational domain extends $20w_j$ in the streamwise direction, $15w_j$ in the jet-normal direction, and $2.56w_j$ in the spanwise direction. The computational grid contains $768 \times 512 \times 128$ points in the x,y, and, z directions, respectively. To resolve the shear layers, non-uniform grid spacing is used in the streamwise and jet-normal directions. Across the jet, 72 grid cells are used, and in order to resolve the smallest length scale in the shear layers, 14 cells are used across the pilots, with 10 cells across each of the wall dividers. The mean velocity of the main jet, $\overline{U}_j$ and pilot jets is 15 m/s, with the coflow velocity being $0.2\overline{U}_j$. The jet and coflow temperature, T_j, is 300 K. The pilot jet is considered to be a completely burnt mixture at $7.0T_j$. For the spray laden flames, a droplet mass flow rate of 8.64×10^{-3} kg/s was used to match the gas phase fuel flow, with a uniform droplet diameter of 29 μm. This equates to a total inflow mass loading of 0.5, which is relatively rich for a spray calculation, but should not create significant errors from unmodeled coalescence. To ensure the validity of the point particle assumption for fuel droplets, there must be an order of magnitude difference between grid size and droplet diameter. The smallest grid size to droplet ratio in this simulation is six in the near wall region of the main jet inflow, which is sufficiently large for this purpose. The simulations were carried out on 768 processors using MPI-based domain decomposition methodology.

The jet inflow conditions were generated using a separate DNS of a periodic channel flow configuration. Streamwise planes of data from this simulations were stored for sufficiently long durations and then fed as inflow profile

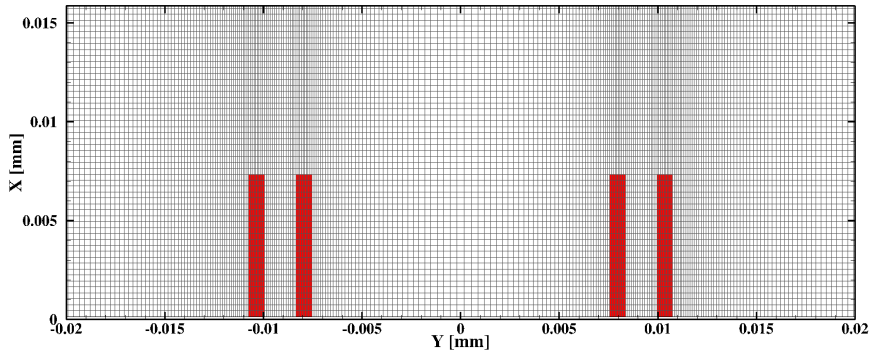

Figure 3.1: Wall configuration for piloted planar jet DNS simulation

for the main jet in the flame DNS. The coflow velocity profiles were assumed to have a prescribed mean turbulent profile with superimposed white noise fluctuations. For the spray flame, the periodic channel was simulated using a particle laden flow. This allowed realistic particle spatial distributions to be fed into the DNS domain. Fig. 3.2 shows an instantaneous image of droplet locations along with a vorticity magnitude isocontour colored by streamwise velocity in the boundary layer for the channel flow simulation.

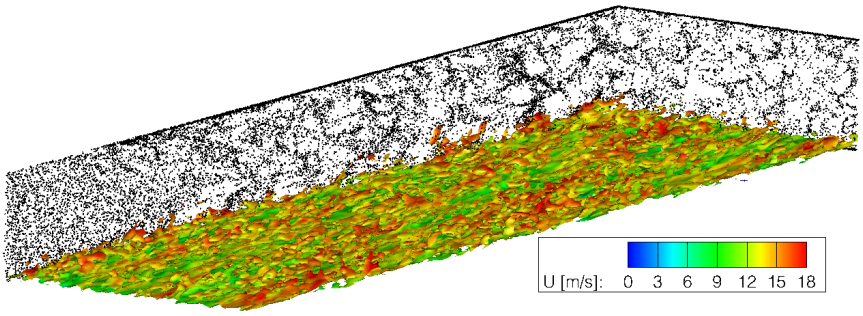

Figure 3.2: Auxiliary spray laden channel simulation for turbulent planar jet inflow

In both the gaseous and spray droplet fuel cases, the one step global reaction model was used to close the chemical source term in the transport equations. The reaction considered in this work is the oxidation of *n*-heptane, expressed as

$$C_7H_{16} + 11O_2 \rightarrow 7CO_2 + 8H_2O \tag{3.1}$$

Using the one step model, the chemical source term takes the form

$$\omega = AT^n \left(\frac{\rho Y_f}{W_f}\right)^a \left(\frac{\rho Y_o}{W_o}\right)^b \exp\left(-\frac{E}{\bar{R}T}\right) \tag{3.2}$$

where A is the Arrhenius coefficient, T is the local temperature, Y_f is the fuel mass fraction, W_f is the fuel molar mass, Y_o and W_o are the same values for the oxidizer, E is the fuel activation energy and $\bar{R}$ is the universal gas constant. The values a, b, and n are constant for a given fuel. In this work, the coefficients for *n*-heptane were adapted from Westbrook and Dryer[88], giving the values $A = 1.2 \times 10^9$ m^3/(mol $\cdot$ s), $E = 116.4$ kJ/mol, $a = 1$, $b = 1$, $n = 0$.

3.2 Flow Analysis

For the gaseous fuel case, the inflow fuel mass fraction is zero for both the coflow and pilot jets, while the main jet is specified to be unity. The mass fraction of oxidizer, in this case oxygen, for the coflow is 0.233 corresponding to that of air, and zero for the pilot and main jets.

Figure 3.3 shows instantaneous temperature contours from the four DNS computations. It can be seen that although the spray flames look similar

to the gaseous flame in terms of a primary flame region supported by the pilot, there are significant differences depending on the Stokes number of the droplets.

To further understand the flame evolution process, a normalized flame index [89] defined below is used:

$$\xi = \frac{\nabla Y_f \cdot \nabla Y_o}{|\nabla Y_f| \, |\nabla Y_o|}, \tag{3.3}$$

where ξ is bounded between -1 and 1. The flame index is defined only in regions of finite chemical reactions. As the value of ξ tends toward -1, the flame can be represented accurately as a diffusion flame, where the fuel and oxidizer are approaching the reaction zone from opposite directions. On the other hand, positive indicator function values represent premixed flame regions where the fuel and oxidizer are both approaching from the same side of the reaction zone.

Figure 3.4 shows the resulting contours for each case. In the case of the gaseous flame, a majority of the indicator function values tend to be negative, characteristic of a partially premixed flame, with a thin non-premixed interface between the fuel and coflow. In contrast, the droplets present in the two lower Stokes number cases result in a distinctly premixed inner region of the flame due to a time delay between evaporation and reaction that allows the carrier air and fuel to mix. Each has a non-premixed region similar to the gas phase flame surrounding the premixed zone, where the excess vaporized fuel penetrates the initial reaction zone and interacts with the outer coflow

air. Similar observations have been made by Luo, et al [18]. The third spray flame containing droplets with Stokes number of 10 has an entirely different dynamic. The most upstream portion of the flame is primarily non-premixed because the vaporized fuel has not yet had time to mix with the surrounding carrier air flow. Due to this reaction zone, part of the fuel has been removed from the flow and results in a complex core region of partially premixed flame.

It is interesting that the spray flame, which is essentially non-premixed at the inlet, actually displays a dominant premixed burning mode. But, a closer look at the conditional temperature data (Fig. 3.5) shows that the premixing mode is overstated by the indicator function. In a premixed combustion process, the conditional temperature plots will contain vertical lines corresponding to ignition across a flame front at constant equivalence ratios. As seen in Fig. 3.5, this feature is not commonly observed indicating the reactions are predominantly partially-premixed or that the equivalence ratio varies considerably in the domain. Although the PDF mixing models have been developed for strictly non-premixed flow configurations, application of these models to partially-premixed combustion has produced very accurate results [29]. Hence, these observations indicate that the PDF method is capable of handling spray combustion.

3.3 Conditional Diffusion Modeling

3.3.1 Micromixing Timescale

In developing the PDF transport equation (Eq. 2.32), the most important unclosed term is the conditional diffusion term, $\mathcal{M}_\alpha$. In general, this micromixing term is closed based on a mixing time scale (related to the scalar dissipation rate) and a shape function [67]. In the IEM model seen in Eq. 2.35, $\mathcal{C}_\phi$ is a model coefficient, τ_ϕ is a time scale determined based on the flow variables, and $\widetilde{\phi}$ is the local mean of the scalar within a filter volume. Below, we use DNS data to determine the evolution of the mixing time scale and the shape function.

In LES, the timescale τ_ϕ is often specified in terms of a turbulent-diffusivity based model [14, 13, 29]. Using the definition of the mixing timescale, the model coefficient for a non-reacting scalar such as mixture fraction can be defined as

$$C_\phi = \frac{\Delta^2}{D + D_t} \frac{\widetilde{\chi_\phi}}{\widetilde{\phi''^2}}, \tag{3.4}$$

where in this case Δ is the filter to grid width ratio while D and D_t are the scalar and turbulent diffusivity, respectively. $\widetilde{\chi_\phi}$ is the filtered scalar dissipation and $\widetilde{\phi''^2}$ represents the subfilter scalar variance. Consequently, the model coefficient is sensitive to the filter width, the chemical reactions that a scalar undergoes, and the distribution of length scales within the filter volume relative to the turbulence length scales.

Figure 3.6 displays calculated values of the micromixing model coefficient for mixture fraction in each individual flowfield. A filter-width to grid

ratio of four is used to obtain this data. In general, the coefficient values increase with an increase in Stokes number. It can be noticed that the coefficient relaxes to the gas phase flame values near the outer flame location, indicating that the spray flames exhibit partially-premixed behavior once the spray droplets have fully evaporated. In addition, while the vast majority of the values in the gas phase flame lie in the commonly used range between 2 and 10, there is a significant portion of the mixing zone that is well beyond these conventional values. This indicates that a constant specified value for the model coefficient is not a valid assumption, especially as larger droplets are considered in spray laden flows.

3.3.2 Mixing Dependencies

The second part of the mixing model is the shape function. The IEM model (Eq. 2.35) makes the assumption that the scalars relax towards the mean linearly. This term was investigated using the exact conditional diffusion term evaluated for different filter widths. Figures 3.7a-c show the conditional diffusion term for the unity droplet Stokes number spray flame. In each plot, the vertical dashed red line indicates the mean subfilter value. In the region close to the jet exit, the large gradients in the mixture fraction value due to strong droplet evaporation leads to a wider range in the conditional diffusion values. As the gradients are slowly destroyed, this term becomes smaller downstream. Most importantly, there is a significant linear region where the IEM model is expected to be valid. However, strong curvature of this term is noticed near

the end values for the range of mixture fraction present in the flow. In the case of the temperature scalar values, similar trends should be observed, leaving significant model errors at the higher values in the reaction zone. The impact of the linearity assumption will be assessed next using *a posteriori* comparison with DNS data.

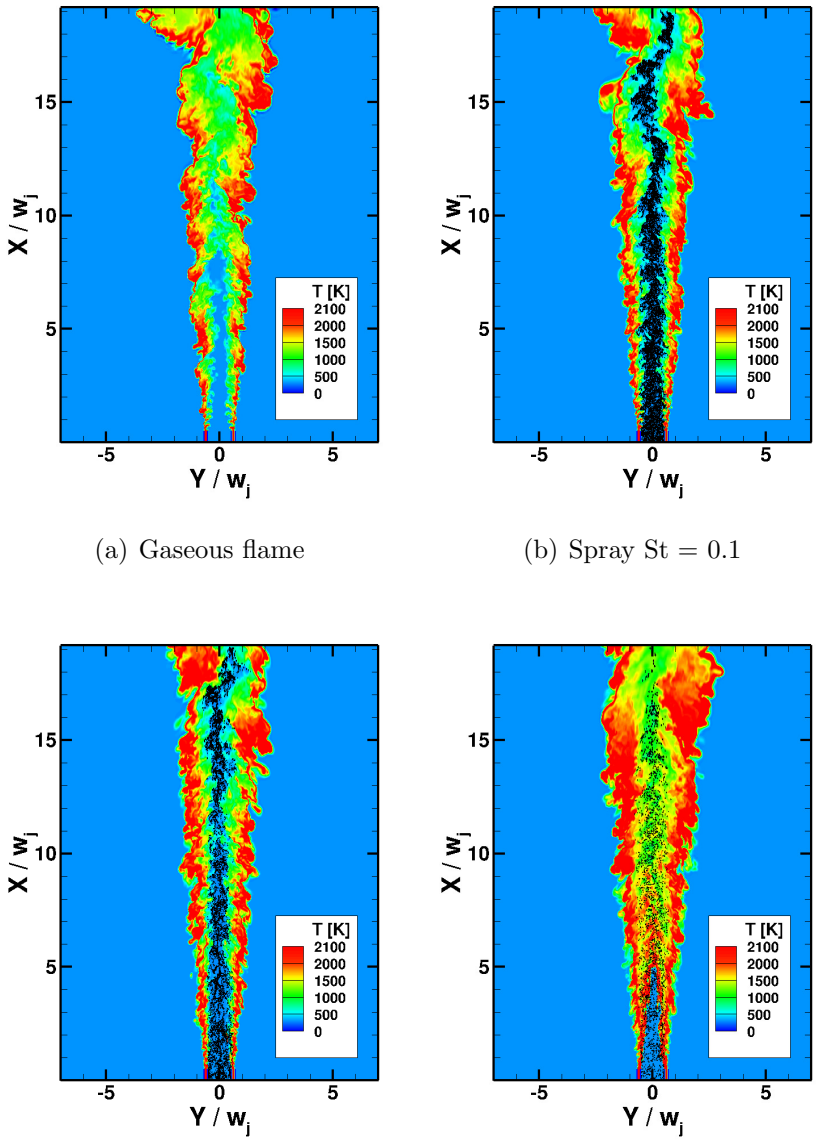

(a) Gaseous flame

(b) Spray St = 0.1

(c) Spray St = 1

(d) Spray St = 10

Figure 3.3: Instantaneous temperature contours with superimposed particle locations for spray cases

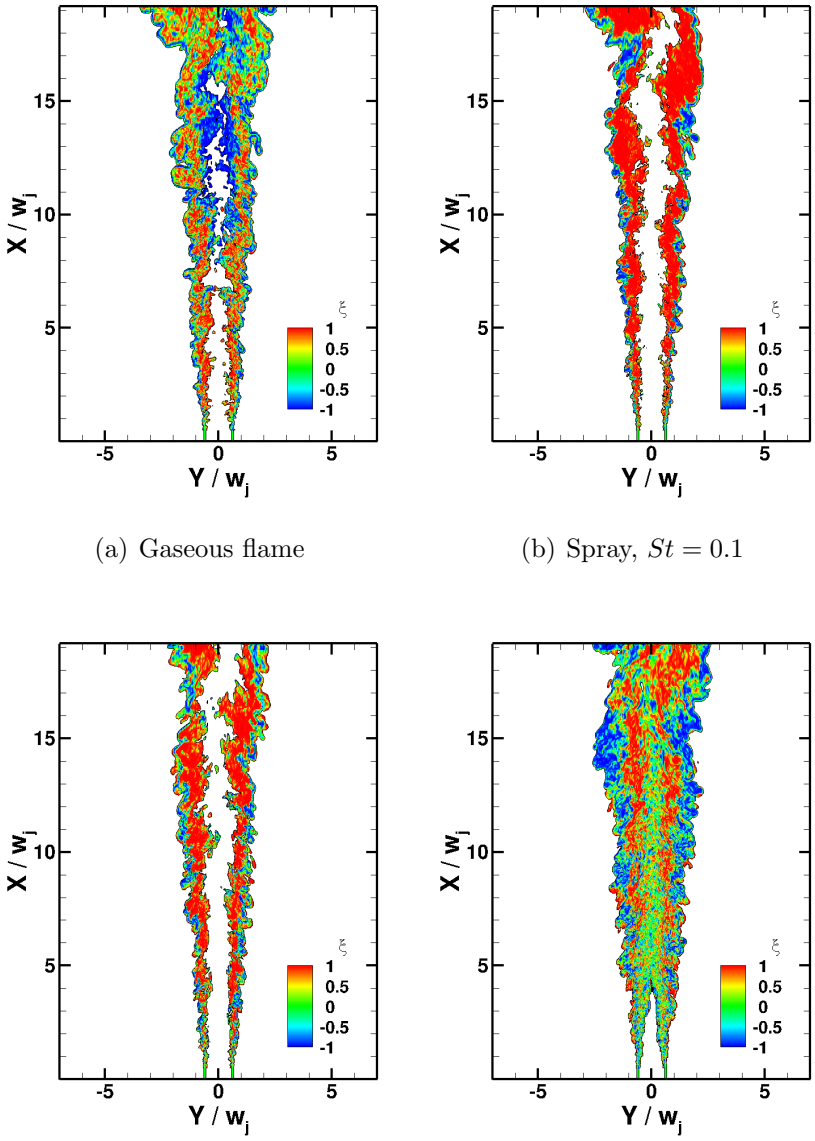

(a) Gaseous flame

(b) Spray, $St = 0.1$

(c) Spray, $St = 1$

(d) Spray, $St = 10$

Figure 3.4: Instantaneous contours of indicator function in regions of significant chemical source term

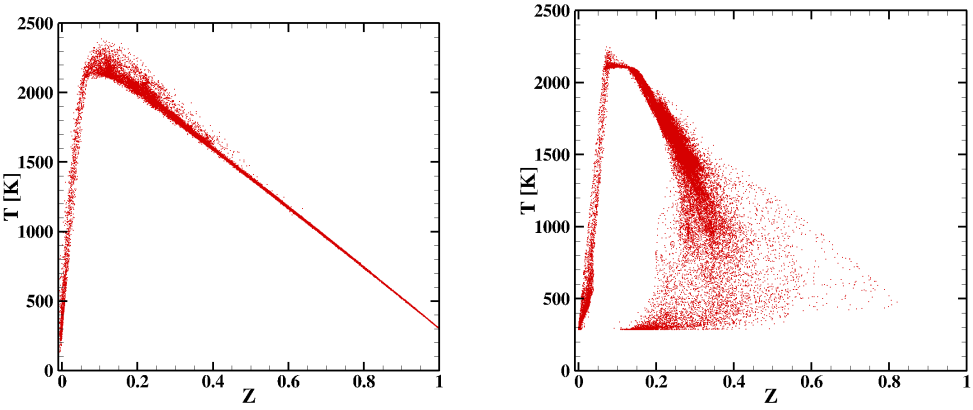

(a) Gaseous flame

(b) Spray flame, $St = 1$

Figure 3.5: Distributions of temperature conditioned on mixture fraction at a streamwise location of $10w_j$

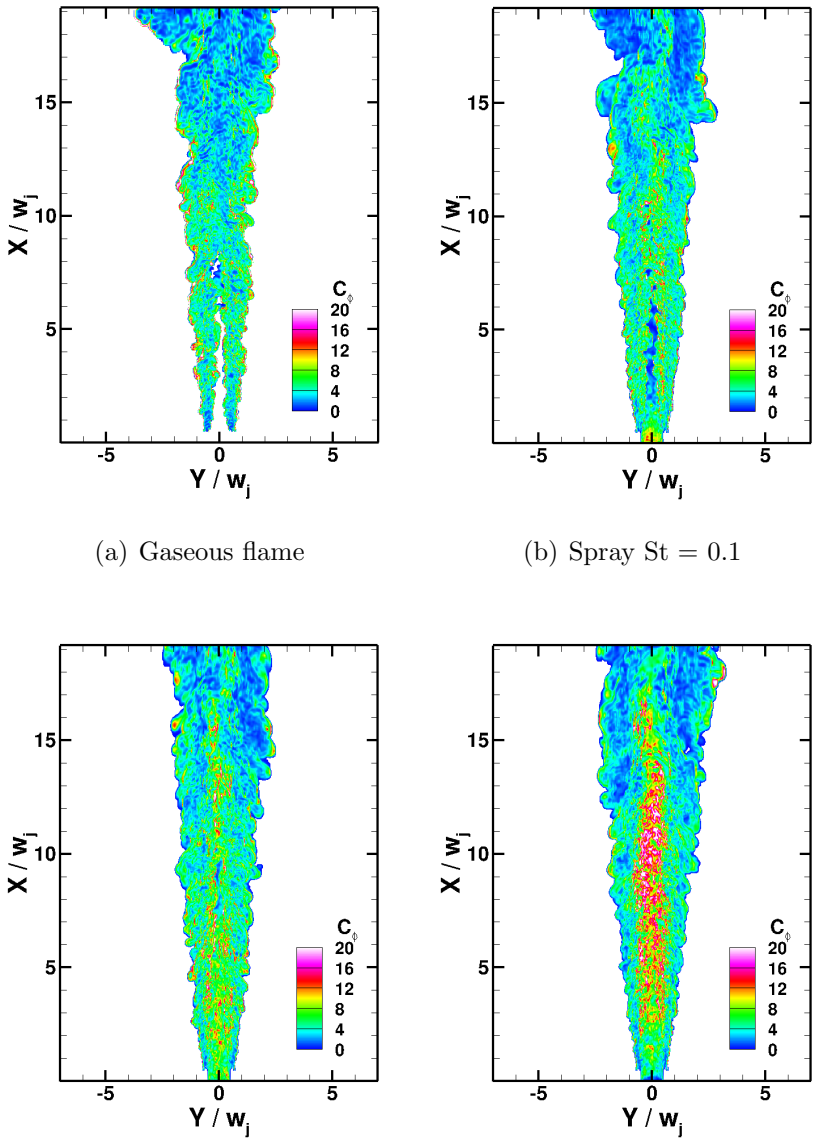

(a) Gaseous flame

(b) Spray St = 0.1

(c) Spray St = 1

(d) Spray St = 10

Figure 3.6: Contours of C_ϕ for gaseous fuel and various Stokes number spray-based fuel

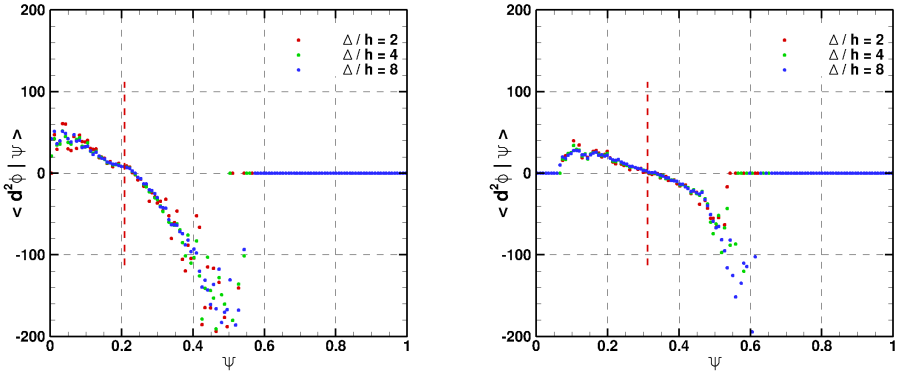

(a) $x/w_j = 1$ (b) $x/w_j = 5$

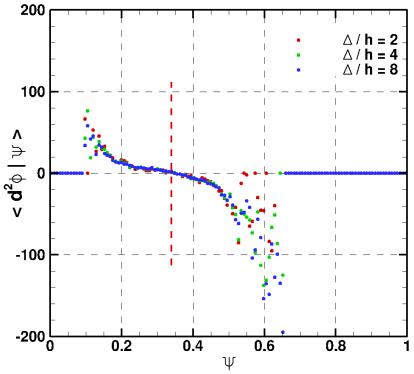

(c) $x/w_j = 10$

Figure 3.7: Conditional diffusion of mixture fraction in the spray flame with St = 1 at various downstream locations plotted for a range of box filter to grid width ratios

Chapter 4

LES/PDF Simulation of a Piloted Ethanol Spray Flame

4.1 Experimental Setup

The first set of validation results come from a family of piloted spray flame experiments performed at the University of Sydney [90, 91][1]. The burner used in these experiments can be seen in Fig. 4.1, where a nebulizer is used to atomize droplets using an air stream that is then carried through a 210 mm pipe into the combustion domain. This allows for vaporization of fuel to occur well before the mixture is exposed to a heated, combustion driven environment. After the pipe flow and nozzle exit, a pilot encircles the core jet as well as a low velocity co-flow to ensure downstream containment. Measurements for these flames are only made downstream of the nozzle exit. This causes some concern with the lack of information at the upstream end of the pipe other than global mass flow rate quantities.

In total, eight flow conditions were investigated in these experiments. Figure 4.2 shows the variations considered, namely fuel and carrier mass flow rates in the core jet flow. The right hand plot in this figure displays the

[1]This work has been previously published [102]. Credit to Venkatramanan Raman for his advisory contributions and Assaad R. Masri for providing experimental data for validation.

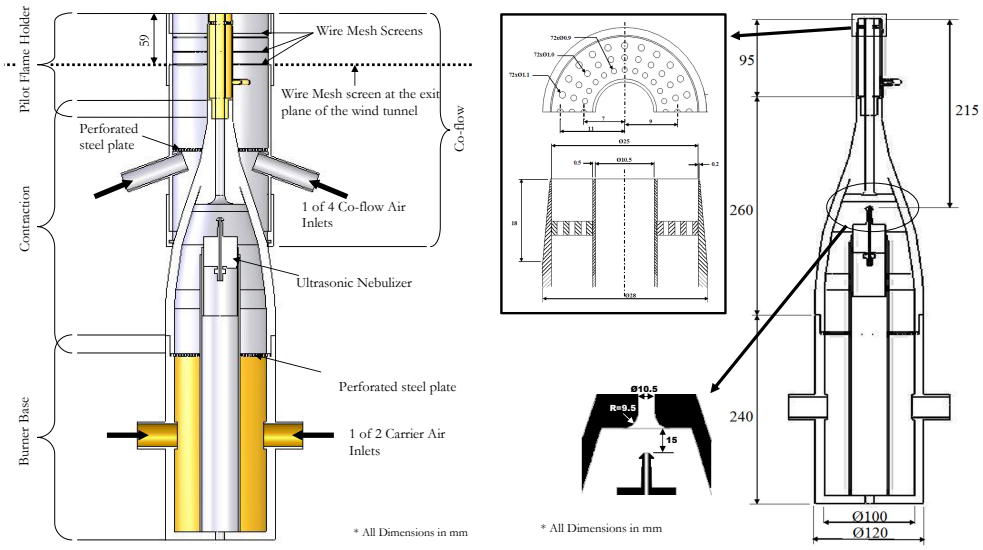

Figure 4.1: Experimental nozzle configuration for piloted spray jet flames used for validation.

resulting flame lengths as a function bulk jet velocity. It is seen by comparing the two plots that for constant velocity, the flame length is relatively robust with respect to fuel mass loading. Increasing the fuel loading, and in turn the overall equivalence ratio, the flame shows a clear extension. These statements are qualitatively confirmed by the images shown in Fig. 4.3.

For the results below, only a select number of flames will be presented, which capture both the Reynolds number and mass loading variations spanned by the experimental efforts. The parameters for the particular flames to be studied using the LES/PDF approach are given in Table 4.1.

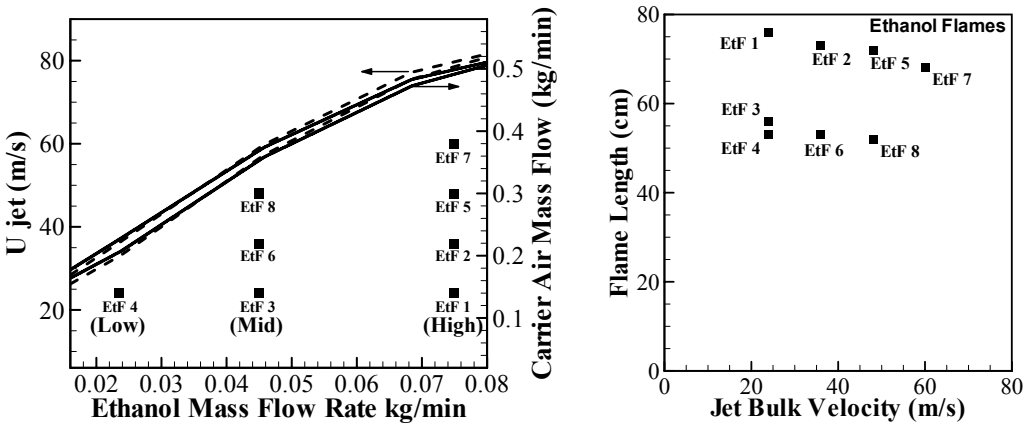

Figure 4.2: Experimental flow rate parameters (left) and the resulting flame lengths

Table 4.1: Ethanol spray jet flame conditions.

Parameter	EtF1	EtF2	EtF6
Bulk velocity (m/s)	24	36	36
Carrier flow rate (g/min)	150	225	225
Liquid injection rate (g/min)	75	75	45
Measured liq. at exit (g/min)	45.7	66.6	41.3
Spray jet density (kg/m^3)	1.60	1.56	1.42
Jet Reynolds number	22525	30661	27422

4.2 Simulations Details

The ethanol spray flame experimentally studied at the University of Sydney [90] will be used to demonstrate the LES-PDF approach. Figure 4.4 shows the simulation domain and the inflow configuration. An acetylene/hydrogen/air pilot is used to stabilize the flame.

The computational grid consisted of 256 x 192 x 64 points in a cylindrical coordinate frame. A separate periodic pipe flow simulation of the gas phase

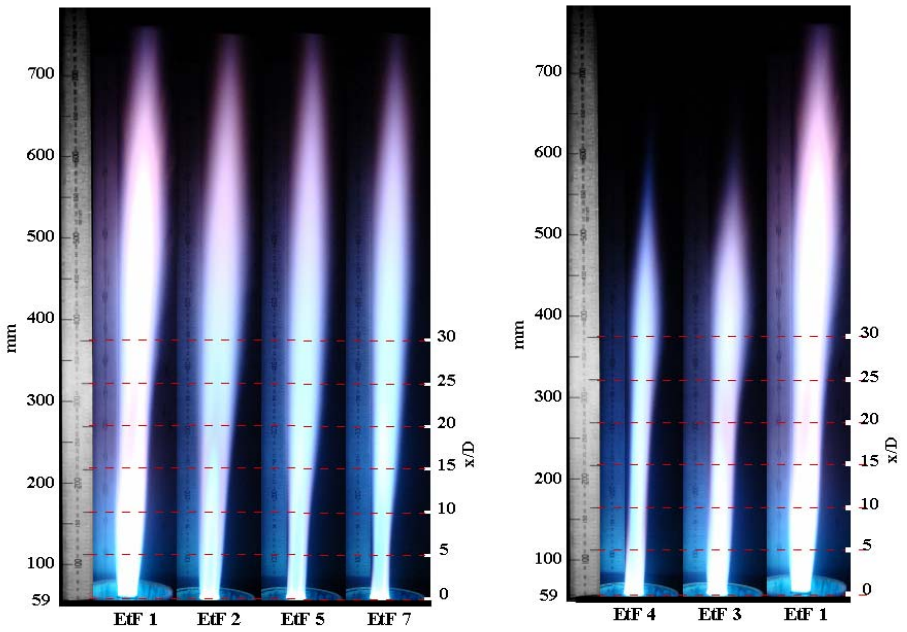

Figure 4.3: Pictures from spray flame experiments. Flames are grouped by progressively increasing core jet air flow rate (left) and core fuel mass loading (right). Demarcations denote millimeters downstream of the nozzle exit.

was used to develop time-correlated turbulent inflow for the droplet-laden jet and the pilot stream. Partial evaporation of the droplets in the pipe alters the bulk velocity (28 m/s as opposed to the air flow rate of 24 m/s for case EtF6). The coflow was specified based on a mean flow obtained from experiments. Fluctuations were not superimposed on the coflow. Droplets were injected uniformly across the pipe inflow with the diameter randomly generated using a log normal distribution with mean diameter of 25 μm and a standard deviation of 15.81 μm. The diameter distribution was fitted to experimental measurements at the nozzle outflow ($x/D = 0.3$).

The flamelet table for ethanol combustion uses a 50 species 235 reaction mechanism [92]. While the outflow from the auxiliary pipe simulation provides the mixture fraction field at the nozzle exit, both mixture fraction and progress variable values must be specified for the pilot and coflow. These values, ($\{Z_{in}, C_{in}\}$) are set to $\{0.105, 1\}$, corresponding to stoichiometric conditions. The coflow is set to $\{0, 0\}$.

The PDF transport equation was solved using a Lagrangian Monte Carlo approach initialized with 20 notional particles in each cell. To ensure accurate closure of the joint PDF, particle counts were constrained to a minimum of 10 particles/cell and maximum of 30 particles/cell, enforced using merging and splitting techniques [21]. During the simulation, the total number of particles in the domain was approximately 150 million. Simulations were carried out using MPI-based parallelization on 256 cores. Statistics were collected over 5 flow-through times after reaching statistical stationarity.

4.3 Results and Discussion

4.3.1 Flame Length

The global parameter for these flames is the length as determined by significant chemiluminescence. Defining this in a simulation can be challenging due to the use of radicals for indicators, though the correlation between stoichiometric conditions and radical generation is a valid means for our purposes. Figure 4.5 displays representative instantaneous fields of gas phase temperature as well as the time-averaged fields. From this, the dependence on mass

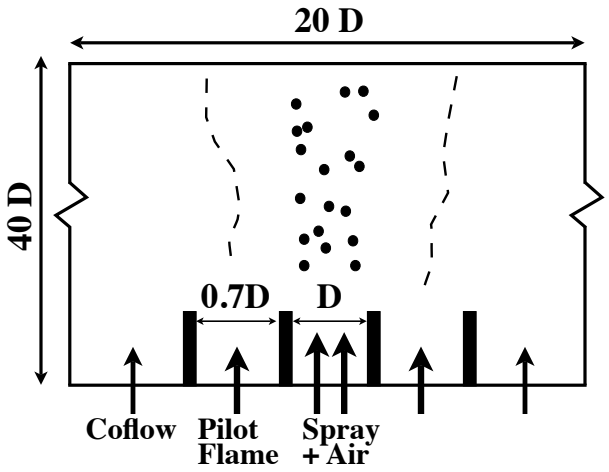

Figure 4.4: Schematic of the spray flame configuration. The spray jet diameter D is 10.5 mm.

loading is clearly displayed.

The determination of a flame length is achieved using the analogy of the stoichiometric value of mixture fraction. The most downstream location of this value in the time-averaged result defined the flame tip. A comparison between the experimentally reported values and those found from the LES/PDF studies in Table 4.2 shows very good agreement for this global quantity under a variety of flow conditions. The largest error from these tests appears for the highest fuel and air loading case. Simplifications to upstream boundary conditions are the probable cause of these discrepancies.

4.3.2 Droplet Evolution

From a validation standpoint, the most comprehensive result reported from the experiments are the mean and rms of the droplet velocities at down-

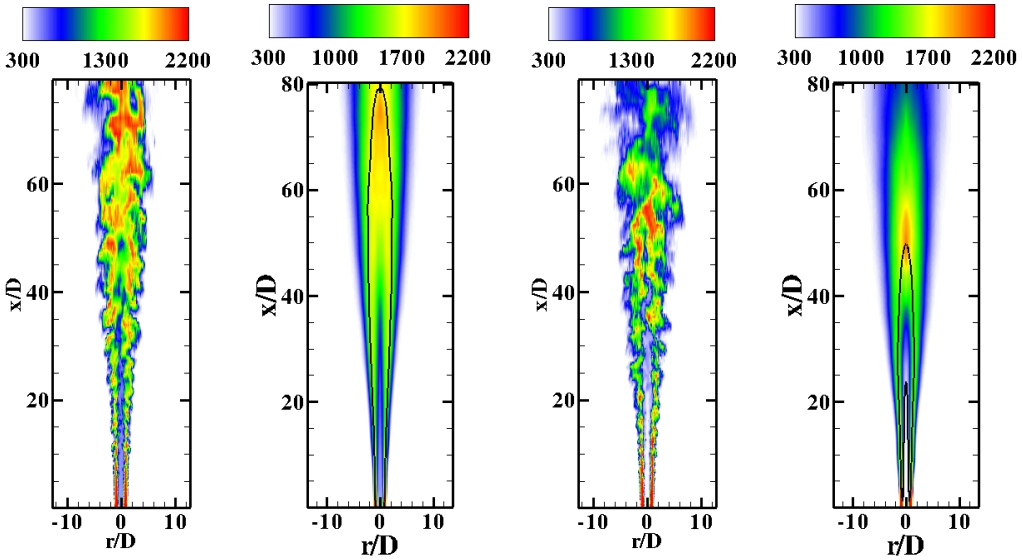

Figure 4.5: Instantaneous and time-averaged contours of gas-phase temperature (shown in Kelvin) for EtF1 (left) and EtF6 (right). The line indicates an isocontour of stoichiometric mixture fraction.

stream stations. Before evaluating the performance of evaporation and combustion models, these values provide insight into the jet spreading and shear layer intensities seen by low-inertia particles. Figures 4.6 and 4.7 display the first two moments of the streamwise and radial velocities from case EtF6. This is representative of the results for the other two validation cases.

First observe the level of accuracy at the $x/D = 0.3$ location, where all four quantities are well-represented. With the simplified boundary conditions at the upstream of end of the auxiliary pipe simulation, this is a surprising result. While the nozzle exit flow is far from fully turbulent, both due to the limited pipe length as well as the damping caused by the presence of droplets, as long as mass flow rate values are accurate, the flow develops in a predictable

Table 4.2: Comparison of experimental and LES/PDF flame lengths.

	EtF1	EtF2	EtF6
Exper.	76 mm	72 mm	53 mm
LES/PDF	79 mm	80 mm	54 mm
Error	3.9 %	11.1 %	1.9 %

manner.

With regards to the spatial evolution of the droplets, there are only two discrepancies worth noting. Deficiencies in streamwise velocity at the intermediate stations may indicate an overall lack of mass flow rate in that direction and an over prediction of jet spreading, but it will be shown that this is directly coupled to an under prediction of gas phase temperature, leading to a higher density, lower velocity core jet. The discrepancy in the predictions of downstream streamwise rms velocity should not be seen as significant due to the accuracy of the other three components at that station.

4.3.3 Flame and Mixing Structure

Figure 4.8 shows the instantaneous plots of velocity and filtered temperature obtained from the LES/PDF computation. As seen in experiments, the flame is long due to the relatively low velocity gradient between the main jet and coflow. The flame front is located outside of the inner jet, leading to reduced levels of turbulent wrinkling. The spray droplets persist up to $x/D = 30$, although the actual mass contained in the liquid phase drops significantly in the near-field ($< x/D = 20$). It is also seen that a high temperature pre-flame

zone on the inner side of the flow close to the main jet. On the other hand, there is much steeper flame front on the co-flow side. Droplet evaporation is primarily caused by the progressive thickening of the pre-flame heating region, where the temperatures are significantly higher than the boiling point of ethanol but considerably lower than the adiabatic flame temperature.

Figure 4.9 shows the filtered mixture fraction and subfilter variance of mixture fraction. The mixture fraction variance has been normalized by $\widetilde{Z}(1-\widetilde{Z})$, which is the maximum local subfilter variance possible for a given filtered mixture fraction. Mixture fraction increases in the core of the central jet, consistent with droplet evaporation occurring away from the reaction zone. It is seen that the mixture fraction variance reaches a maximum of only 15% of the maximum value possible, which shows that the grid is sufficiently resolved to capture the large scale features [29]. Moreover, variance appears in filament-like structures of small length scale compared to the jet diameter. These structures are initially aligned with the flow direction but progressively shift (around $x/D = 13$) to a 45^o angle at downstream distances (see arrows in Fig. 4.9). Since the scalar dissipation rate is linked to variance through a timescale, it exhibits similar structures (not shown here). Note that the alignment of the dissipation structures have been widely studied in the context of gas-phase flames [93, 27, 29]. The nearly 45^o orientation of the structures with respect to the flow direction arises from the direction of the principal compressive strain, which is at 45^o for a pure shear flow [93]. Also, this preferential alignment becomes prominent only downstream while the variance structures

are more aligned with the flow in the upstream region. In this particular flow configuration, droplet evaporation is concentrated in the central jet, so much so that at downstream locations of $x/D = 10$ and beyond, it resembles a conventional non-premixed or partially-premixed flame. This separation of the evaporation zone from the flame leads to a conventional gas-phase flame structure once droplet evaporation is nearly complete.

4.3.4 Conditional Statistics

Figure 4.10 shows the conditional statistics obtained from the PDF computations at three different axial locations. The data are plotted using the particle information at all radial and azimuthal locations. At all axial distances shown, the lean-side of the flame ($Z < Z_{st}$) subscribes to a conventional flamelet-type solution. This part of the conditional plots is obtained from particles that are approaching the flame from the coflow surrounding the pilot. Since the inflow mixture fraction is set at 0.16 to account for the evaporated fuel, the central jet is always richer than stoichimetric conditions. On the rich-side of the flame, a much broader scatter of data is seen, caused by the evaporating droplets. The lower part of this data which shows increasing temperature with increasing mixture fraction corresponds to the droplets evaporating in the pre-flame zone. Since evaporation occurs at significant distance from the flame front, turbulent mixing molecularly mixes the fuel and oxidizer leading to a premixed, variable-equivalence ratio mixture that approaches the flame front. The broad variation in temperature for any given mixture fraction

is similar to a premixed flame with constant equivalence ratio.

At downstream locations, droplet evaporation is nearly complete and the lower line of increasing mixture fraction/temperature is absent. But the scatter for each mixture fraction value persists implying that close to the flame, there exists a persistent region of stratified mixture, which enters the flame zone due to entrainment in the shear layers. The flame itself is located outside the turbulent jet core, and the high central jet velocity prevents the flame from propagating fast enough into this stratified mixture.

4.3.5 Evaporation and Combustion Modeling

In this section, the impact of evaporation and combustion models are evaluated along with an investigation of the performance of the IEM mixing model in the PDF transport equation. Figure 4.11 displays the quantities of interest provided for validation relevant to evaporation and combustion. While gas phase temperature and droplet diameter are self-explanatory, the droplet volume flux is used as a measure of evaporation rate between downstream stations. Individual profiles are useful in comparison to experimental results, though it is the change from one location to the next that defines some measure of global evaporation rate. It is useful to note that mean droplet diameter and droplet volume flux profiles should be correlated to the gas phase temperature of the upstream adjacent measurement station. The high rate of droplet advection decorrelates the evaporation and combustion characteristics at a given location.

The combustion model predictions perform relatively well in the shear layer where the pilot serves to maintain high reaction rates. However, the model tends to under predict temperatures near the centerline in the near field before recovering by the furthest station. While this appears to be an important discrepancy, it will be shown in the following section that these results serve to justify the transported PDF equations predictions of extreme temperatures in comparison to more conventional filtered scalar transport predictions.

One of the unique characteristics of these flames is the apparent increase in mean droplet diameter as the flow progresses downstream. This would seem counterintuitive due to strong evaporation that should drive down mean diameter. This is not the case, however, mainly due to the contribution of non-equilibrium evaporation effects, as modeled in Eq. 2.24. It has been shown [60] that small droplets can experience a drastically accelerated evaporation rate when exposed to intermediate temperatures, as is the case along the centerline of the jet. In the case of the transported PDF predictions, there is some ability to capture this non-equilibrium effect, though the underprediction of gas phase temperatures in the near field results in an underprediction of overall non-equilibrium contribution further downstream.

As previously noted, the conditional diffusion (micro-mixing) model tends to be a source of uncertainty for transported PDF methods and can be strongly dependent on model parameters. In this case, a range of $\mathcal{C}_\phi$ values have been analyzed for the IEM model (Eq. 2.35) to investigate the sensitivity

of gas phase temperature predictions to the choice of value. For this case, the pilot serves to both stabilize the flame and prevent rapid jet spreading and mixing due to a high density ratio (> 10) between high density core and low density vitiated pilot mixture. Because of this, the rate of mixing has no significant effect, even across an order of magnitude range of model coefficients. As will be seen for the auto-igniting validation case, this is not a universal characteristic for spray flames.

4.3.6 Comparison between PDF and Filtered Scalar Transport

In this section, a comparison is made between the combustion predictions of the proposed transported PDF approach with a more conventional filtered scalar transport (Eq. 2.4). Both approaches utilize a flamelet-progress variable approach for the determination of the chemical source terms, though the transported PDF does not rely on the β-function assumption regarding the structure of sub filter mixing. The transported PDF results reported below match those from the previous section with an IEM model coefficient value of $\mathcal{C}_\phi = 0.5$.

Differences in the time-averaged values are prefaced by showing instantaneous fields of gas phase temperature in Fig. 4.12. There is a clear difference in the overall levels of reaction in the shear layer and near the flame tip. In addition, the filtered scalar transport equation tends to predict a very continuous flame in the shear layer, while the LES-PDF approach tends to capture a large amount of local extinction.

Figures 4.13 and 4.14 display the evaporation and combustion model predictions for both case EtF6 and EtF2, respectively. The air mass flowrate is matched between these two cases with an increased fuel mass loading for the EtF2 flame. Comparing only the experimental data for these two cases reveals that the fuel mass loading serves to suppress high levels of centerline reaction due to an overall rich mixture at those locations.

Comparing the two modeling approaches reveals a trade-off in this particular configuration that serves to inform usage in more practical combustion applications. While both approaches capture the combustion and non-equilibrium evaporation well for case EtF2, the most significant difference arises in the ignition location and intensity predicted for the lean mixture in EtF6. The filtered scalar transport approach captures the near field ignition levels well, far superior to the proposed method. The disadvantage, however, arises downstream, where the transported PDF approach reports much more reasonable centerline temperature values.

This trade-off can be seen in two ways: 1) that the transported PDF induces a delayed ignition time due to numerical diffusion, or 2) the filtered scalar transport over-predicts global reaction rates in high temperature regions. The distinction becomes important depending on the quantity of interest. For most combustion applications, value is placed on an accurate characterization of extreme conditions, i.e., high temperature, high pressure conditions. This provides justification for the transported PDF approach, even in this simple jet flame configuration. The filtered scalar transport equation also performs

well here due to the distinct evaporation and combustion zones. It has been shown [18] that the need for a dynamic, adaptive combustion model becomes much more important in industry-relevant configurations where droplets routinely penetrate reaction zones due to recirculation or swirl effects.

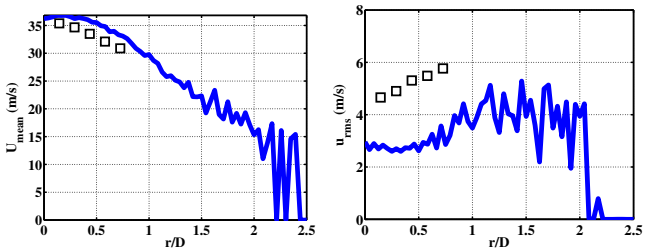

(a) x/D = 30

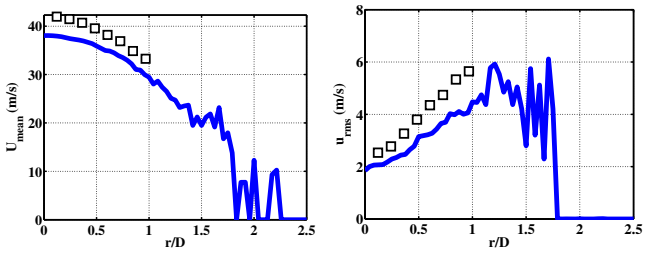

(b) x/D = 20

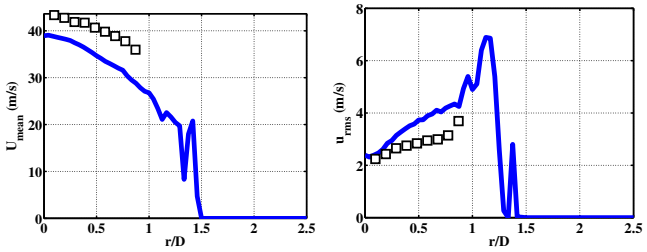

(c) x/D = 10

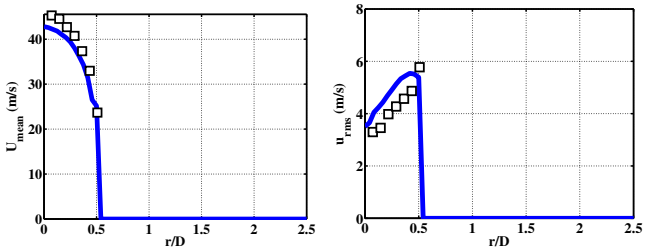

(d) x/D = 0.3

Figure 4.6: Comparison of droplet velocity statistics between LES/PDF simulations (lines) and experimental measurements (symbols). The quantities shows are streamwise mean (left) and streamwise rms (right).

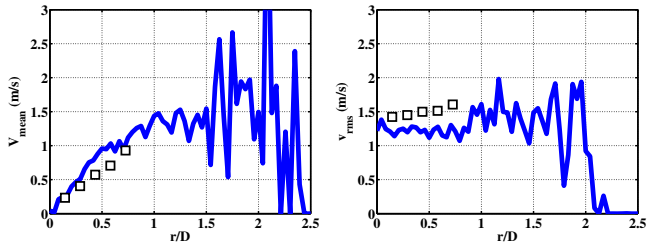

(a) x/D = 30

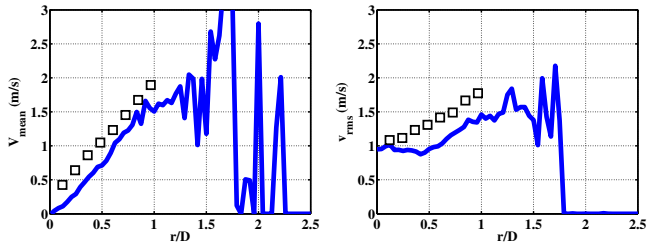

(b) x/D = 20

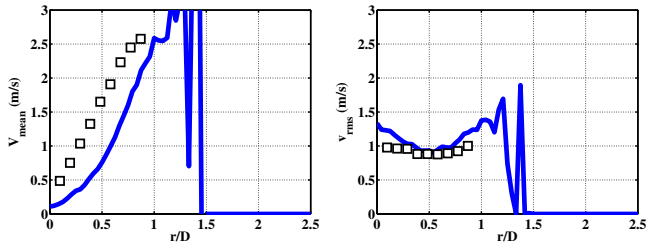

(c) x/D = 10

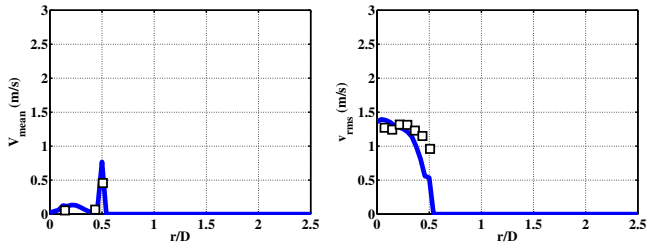

(d) x/D = 0.3

Figure 4.7: Comparison of droplet velocity statistics between LES/PDF simulations (lines) and experimental measurements (symbols). The quantities shows are radial mean (left) and radial rms (right).

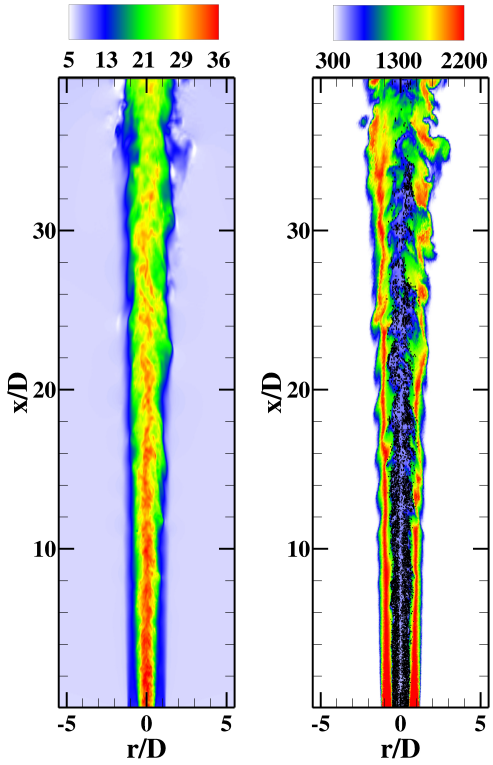

Figure 4.8: Instantaneous contours of streamwise velocity (shown in m/s) (left) and gas phase temperature (shown in Kelvin) overlaid with number density lines (right).

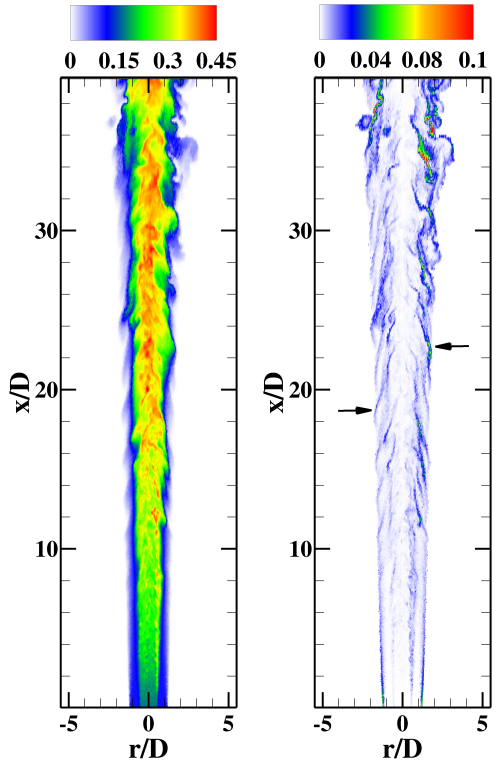

Figure 4.9: Instantaneous contours of filtered mixture fraction (left) and normalized subfilter mixture fraction variance (right).

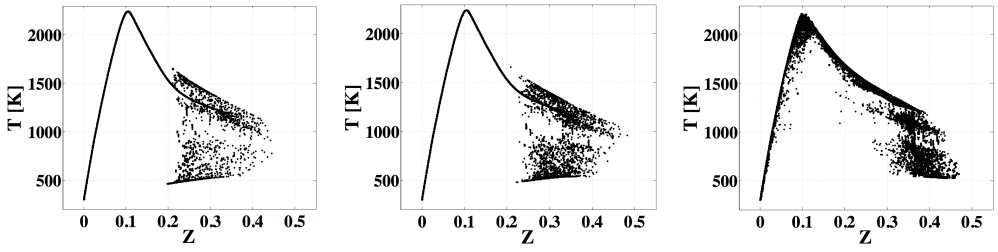

Figure 4.10: Instantaneous PDF notional particle temperature conditioned on particle mixture fraction for all particles located at $x/D = 5$ (left), $x/D = 10$ (middle), and $x/D = 30$ (right).

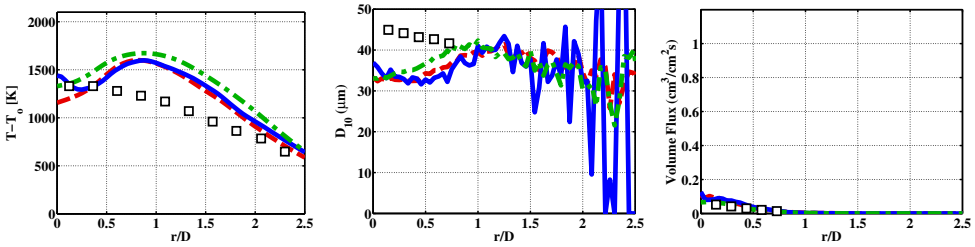

(a) x/D = 30

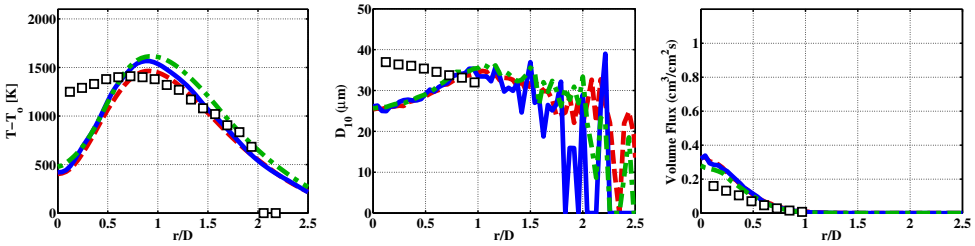

(b) x/D = 20

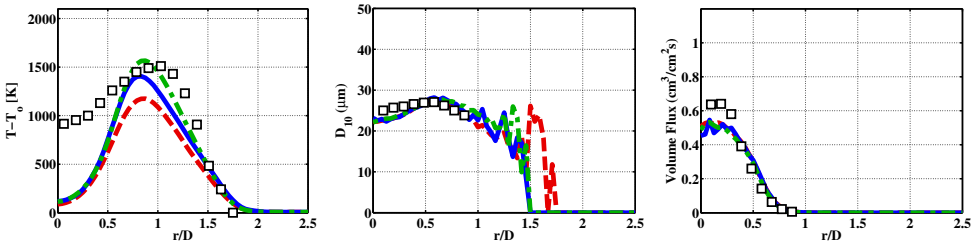

(c) x/D = 10

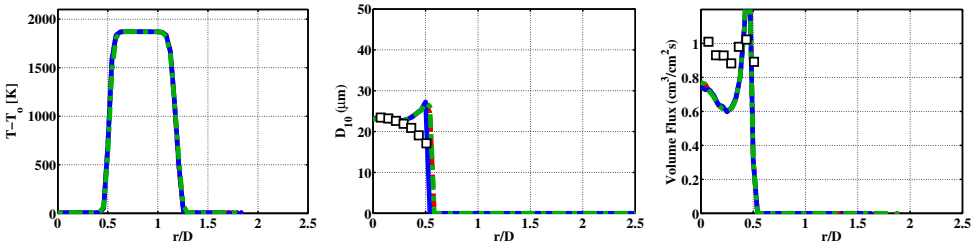

(d) x/D = 0.3

Figure 4.11: Comparison of gas-phase temperature (left), mean droplet diameter (center) and droplet volume flux (right) statistics between LES/PDF simulations (lines) and experimental measurements (symbols) for case EtF6. The IEM model coefficient (Eq. 2.35) is prescribed as $\mathcal{C}_\phi = 0.1$ (red dashed), 0.5 (blue solid) and 2.0 (green dash-dotted).

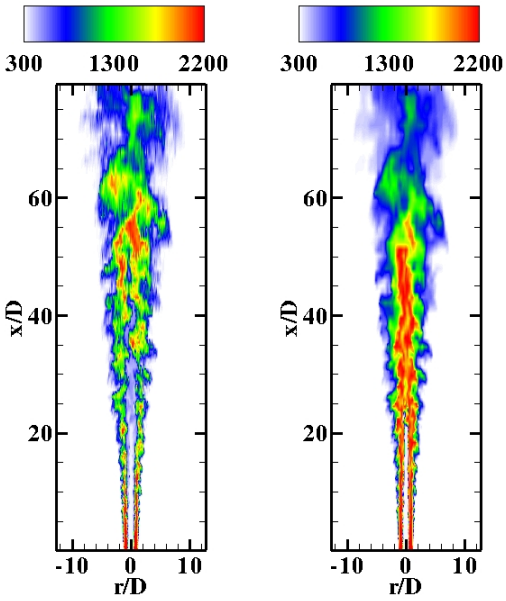

Figure 4.12: Instantaneous contours of gas phase temperature (shown in Kelvin) for EtF6 results from the LES/PDF simulations (left) and LES with filtered scalar transport (right).

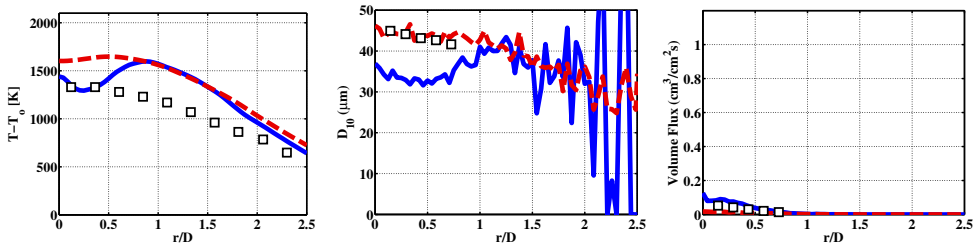

(a) x/D = 30

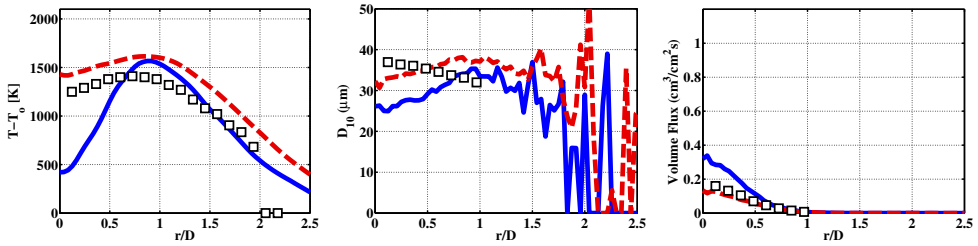

(b) x/D = 20

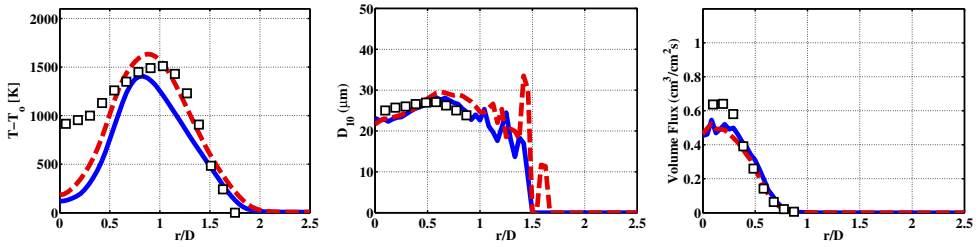

(c) x/D = 10

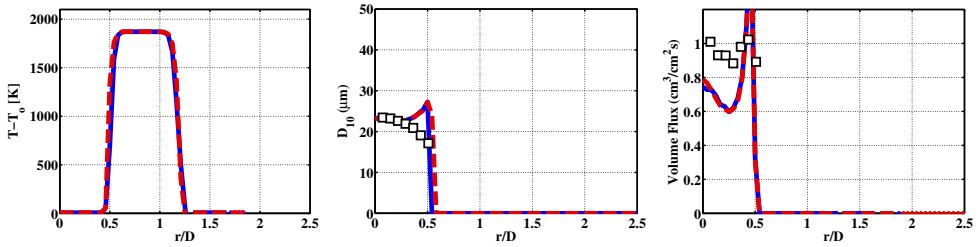

(d) x/D = 0.3

Figure 4.13: Comparison of gas-phase temperature (left), mean droplet diameter (center) and droplet volume flux (right) statistics between LES/PDF results (blue solid line), full LES results (red dashed line) and experimental measurements (symbols) for case EtF6.

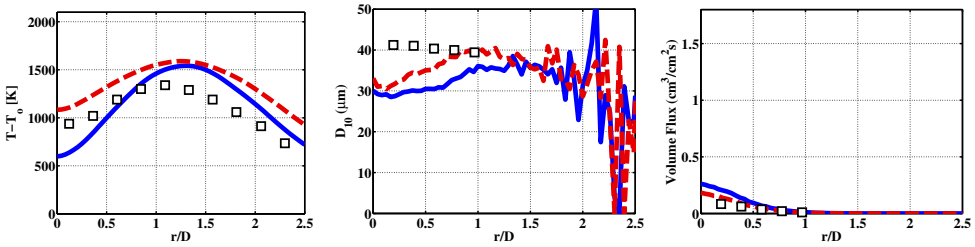

(a) x/D = 30

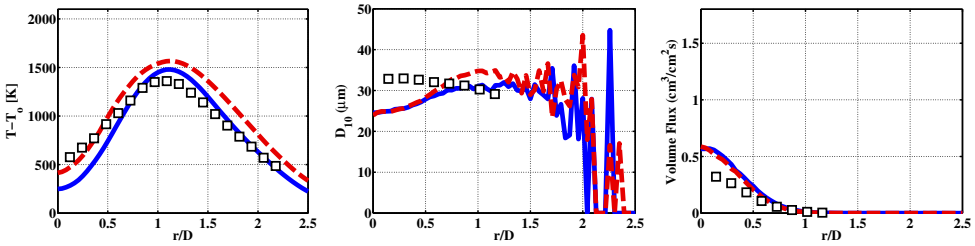

(b) x/D = 20

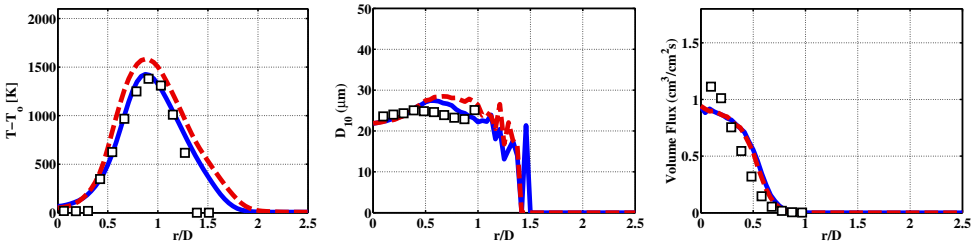

(c) x/D = 10

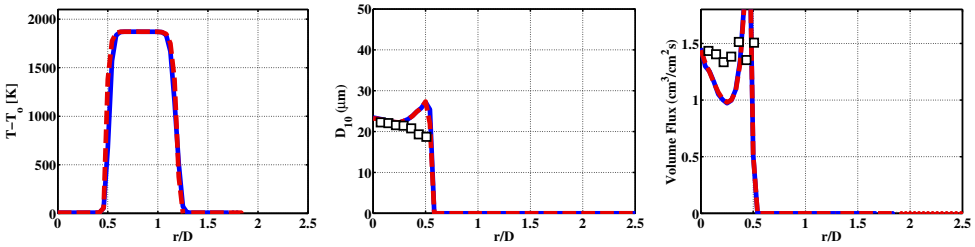

(d) x/D = 0.3

Figure 4.14: Comparison of gas-phase temperature (left), mean droplet diameter (center) and droplet volume flux (right) statistics between LES/PDF results (blue solid line), full LES results (red dashed line) and experimental measurements (symbols) for case EtF2 at downstream locations of $x/D = 0.3,\ 10,\ 20$ and 30.

Chapter 5

LES/PDF Simulation of a Lifted Methanol Spray Flame

The goal of this work is to develop a novel Lagrangian transported PDF approach with spray/combustion interactions to model auto-igniting methanol spray flames. The subfilter PDF will be described using a large number of notional stochastically evolving particles. A new probabilistic spray/combustion coupling algorithm is developed that will allow the subfilter interaction of spray droplets with the gas phase thermochemical combustion process. Detailed chemical kinetics are incorporated, with cost-reducing algorithms using the *in-situ* adaptive tabulation (ISAT) [82, 94] approach. These high fidelity approaches help probe minor species evolution in these flames. This LES/PDF approach is used to study ignition events in three different spray flames experimentally studied at the University of Sydney [95, 96]. In particular, the impact of small-scale mixing on ignition is studied.

5.1 Additional Modeling Considerations

5.1.1 Scalar Mixing Time Scale

The mixing time scale should provide a measure of the filter-level mixing time for the thermochemical composition vector. In LES, this timescale

is often specified based on turbulent diffusivity [14, 97, 98]. However, for the commonly-used dynamic model considered in this work [53], the diffusivity parameter has very high wavenumber content and is not a smooth field. Consequently, it is not a good descriptor of the mixing time. Given that turbulent diffusivity is evaluated based on the filtered strain rate [99], it is better to use this quantity for defining the time scale, resulting in the following implementation for the IEM model

$$\widetilde{\mathcal{M}_\alpha|\boldsymbol{\psi}}, \eta = \mathcal{C}_\phi|\overline{S}|\left(\boldsymbol{\psi}_\alpha - \widetilde{\phi}_\alpha\right) \tag{5.1}$$

In this case, the coefficient $\mathcal{C}_\phi$ cannot assume the same values as the turbulent diffusivity based models (set to anywhere between 2.0-8.0). In this work, a nominal value of $\mathcal{C}_\phi = 0.1$ is chosen based on comparisons with gas phase flames. However, this coefficient is varied to understand the role of the subfilter PDF on the evolution of the ignition process. It should be noted that the higher the coefficient value, the faster the subfilter mixing is, leading to a change in the ignition kernel development.

5.1.2 Stochastic Spray Algorithm for Droplet Evaporation

In almost all spray applications, the conditional source term ($\dot{W}_c, \dot{S}_c^e$ in Eq. 2.32) is equated to the unconditional source, implying that there is no direct dependence of the evaporation source term on the gas phase composition. In the context of mixture-fraction based spray modeling, Pera et al. [100] have proposed a correlation based on direct numerical simulations. In the FSSF approach, later adapted to LES by De and Kim [101], the subfilter PDF

is sampled in order to obtain surface conditions for a droplet. In this work, we follow a similar approach but leverage the availability of the multi-dimensional PDF for obtaining the droplet evaporation conditions.

Two fundamental assumptions are required to determine the local composition at a droplet's surface from the notional PDF particles. First, droplets are assumed to be uniformly distributed at the subfilter level. This is valid for droplets with Stokes numbers differing from unity where clustering is avoided. In the LES context, there is no means to define subfilter correlations between droplet location and gas phase composition, thus requiring this assumption. Second, the filter volume is defined as an ensemble of fluid elements with uniform composition that decrease in size as Reynolds number increases. Therefore, given a droplet location, the fluid element at that location can be directly provided by the scalar PDF defined in Eq. 2.30. In other words, the probability of finding a fluid element of a given composition $\{\boldsymbol{\psi}, \eta\}$ is provided by $P(\boldsymbol{\psi}, \eta)$. In a time-varying flow, the effective evaporation rate is then obtained by carrying out the evaporation process with repeated sampling of the subfilter PDF. In statistically stationary flows, such as the configuration simulated here, temporal averaging could be used instead. In this case, at each time-step, the droplet is paired with a gas phase Lagrangian particle, sampled based on the PDF.

The pairing of a droplet and PDF particle is initiated independently for each droplet entering a filter volume and is retained for the entire duration that both particles remain in the computational cell, requiring reinitialization

if the PDF particle exits prior to the droplet. For each droplet, a PDF particle is randomly chosen but from the distribution weighted by the particle weights. In this sense, more than one droplet could be paired to the same PDF particle. This implementation provides a pairing time that is on average the time taken to traverse half the filter width. This pairing time respects the definition of the LES filter volume as the smallest resolved length scale. The process is displayed in Fig. 5.1, where in the conventional method, all PDF particles within a given filter volume receive proportional contribution from droplet evaporation, while in the proposed approach, only one particle per fuel droplet is involved in both the evaluation of evaporation rate as well as consistent adjustment of particle weight and scalar from the resulting evaporation source terms.

It is possible to include more sophisticated description of the spatial structure of the scalars at the small-scales but this will invariably require additional modeling and model inputs. Additionally, the cell residence pairing time minimizes artificial mixing of the fuel with the other fluid elements in the cell. Note that in the absence of this coupling, the evaporated fuel is added to the entire filter volume ensemble of PDF particles, weighted by their composition [102]. Distribution of this mass leads to artificial mixing, which progressively removes all variations in subfilter composition as the time-step is decreased. In this work, the exclusive pairing ensures that the coupling of evaporation and mixing rates are independent of time-step. The effect of this stochastic coupling will be discussed in Sec. 5.3.3.

5.1.3 *In Situ* Adaptive Tabulation for Detailed Chemistry

Coupling detailed chemistry with the Monte-Carlo method for PDF transport involves impractical computation expense. A previously developed *in situ* tabulation method proves to be very effective in reducing computational expense while maximizing accuracy with direct integration of a chemical mechanism. This approach, previously mentioned as ISAT, aims to return the resulting composition following integration for a time step Δt within a prescribed error tolerance ϵ_{tol}. During each request to the ISAT software to determine the result of an integration, the algorithms go through the following process:

1. The initial composition, energy and integration time step are received from the calling function.

2. These input values are queried against previous calculations performed by ISAT via the search of a binary tree.

3. If the Euclidean norm between the input values and the values of a previous calculation is less than the prescribed error, ϵ_{tol}, the composition and state variables are read from the tree and a direct integration is not performed.

4. Otherwise, if after searching the previously performed calculation no sufficiently representative values are found, a direct integration is performed and a new entry is stored in the tree for future searches.

The ISAT subroutines used for this work have been made available for open source usage [94].

5.2 Spray Flame Configuration and Simulation Details

The experimental configuration of O'Loughlin and Masri [96] is simulated here. A schematic of the flow configuration is provided in Fig. 5.2. The experimental setup consists of a central jet of 4.6 mm diameter issuing a mixture of air and pre-atomized fuel droplets as well as fuel vapor from evaporation as the mixture travels to the jet exit plane. The bulk velocity of the air is set to 75 m/s. The coflow is burnt hydrogen-air with excess oxygen at a temperature of 1430 K and a streamwise bulk velocity of 3.5 m/s. The Reynolds number based on jet diameter and carrier air flow rate is 23,750. Three different flames were chosen for this study and relevant experimental parameters can be found in Table 5.1. These cases are parameterized by increasing spray mass flowrate, resulting in lowered centerline temperatures at the jet exit plane due to pre-vaporization and a progressive decrease in flame lift-off height [96].

Table 5.1: Jet flame boundary conditions.

Case	$\dot{m}_{fuel}$ (g/min)	Y_{fuel}	T_{CL} (K)
Mt2A	20.4	0.018	283
Mt2B	23.8	0.047	287
Mt2C	27.1	0.080	288

The simulations were conducted based on a low-Mach number finite

volume solver [70, 71]. The equations of motion were solved in a cylindrical coordinate system with 160 $\times$ 108 $\times$ 32 grid points in the axial, radial, and azimuthal directions, respectively. Grid clustering was used to resolve the central jet and the shear layers. The jet boundary condition was specified as a combination of gas phase velocities taken from a transient turbulent pipe flow at the experimental flow rate and droplet velocities interpolated to match those values. Droplets were uniformly distributed across the jet profile and their diameters were randomly selected from a log-normal distribution set to match the d_{10} and d_{32} moments of the distribution given by the experiments. No artificial grouping of droplets is considered as each injected computational particle is representative of an individual droplet. The vapor fuel mass fraction in the jet is assumed to be uniform as is the equilibrium composition of the coflow.

For the Monte Carlo approach to transport of the subfilter PDF, an average of 20 particles per cell were present, regulated by the splitting of high-weight particles and merging of low-weight ones to maintain an appropriately sized ensemble in each cell. Analysis of the IEM mixing model was conducted with values varying from 0.025 to 1.0 with respect to the strainrate-based timescale. The chemical source term calculation uses a 18-species, 19-step reduced mechanism for methanol oxidation [103] coupled to the ISAT algorithm. In order to reduce the computational expense of ISAT integrations in each timestep, processors which required the most wall-clock time during the previous time step have their respective integrations and tabulations re-

distributed uniformly in parallel by temporarily transferring tagged particles between processors. With direct integration requiring much more computational time than communication or redistribution, this provides a 5-10 times speedup of ISAT. Speedup values in excess of 100 are achieved in comparison to direct integration for the configurations and PDF particle number density considered in this work. For each case, statistics were collected over eight jet flow-through times to ensure convergence, utilizing 192 processors and 12,000 computational hours per simulation.

5.3 Results and Discussion

5.3.1 Flame Ignition Processes

The instantaneous data are presented to identify the key physical processes in this flame. Figure 5.3 shows temperature contours in the three different flames overlaid with isolines of peak heat release. As expected, the ignition region moves upstream with increased fuel flow rate. The increase in fuel flow rate is accompanied by an increase in pre-vaporized methanol mass fraction entering the domain with the carrier gas as well. For all three flames, it is seen that pockets of high-temperature gases enter the central jet either through entrainment or auto-ignition of premixed fuel/air mixture that has had sufficient residence time. The ignition kernels appear sporadically, and only a fraction of the kernels actually transition to a fully burning pocket. The probability of such transition increases from flame A to C. As seen in this picture, the length that such ignition kernels have to travel before attaching to the main flame is

considerably shortened in the most reactive case, flame C, as compared to the other flames. In flame A, the ignition kernels could be dissipated by mixing with the cold central jet (even though there is considerable fuel in this flow stream).

The ignition process is observed to occur in two different modes. In the first mode, a coflow pocket of relatively high temperature (>1000 K) enters the central jet through entrainment. Here, the pocket then accelerates the evaporation of droplet groups over short times that lead to a local ignition kernel. The subsequent propagation of these kernels depends on the rate of mixing with the gas phase. The second mode is caused by a process similar to stratified ignition. The continuous mixing with the coflow causes the central jet to progressively increase in temperature over time as evaporation continuously contributes vaporized fuel. At the same time, the evaporation of the droplets increases the methanol concentration in the jet. Figure 5.4 shows the time-averaged centerline mass fraction of methanol. It is seen that the drop in methanol concentration is considerably lower than would be expected of a passive scalar issuing into a coflow. This is essentially due to the evaporative addition of fuel vapor to the central jet. At around x/D=25-30, the core of the central jet breaks down, which ignites the premixed mixture. Immediately following this, the increased gas phase temperature causes the droplets to evaporate rapidly, leading to a substantial increase in methanol vapor at intermediate locations. The base of the flame is located downstream of this maximum evaporation region, which consumes all of the fuel. The centerline

profiles show that the flame base is located far upstream in the most reactive case, while the least reactive case shows a more progressive consumption that leads to weak flames before a fully ignited flame is set up at x/D > 35. Each of these two ignition modes are central to the stochastic coupling algorithm (described in Sec. 5.1.2) and analyzed in Sec. 5.3.3.

5.3.2 Comparison with Experimental Data

The time-averaged data are compared with experiments to establish the overall accuracy of the approach. Droplet velocities for cases Mt2A and Mt2C shown in Figure 5.5 show reasonable agreement with experimental measurements. Discrepancies in droplet velocity are induced by differences in local density due to the simulation flame structure discussed below. Figure 5.6 shows the comparison with experimental temperature measurements for the least and most reactive cases. In these plots, the first location shows shear temperature rise due to preliminary mixing but no evidence of ignition for any of the three cases. At x/D=20, the experiments show ignition in the core of the central jet, while the simulations show some increase but do not match the level of ignition observed in the experiments. At other downstream locations, the flame is fully ignited leading to higher average temperatures. It is important to note that the average temperatures are nearly 500 K lower than the instantaneous peak temperature, indicating that there is considerable variation in the axial location of the flame. From the instantaneous plot, it can be seen that the high temperature region is long but sufficiently turbulent

that large radial displacements occur throughout the simulation. This leads to an average that is principally uniform across the radius of the jet. The simulations do predict a flame based in the center of the jet throughout the downstream locations, in contradiction to the experiments, at least for the most reactive flame C, which show a shear layer based flame with two peaks on either side of the centerline. The grid used here is relatively coarse (as LES calculations should be!), and the shear layers are not fully captured. With this discrepancy in mind, grid dependence and ISAT error tolerance have both been tested without significant response in flame ignition. Possible sources of error include the chemistry mechanism, and the use of the turbulent diffusivity model based on local equilibrium formulation that may not be valid in a spray flow configuration.

5.3.3 Subfilter Interactions Between Spray Droplets and Gas Phase

The stochastic coupling algorithm (Sec. 5.1.2) is designed to prevent artificial mixing that is characteristic of unconditional rate based models [102, 104]. In the method proposed here, a spray droplet and a PDF particle are paired, with the probability of choosing a particular PDF particle based on its weight. Figure 5.7 shows scatter plot of particle fuel composition plotted against temperature for a few filter volumes. Note that these samples were obtained at random from fuel-rich regions, and constitute instantaneous subfilter distributions. Consequently, they are not statistical quantities, but instead serve to illustrate the effect of the coupling algorithm. In the case of the un-

conditional source term for evaporation, the evaporated mass is distributed to all the particles. This creates an artificial mixing process, which is both temporally non-convergent and represents an unphysical process. Consequently, it can be seen that this unconditional approach leads to particle values that remain near the ensemble average. In fact, as the time-step is decreased, it can be shown that variance will be even lower since this volumetric distribution will cause all particles to progressively become fuel-rich.

On the other hand, the stochastic spray/combustion coupling introduces a pairwise interaction that leads to a very different behavior. Fig. 5.7 shows that the stochastic coupling causes significant variations in fuel mass fraction. Variations are magnified as droplets and particles remain coupled for an entire cell residence time. Note that the scenario minimizing artificial mixing would independently introduces an additional PDF particle to the gas phase for the evaporated mass from each droplet and subsequently mix at the filter-level time-scale. However, this implementation would not be realistic since the fuel source is at length-scales smaller than the Kolmogorov scale (or the equivalent diffusive scale). Hence, it should be expected that mixing will be faster than the filter-level time-scale. Therefore, while the use of pairwise coupling implies infinitely fast mixing between the spray/PDF particle pair, it limits mixing to filter-level time-scale for mixing with other particles in the cell.

With regards to the impact on ignition, this coupling will allow both the entrainment and the premixed modes to be captured. In the entrainment

mode, the spray droplet is surrounded by a local coflow pocket, which is similar to the pairwise interaction introduced here. Since this pocket travels at the local convective velocity, it is reasonable to pair the spray/PDF particle for the entire duration that the particles are in the cell. On the other hand, the slow mixing of evaporated fuel in the central jet will lead to near uniform subfilter mixing close to the region where jet breakdown occurs, thereby capturing the premixed ignition process. Figure 5.8 shows mean temperature profiles for flame C near the ignition region. The unconditional source term produces a much lower temperature as compared to the stochastic coupled result, since the former approach preferentially creates the premixed mode of ignition. Since the equivalence ratio of the mixture is leaner than stoichiometric in this zone, the temperature increase in lower. The stochastic coupling produces a mixture of entrainment-based and premixed ignition processes (with the former alone, temperatures will be even higher) leading to higher temperatures.

5.3.4 Effect of Mixing Rates on Flame Ignition

The mixing time scale used in the conditional diffusion model (Sec. 2.4.1) has a significant effect on determining the burning mode in these flames. Figure 5.9 displays both the subfilter variance of gas phase temperature as well as the resolved RMS values at the location of peak heat release in the most reactive flame (Mt2C). It is interesting to note that as the subfilter mixing is increased at the flame front, the RMS temperature fluctuations also increase. This is counter-intuitive, since increased small-scale mixing should homogenize

the fluid, which propagates to yield a premixed-like flow system. It appears that increased mixing in this system serves to suppress combustion by decreasing the probability of an ignition kernel surviving turbulent mixing. This is observed in the simulations of Prasad and Masri [104], where the use of a single stochastic field model (which is essentially assuming infinitely fast mixing rate) produces a lower average temperature compared to a case with eight fields. In the conserved scalar modeling context, increasing $\mathcal{C}_\phi$ is equivalent to increasing scalar dissipation rate.

The increased mixing rate seeks to produce pockets of suppressed burning which convect along the centerline. Consequently, the effect of increased mixing is seen only near the centerline. While the subfilter variance of temperature increases with decreasing $\mathcal{C}_\phi$, the mean temperature does not change away from the centerline. This could be the result of a few burning particles dominating the mean composition through large weights. This is particularly possible if these particles were entrained from the coflow, where the local volume is higher and the particles have larger weights. The variance is generated essentially by the presence of smaller but non-burning or partially burning PDF particles.

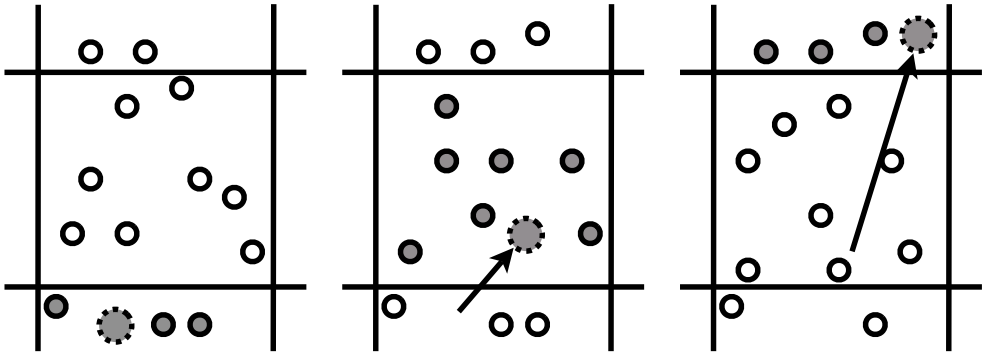

(a) Conventional unconditional evaporation

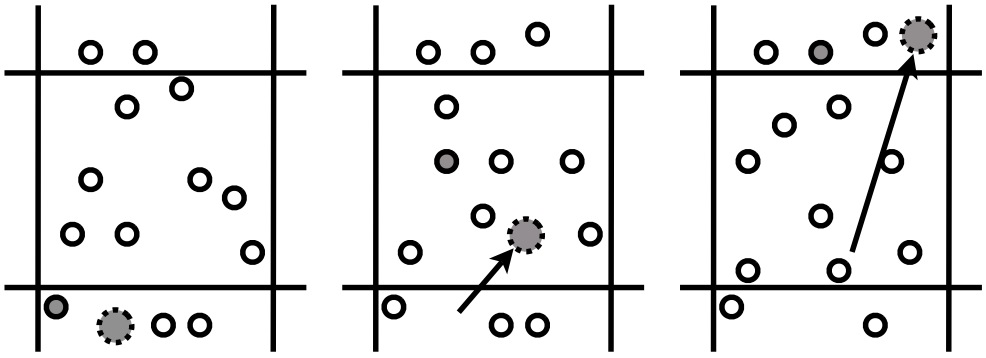

(b) Proposed conditional evaporation

Figure 5.1: Coupling algorithms for Monte Carlo transported PDF approaches in evaporating spray-laden flows. Lagrangian fuel droplets (dotted line) and Monte Carlo PDF particles (solid line) are shown. Active particles in the coupling algorithm are shaded.

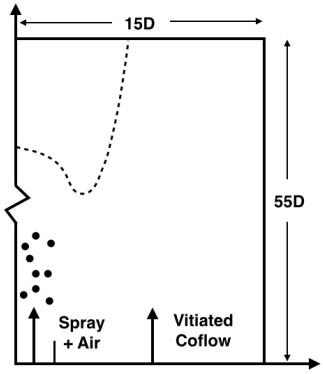

Figure 5.2: Schematic of the axisymmetric configuration with dashed line indicating approximate lifted ignition region.

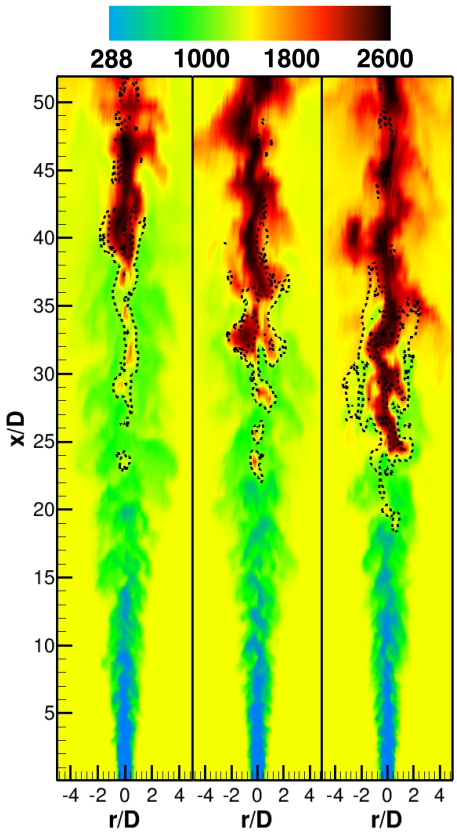

Figure 5.3: Representative instantaneous gas phase temperature fields (shown in Kelvin) from LES-PDF simulations of flames Mt2A (left), Mt2B (middle), Mt2C (right). Dashed lines represent regions of significant heat release as described by [OH][CH_2O].

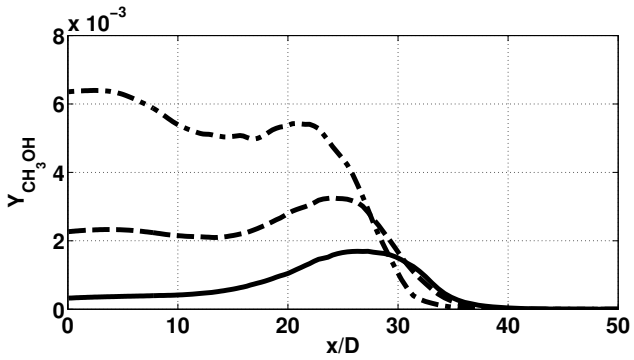

Figure 5.4: Time-averaged methanol vapor mass fraction profiles along the centerline for Mt2A (solid), Mt2B (dash) and Mt2C (dash-dot).

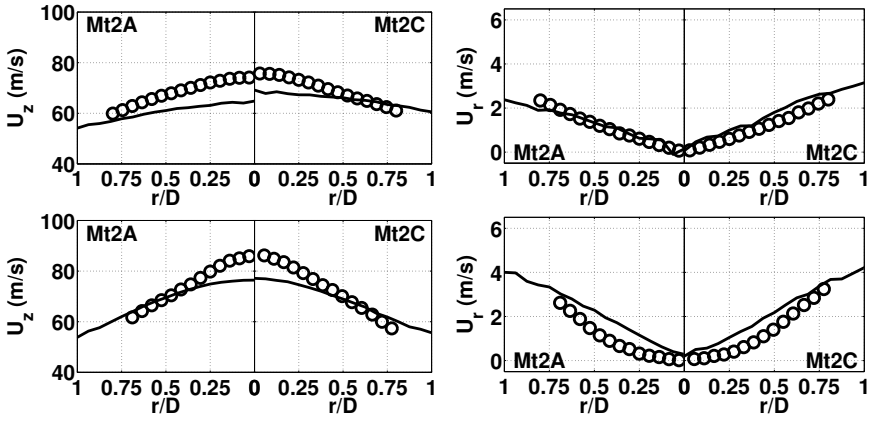

Figure 5.5: Mean streamwise (left) and radial (right) droplet velocity profiles for case Mt2A and Mt2C at x/D of 10 (bottom) and 20 (top) from LES results (lines) and experimental measurements (symbols).

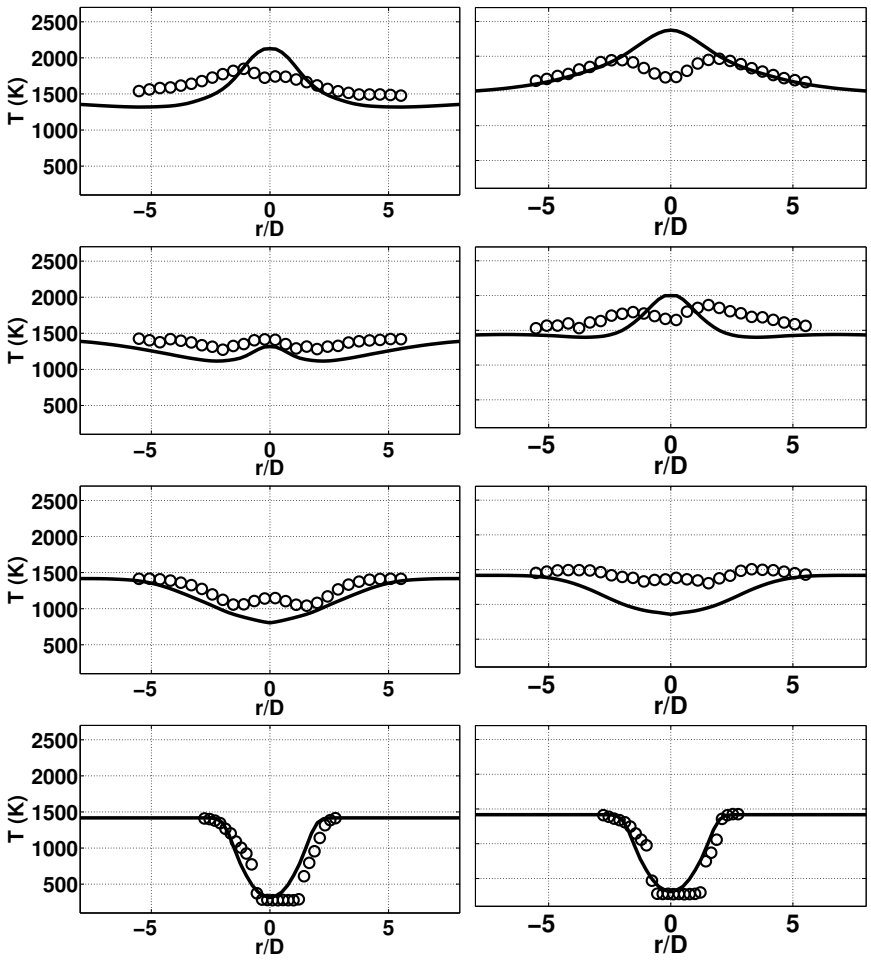

Figure 5.6: Mean temperature profiles for case Mt2A (left) and Mt2C (right) at x/D locations of 5, 20, 30 and 40 (bottom to top) from LES results (line) and experimental measurements (symbols).

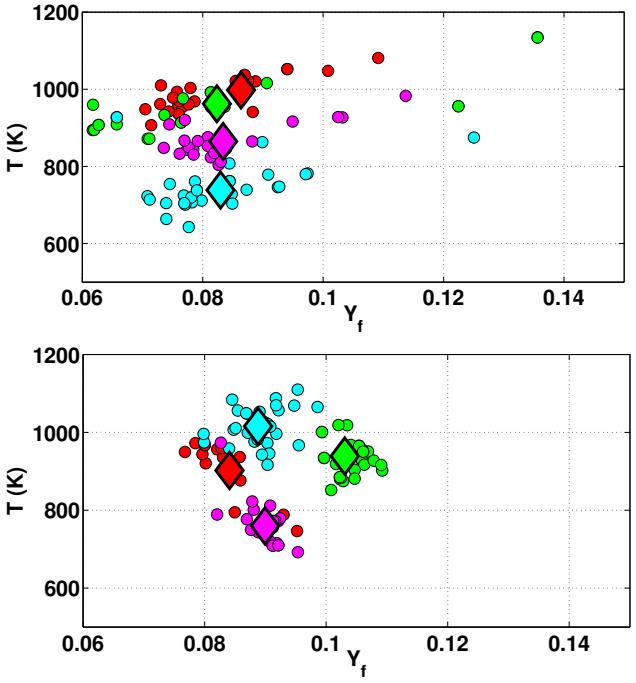

Figure 5.7: Scatter of gas phase temperature and methanol mass fraction (Y_f) for PDF particles located in four representative cell volumes and the ensemble average (diamond). Cases with evaporation using conditional stochastic (top) and unconditional volume average source term (bottom) are shown. Colors denote respective cell.

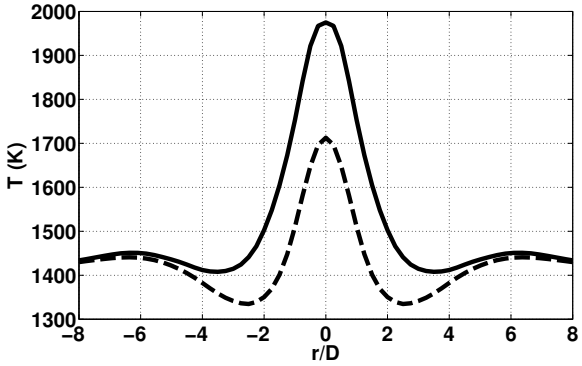

Figure 5.8: Mean temperature profile at x/D = 30 using conditional (solid) and unconditional (dash) evaporation modeling.

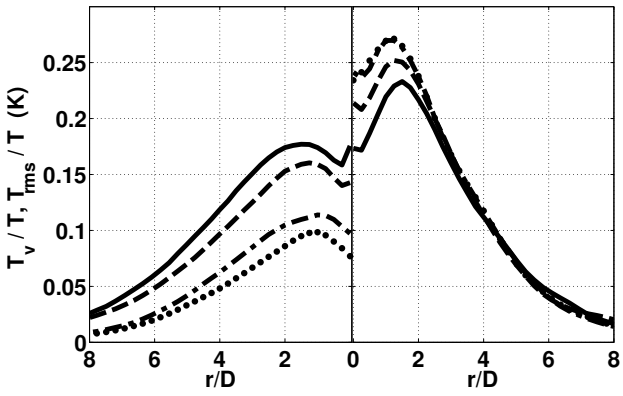

Figure 5.9: Time-averaged subfilter variance (left) and rms (right) of gas-phase temperature for IEM $\mathcal{C}_\phi$ values of 0.025 (solid), 0.1 (dash), 0.5 (dash-dot) and 1.0 (dot).

Chapter 6

Explicitly Filtered LES Approach

Explicit filtering originated with the idea of developing commutative filters for LES [37]. On non-uniform grids, the filtering operation does not commute with the spatial derivative, leading to errors [105]. The commutative filters developed by Vasilyev and co-workers [37] emulate sharp spectral cutoff filters. Their formulation introduces an explicit filtering operation that limits the wavenumber content through specification of a filter width relative to the computational mesh size. Consequently, even on uniform meshes, the explicit filtering operation could be used to separate the filter width parameter from the underlying computational grid.

6.1 Momentum and Scalar Transport Equations

Similar to all LES formulations, the filtering operation is defined as follows

$$\overline{\phi}(\mathbf{x},t) = \int_{\alpha}^{\beta} \phi(\mathbf{y},t)\mathcal{G}(\mathbf{y}-\mathbf{x},\Delta)d\mathbf{y}, \tag{6.1}$$

where $\overline{\phi}$ is the filtered field corresponding to original field ϕ, and $\mathcal{G}$ is the filtering kernel. The kernel is specified in a manner that minimizes commutation error and also removes energy from the small scales. The extent of the

integral is physical space is determined by α and β. The equivalent expression for Favre-filtered equations is given by

$$\widetilde{\phi}(\mathbf{x},t) = \frac{1}{\overline{\rho}(\mathbf{x},t)} \int_{\alpha}^{\beta} \rho(\mathbf{y},t)\phi(\mathbf{y},t)\mathcal{G}(\mathbf{y}-\mathbf{x},\Delta)d\mathbf{y}, \tag{6.2}$$

where ρ is the density.

The explicitly filtered equations are derived by convolving the governing equations with the commutative filter kernel defined above [37]. The filtered continuity equation takes the form

$$\frac{\partial \overline{\rho}}{\partial t} + \frac{\partial \overline{\rho}\widetilde{u}_i}{\partial x_i} = 0, \tag{6.3}$$

where $\widetilde{u}_i$ is the Favre filtered velocity field. Following the same procedure gives the filtered momentum equation as

$$\frac{\partial \overline{\rho}\widetilde{u}_i}{\partial t} + \frac{\partial \overline{\rho u_i u_j}}{\partial x_j} = -\frac{\partial \overline{p}}{\partial x_i} + \frac{\partial \widetilde{\sigma}_{ij}}{\partial x_j} \tag{6.4}$$

where

$$\widetilde{\sigma}_{ij} = -\frac{2}{3}\overline{\mu}\frac{\partial \widetilde{u}_k}{\partial x_k}\delta_{ij} + \overline{\mu}\left(\frac{\partial \widetilde{u}_j}{\partial x_i} + \frac{\partial \widetilde{u}_i}{\partial x_j}\right), \tag{6.5}$$

and μ is the local viscosity and $\bar{\rho}$, $\bar{p}$ are the filtered density and pressure, respectively. The non-linear term in Eq. 6.4 needs to be re-written in terms of $\widetilde{u}_i$ in order to close the above equation as follows:

$$\overline{\rho u_i u_j} = \overline{\overline{\rho}\,\widetilde{u}_i\widetilde{u}_j}^{e} + \left(\overline{\rho u_i u_j} - \overline{\overline{\rho}\,\widetilde{u}_i\widetilde{u}_j}^{e}\right) = \overline{\overline{\rho}\,\widetilde{u}_i\widetilde{u}_j}^{e} + \tau_{ij}, \tag{6.6}$$

where τ_{ij} is the subfilter stress and needs to be modeled. Explicit filtering enters the calculation through the secondary filtering in this decomposition,

denoted as $\overline{\cdot}^e$, which is applied at each time step. In a physical sense, this is equivalent to removing all the high wavenumber content from the nonlinear product of the velocity components.

The resulting momentum transport equation to be solved appears as

$$\frac{\partial \overline{\rho}\widetilde{u}_i}{\partial t} + \frac{\partial \overline{\overline{\rho}\,\widetilde{u}_i\widetilde{u}_j}^e}{\partial x_j} = -\frac{\partial \overline{p}}{\partial x_i} + \frac{\partial \widetilde{\sigma}_{ij}}{\partial x_j} - \frac{\partial \tau_{ij}}{\partial x_j} \tag{6.7}$$

where the subfilter stress is modeled using a Smagorinsky-type closure as follows

$$\tau_{ij} - \frac{1}{3}\tau_{kk}\delta_{ij} = -\overline{2\mathcal{C}_s\overline{\rho}\Delta^2|\overline{S}|\left(\overline{S}_{ij} - \frac{1}{3}\overline{S}_{kk}\delta_{ij}\right)}^e. \tag{6.8}$$

$\overline{S}_{ij}$ is a component of the resolved strain-rate tensor and $|\overline{S}|$ is its magnitude. The coefficient $\mathcal{C}_s$ is obtained using a dynamic formulation adapted for the explicit filtering approach [40]. From the above expression, it is seen that the subfilter stress term is explicitly filtered in order to ensure that it does not possess spectral content at wavenumbers higher than that corresponding to the filter width.

Conserved scalar models have become popular for performing LES of turbulent combustion due to their reduced computational cost and excellent performance in canonical experimental flows [106, 107, 21, 29, 7, 27]. These models use mixture fraction, which is a measure of the local fuel to air ratio, to map the gas phase thermochemical composition vector. In the flamelet-based approach, an one-dimensional representation of the flame is used to relate mixture fraction to the composition vector. In the context of LES, the filtered mixture fraction along with measures of subfilter mixing such as

variance and dissipation rate are used to obtain the filtered thermochemical composition vector as well as the fluid density. The main objective of this work is to determine the effect of numerical errors on the performance of models for variance and dissipation rate.

Analogous to the final form for momentum transport in Eq. 6.7, the explicitly-filtered transport equation for filtered mixture fraction is given by

$$\frac{\partial \bar{\rho}\widetilde{Z}}{\partial t} + \frac{\partial \overline{\bar{\rho}\ \widetilde{u}_i \widetilde{Z}}^e}{\partial x_i} = \frac{\partial}{\partial x_i}\left[\ \overline{\rho}\widetilde{D}\frac{\partial \widetilde{Z}}{\partial x_i}\ \right] - \frac{\partial M_{Z,i}}{\partial x_i} \tag{6.9}$$

where $M_{Z,i}$ denotes the subfilter scalar flux term $\overline{\rho u_i Z} - \overline{\bar{\rho}\ \widetilde{u}_i \widetilde{Z}}^e$.

Similar to the subfilter stress term in Eq. 6.8, the subfilter scalar flux term is modeled using a gradient-diffusion hypothesis and a dynamic procedure to estimate the associated model constant. The modeled flux could then be written as

$$M_{Z,i} = \overline{-2\mathcal{C}_Z \bar{\rho}\Delta^2 |\overline{S}| \frac{\partial \widetilde{Z}}{\partial x_i}}^e . \tag{6.10}$$

Grouping the leading terms into a turbulent diffusivity allows the filtered mixture fraction transport equation to be written as

$$\frac{\partial \bar{\rho}\widetilde{Z}}{\partial t} + \frac{\partial \overline{\bar{\rho}\ \widetilde{u}_i \widetilde{Z}}^e}{\partial x_i} = \frac{\partial}{\partial x_i}\left[\ \overline{\rho}\widetilde{D}\frac{\partial \widetilde{Z}}{\partial x_i} + \overline{\rho D_T \frac{\partial \widetilde{Z}}{\partial x_i}}^e\ \right] \tag{6.11}$$

where the secondary filtering on the subfilter flux term is retained due to the non-linearity of the product.

6.2 Scalar Variance Modeling

Small-scale mixing, which needs to be modeled in LES, is described using two fields - the subfilter variance and dissipation rate. Both these quantities are modeled using filter-scale quantities, and numerical errors at the near filter-width scales will strongly impact accuracy [34, 35, 44]. The subfilter scalar variance of the conserved scalar Z is defined as

$$Z_v = \widetilde{Z^2} - \widetilde{Z}^2, \tag{6.12}$$

and cannot be obtained only from the resolved mixture fraction due to the first term on the right hand side. There are two kinds of models available for variance: a) algebraic models based on a local equilibrium assumption, and b) transport equation models. The former class of models are commonly used since they are easily amenable to dynamic modeling of the coefficients that appear in the formulations, but introduce errors due to the assumption that production and dissipation of variance are balanced within each filter volume [34, 44]. The latter class of models transport variance in space and time and do not invoke an equilibrium assumption but are hampered by the need to specify model coefficients. Recently, Kaul and Raman have introduced a dynamic procedure for transport equations [108, 44]. The most widely used algebraic model, henceforth denoted as the classic dynamic model (CDM), is based on a gradient-squared scaling law [99]:

$$Z_v = \mathcal{C}_v \Delta^2 \frac{\partial \widetilde{Z}}{\partial x_i} \frac{\partial \widetilde{Z}}{\partial x_i}, \tag{6.13}$$

where the coefficient $\mathcal{C}_v$ is usually estimated dynamically [99, 109]. The gradient of mixture fraction is highly sensitive to near filter-width scales, and any contamination through numerical evolution of the scalar or differentiation will affect results. Kaul et al. [34, 35] have shown that these errors lead to non-intuitive behavior of the model, where some lower order finite difference methods produce more accurate results than higher order methods.

Transport equation models for variance require the solution of an additional scalar transport equation, either for the scalar second moment $\widetilde{Z^2}$ or for the subfilter scalar variance [110, 34]. While both the forms are equivalent in the continuous sense, it has been shown that the second moment transport equation (STE) is numerically superior to the variance transport equation (VTE) [34, 35]. Starting with the transport equation for Z^2, it is possible to derive the STE by convolving this equation with the filter form (Eq. 6.1).

$$\frac{\partial \overline{\rho}\widetilde{Z^2}}{\partial t} + \frac{\partial \overline{\overline{\rho}\ \widetilde{u}_i \widetilde{Z^2}}^e}{\partial x_i} = \frac{\partial}{\partial x_i}\left[\overline{\rho}\widetilde{D}\frac{\partial \widetilde{Z^2}}{\partial x_i} + \overline{\overline{\rho} D_T \frac{\partial \widetilde{Z^2}}{\partial x_i}}^e \right] - \overline{\rho}\widetilde{\chi}_Z, \tag{6.14}$$

where $\widetilde{\chi}_Z$ is the dissipation rate of variance, given in exact form by

$$\widetilde{\chi}_Z = 2D\frac{\widetilde{\partial Z}}{\partial x_j}\frac{\partial Z}{\partial x_j}. \tag{6.15}$$

The filtered dissipation rate, as defined above, is an interesting quantity. In high-Reynolds number flows, scalar energy dissipation will happen predominantly at the small scales. In other words, the resolved contribution to dissipation rate will be negligible. If the dissipation rate is filtered using a low-pass filter, this filtered rate will be very close to zero. For this reason,

the filtered dissipation rate that appears in the STE equation should be seen as an "effective" dissipation rate that represents the effect of small scale dissipation on the second moment in a given filter volume. Since this dissipation rate should only affect the filter-scale quantity, it cannot exhibit scales smaller than the filter width. Hence, any model used for dissipation rate should also be explicitly filtered to remove small-scale energy.

For application in explicitly-filtered LES, the filtered dissipation rate is modeled in the form

$$\overline{\rho}\widetilde{\chi}_Z = \overline{\mathcal{C}_\tau \overline{\rho} \frac{\widetilde{D} + D_T}{\Delta^2} Z_v + 2\overline{\rho}\widetilde{D} \frac{\partial \widetilde{Z}}{\partial x_i} \frac{\partial \widetilde{Z}}{\partial x_i}}^e \tag{6.16}$$

where the first term on the right hand side represents the sub filter contribution, which is considered proportional to the variance and inversely proportional to a mixing timescale, commonly defined as the ratio of square of filter width to total diffusivity. The entire term is explicitly-filtered to remove subfilter-scale energy.

Alternately, the filtered dissipation rate can be modeled using an algebraic closure as

$$\widetilde{\chi}_Z = \overline{2(\widetilde{D} + D_T) \frac{\partial \widetilde{Z}}{\partial x_i} \frac{\partial \widetilde{Z}}{\partial x_i}}^e \ . \tag{6.17}$$

This model, similar to the algebraic variance model, is most susceptible to numerical errors since it contains the gradient-squared term that is heavily contaminated by filter-level numerical discretization error.

In grid-filtered LES, the VTE model could be derived starting with the STE model and subtracting the transport equation for $\widetilde{Z}^2$. A similar

approach here is possible, but will lead to a variance transport equation that is considerably different from the convective-diffusive form of the STE or scalar transport equations. An alternate approach is based on the idea that the explicit filtering operation is designed to remove small scale energy. The VTE is derived as in the grid-filtered LES formulation, but all terms that could generate small-scales are explicitly filtered at each time step. This results in the following form the VTE:

$$\frac{\partial \bar{\rho} Z_v}{\partial t} + \frac{\partial \overline{\bar{\rho}\, \widetilde{u}_i Z_v}^e}{\partial x_i} = \frac{\partial}{\partial x_i} \left[\bar{\rho} \widetilde{D} \frac{\partial Z_v}{\partial x_i} + \overline{\bar{\rho} D_T \frac{\partial Z_v}{\partial x_i}}^e \right] + \mathcal{P} - \widetilde{\epsilon}_Z \tag{6.18}$$

where $\mathcal{P}$ and $\widetilde{\epsilon}_Z$ represent the production and dissipation of subfilter mixture fraction variance, respectively. For our purposes, the production term will be modeled using a gradient-diffusion hypothesis

$$\mathcal{P} = \overline{2 \bar{\rho} D_T \frac{\partial \widetilde{Z}}{\partial x_i} \frac{\partial \widetilde{Z}}{\partial x_i}}^e \tag{6.19}$$

and dissipation will be closed in the form

$$\widetilde{\epsilon}_Z = \overline{\mathcal{C}_\tau \bar{\rho} \frac{\widetilde{D} + D_T}{\Delta^2} Z_v}^e \tag{6.20}$$

6.3 Modified Dynamic Modeling

Closure of Eq. 6.11 and Eq. 6.13 requires models for the eddy diffusivity D_t and the dynamic variance model coefficient $\mathcal{C}_v$. The conventional dynamic procedure has to be altered to account for the explicit filtering operation [37]. In the expression below, $\widehat{(\cdot)}$ indicates spatial test filtering at a filterwidth $\hat{\Delta}$

while $\check{(\cdot)}$ indicates the Favre test filtering operation, i.e. $\check{f} = \widehat{\rho\widetilde{f}}/\widehat{\overline{\rho}}$. The ratio $\hat{\Delta}/\Delta = 2$ is used here.

$$\left[\widehat{\overline{\rho}\widetilde{u}_i\widetilde{Z}} - \widehat{\overline{\rho}}\widehat{\check{u}_i}\check{Z}\right] = \mathcal{C}_Z \left[\widehat{\overline{\rho}\Delta^2|\widetilde{S}|\frac{\partial\widetilde{Z}}{\partial x_i}} - \widehat{\overline{\rho}}\widehat{\hat{\Delta}^2|\check{S}|}\frac{\partial\check{Z}}{\partial x_i}\right] \tag{6.21}$$

Letting $\mathcal{L}_{Z,i}$ and $\mathcal{M}_{Z,i}$ denote, respectively, the bracketed quantities on the left- and right-hand sides of Eq. 6.21, the model coefficient is estimated by $\mathcal{C}_Z = \langle \mathcal{L}_{Z,i}\mathcal{M}_{Z,i}\rangle \,/\, \langle \mathcal{M}_{Z,i}\mathcal{M}_{Z,i}\rangle$. Brackets $\langle\cdot\rangle$ indicate some averaging operation whose precise definition depends on the flow configuration.

6.4 Discrete Filters

An important component of the simulations is the application of the explicit filter at each time step. As in prior work [37, 40, 43, 42], the filtering operation is never applied directly to the variables that are being solved for, but only to specific terms in the evolution equations. This is mainly due to the fact that filters used here are only spectral-like and do not provide sharp cut-off in spectral space. Instead of cleanly removing the energy, the filters redistribute energy above the filter scale. Hence, directly filtering the solution will result in excessive smoothing. For the same reason, it is important to ensure that the simulations are initialized with minimal energy content at the small scales. This will prevent pile-up of energy that is not removed by the discrete filter.

As proposed by Vasilyev et al. [37], the explicit filtering operation in

one dimension is implemented as a weighted sum of values

$$\overline{\phi}_j^e = \sum_{n=-K_j}^{L_j} w_n^j \phi_{j+n} \tag{6.22}$$

where at grid point j, $\overline{\phi}_j^e$ is a general filtered quantity, ϕ_{j+n} is the unfiltered value at the n^{th} point in the filter stencil, and w_n is the coefficient associated with that respective position. This definition allows asymmetric stencils, where $K_j \neq L_j$, for application near boundaries, as well as variable stencil definitions throughout the domain. Explicit filtering in three dimensions is considered as a tensor product of three one-dimensional filtering operations in each direction as follows

$$\Phi_1(x_i, y_j, z_k, t) = \sum_{n=-K_i}^{L_i} w_n^i \phi(x_{i+n}, y_j, z_k, t) \tag{6.23}$$

$$\Phi_2(x_i, y_j, z_k, t) = \sum_{n=-K_j}^{L_j} w_n^j \Phi_1(x_i, y_{j+n}, z_k, t) \tag{6.24}$$

$$\overline{\phi}^e(x_i, y_j, z_k, t) = \sum_{n=-K_k}^{L_k} w_n^k \Phi_2(x_i, y_j, z_{k+n}, t) \tag{6.25}$$

where Φ_1 and Φ_2 are intermediate arrays following respective one-dimensional filtering operations.

The stencil width, or the number of adjacent discrete points required for filtering, is prescribed based on the FGR. For the configurations considered in this work, primarily periodic and uniform cartesian grids are used, allowing for a single symmetric stencil to be applied universally for a given FGR. Solutions are obtained for FGR values ranging from one to eight. However, due to test

filtering operations required for dynamic modeling, filter stencils are defined for FGR values as high as 16. Each associated set of coefficients is determined based on a desired order of commutation error and a spectral cutoff target function as proposed by Vasilyev et al. [37] and can be found in Appendix C.

Plotting the Fourier transform of the discrete filter stencils in Fig. 6.1 reveals that, while the effective cutoff wavenumber varies relative to grid size, they are qualitatively indistinguishable at low wavenumbers when scaled by the corresponding filter width. However, when plotted in log scale, the high wavenumber content of the transfer function is not identically zero. This prevents the filtering operation from completely removing small scale energy and results in the progressive accumulation of subfilter scales, as will be shown in Sec. 7.1.

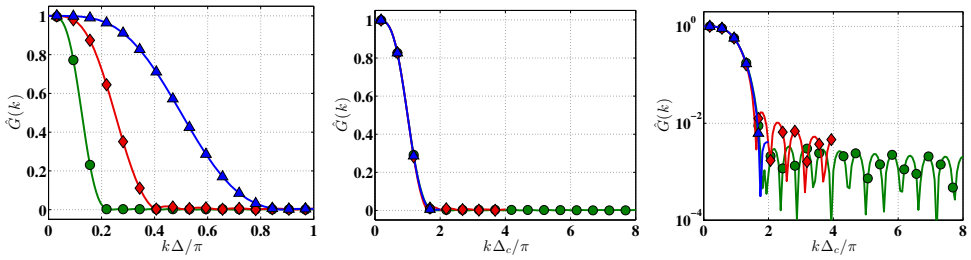

Figure 6.1: Filter transfer function in spectral space for FGRs of two (blue square), four (green circle) and eight (red diamond). Profiles are plotted linearly against grid wavenumber (left), linearly against filter-scale wavenumber (center) and logarithmically against filter-scale wavenumber

Chapter 7

Scalar Mixing Results for Explicitly Filtered LES

In this study, two different configurations will be considered. The first is a simulation of homogeneous isotropic turbulence (HIT) in a periodic box, while the second considers a temporal shear layer with two periodic directions and mean velocity and scalar gradients in the stream-normal direction. Both cases use a finite-volume approach for momentum and scalar transport, applying the discrete filter to all terms previously noted. The first case uses a canonical configuration but with the practical application of physical space discretization as well as accounting for the velocity errors. The second case contains a directional gradient that is common in most practical applications.

7.1 HIT Using Finite-Volume Method

7.1.1 Simulation Details

Decaying isotropic turbulence cases are used to understand model errors in a canonical flow configuration. The explicit filter is applied to both the filtered momentum and scalar equations, thereby characterizing the interaction of the numerical errors. A low-Mach number approach with a pressure-projection based algorithm is used [26, 111]. The low-Mach number solver uses

second-order central difference schemes for the momentum equations (both convective and viscous terms) and a third-order upwind QUICK scheme [112] for scalar advection. Scalar diffusion is discretized using a second-order central difference scheme. The pressure-projection algorithm and its implementation are discussed in [26, 71]. A series of simulations are conducted with this flow configuration and solver. To investigate the effect of filter width on model behavior, three sets of results were obtained with $\Delta_1 = 2\pi/16,\ \Delta_2 = 2\pi/32$ and $\Delta_3 = 2\pi/64$. For each of these filter widths, multiple FGR values were tested. For the larger two filter widths ($\Delta_1,\ \Delta_2$), simulations with FGR = 1, 2, 4 and 8 were conducted, while FGR = 1, 2 and 4 were used for the smallest filter width (Δ_3). Grid sizes for each case are listed in Table 7.1.

Table 7.1: Number of grid points in one direction (N_x) for explicit LES of HIT for each filter width ($\Delta_1, \Delta_2, \Delta_3$) and FGR.

Δ_i	1	1	1	1	2	2	2	2	3	3	3
FGR	1	2	4	8	1	2	4	8	1	2	4
N_x	16	32	64	128	32	64	128	256	64	128	256

To avoid inconsistency in the rate of scalar mixing between different filter width simulations due to linear forcing of the finite-volume solution, decaying HIT is investigated. However, in order to obtain comparable initial conditions for all explicitly filtered simulations, three implicit LES cases of forced HIT are conducted independently with the grid size set to the respective filter widths and a linear forcing coefficient of 0.5 [113]. With this procedure, identical domain average turbulent kinetic energy values are obtained for the initialization of the explicit filtering runs, resulting in Re_λ values of 38, 63 and

105 for Δ_1, Δ_2 and Δ_3, respectively. This results in filter width to Kolmogorov scale ratios (Δ/η) between 8 and 9 for all cases considered. The unmixed scalar field is then initialized on the finest implicit LES mesh and linearly interpolated to the two coarser grids. For each filter width case, the velocity and scalar fields are translated to finer grids for non-unity FGR values by zero-padding the discrete Fourier transform. This provides exact spectral replication up to the highest wavenumber resolved on the respective grids for a FGR = 1. The resulting turbulent energy and scalar energy spectra are displayed in Fig. 7.1. This initialization procedure was deemed important to ensure that most of the fine scale energy at scales smaller than the filter width is removed at the initial condition.

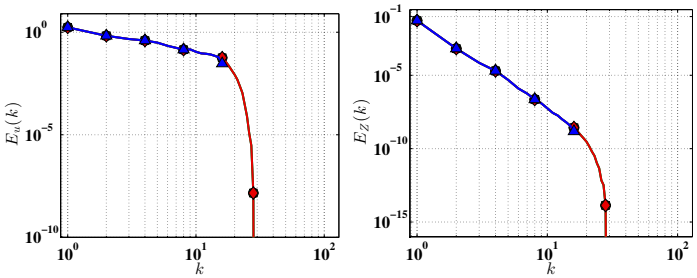

Figure 7.1: Initial turbulent energy spectra (left) and scalar energy spectra (right) for an effective filter width of $2\pi/32$ with FGRs of one (blue triangle), two (red diamond), four (green circle) and eight (cyan square).

The simulations used dynamic models for turbulent viscosity and diffusivity, modified for the explicit filtering procedure [37, 40]. The dynamic model for variance (CDM) (Eq. 6.13), the STE (Eq. 6.14) and VTE (Eq. 6.18)were solved. In addition, the equilibrium model for scalar dissipation rate (Eq. 6.17) was evaluated.

7.1.2 Large Scale Mixing Process

Figure 7.2 shows the evolution of the volume averaged velocity RMS. It is seen that the initialization procedure described above leads to comparable initial values for these averages. In addition, their evolution appears independent of the FGR or filter width. Since these quantities are dominated by the large scale spectral content, it appears that the numerical errors do not significantly affect the large scale evolution.

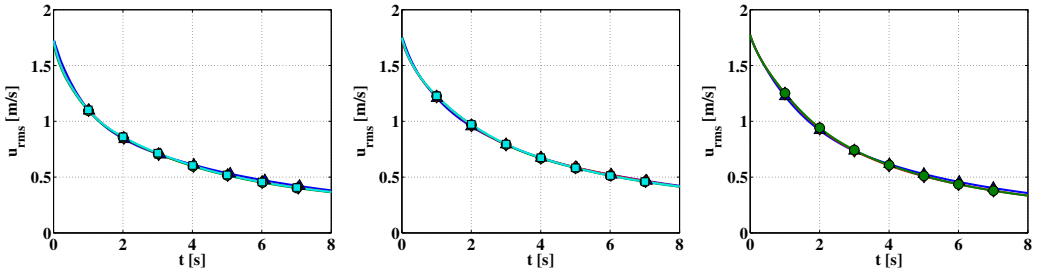

Figure 7.2: Evolution of volume averaged RMS velocity at effective filter widths of $2\pi/16$ (left), $2\pi/32$ (middle) and $2\pi/64$ (right) with FGRs of one (blue triangle), two (red diamond), four (green circle) and eight (cyan square).

Figure 7.3 shows the evolution of the turbulent and scalar energy spectra for the different filter widths and FGR cases. The turbulent energy spectrum corresponds to decaying fluctuations, where energy at higher wave numbers is attenuated faster. It is also seen that the explicit filtering approach, though effective in limiting scales, leaves residual energy in the small scales. This is an artifact of the spatial reconstruction of the sharp-spectral cutoff filter. However, the residual energy is several orders of magnitude smaller than the integral scale energy content. Figure 7.4 shows the same data plotted to

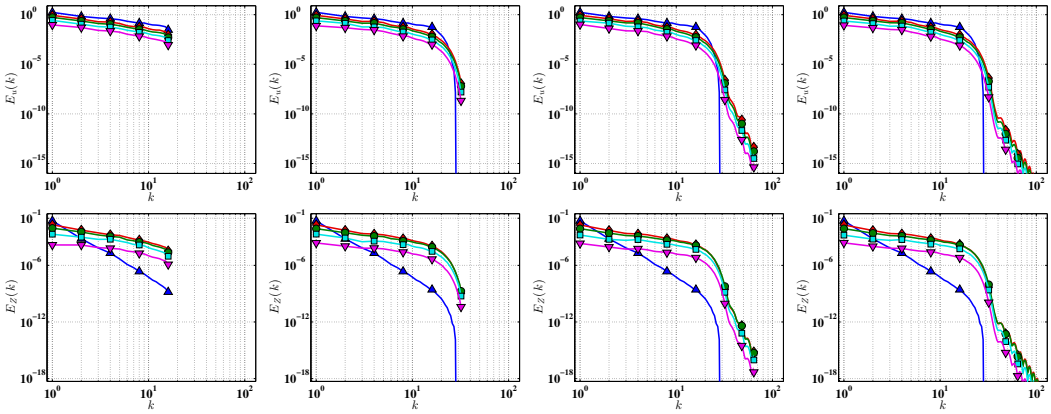

Figure 7.3: Turbulent energy spectra (top) and scalar energy spectra (bottom) with FGRs of one, two, four, and eight (left to right) at times of zero (blue triangle up), one (red diamond), two (green circle), four (cyan square) and eight (magenta triangle down) seconds for an effective filter width of $2\pi/32$.

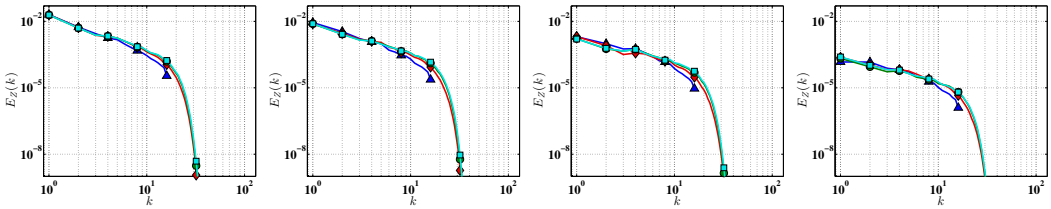

Figure 7.4: Scalar energy spectra at times of one, two, four and eight seconds (left to right) for FGRs of one (blue triangle), two (red diamond), four (green circle) and eight (cyan square) for an effective filter width of $2\pi/32$.

compare various FGR values at given times. It is seen that the decay rate of the spectrum collapses beyond a FGR = 1.

Figure 7.5 shows the instantaneous contours of mixture fraction for four different times and the different FGRs with an effective filter width of $2\pi/32$. From the plots, it is seen that as the FGR increases, the evolution appears to converge with very similar structures (more quantitative features will be discussed below). Interestingly, it is seen that the size of the smallest length

scales that appear in the different FGRs do not decrease very much, indicating that the explicit filtering of all nonlinear terms reduces the generation of small-scale structures. However, the different FGR cases alter the evolution from the initial conditions. With an increase in FGR, there is a convergence of the scalar evolution with very similar structures found in the FGR of four and eight cases.

For comparison purposes, an implicitly filtered (i.e., grid filtered) LES is also shown in Fig. 7.6 for the Δ_2 case at the same grid resolution as a FGR = 8. As expected, the grid-filtered LES generates scalars that are comparable to the grid size starting from the same initial conditions. From these data, it can be concluded that the explicit filtering operation effectively limits the range of scales in LES while separating the mesh and filter sizes.

7.1.3 Turbulence Modeling

Figure 7.7 shows the evolution of the dynamic model coefficients for the eddy viscosity and diffusivity models. The case with FGR = 1 clearly introduces numerical errors but even FGR = 2 is sufficient to remove most of these errors. The coefficients appear converged for all higher FGR values. Interestingly, the coefficients do not change although the turbulent kinetic energy and the scalar energy decay with time. The higher coefficient value for FGR = 1 partially compensates for the lower values obtained in the numerical evaluation of the filtered strain rate (see Eq. 6.8).This self-correcting nature of the dynamic procedure has been previously noted by Kaul et al. [34, 35]. As

seen in Fig. 7.2, the errors in the evaluation of the dynamic model coefficient do not seem to affect the decay rate of the turbulent kinetic energy substantially.

7.1.4 Subfilter Scalar Variance Model Convergence

Figure 7.8 shows the volume averaged subfilter variance as a function of time for the three different model formulations. As expected, the volume-averaged variance decreases with a decrease in filter width for all three models. The dynamic model (CDM), however, consistently produces much smaller values of subfilter variance compared to the other two models. For the largest filter width case ($\Delta_1 = 2\pi/16$), the model coefficient obtained by averaging the local coefficient in homogeneous directions becomes negative. This leads to a sudden drop in variance to zero. This behavior of the model coefficient is well known and has been the subject of prior studies [114, 109, 44]. However, as the filter width is reduced, the model exhibits more robust behavior, with smaller difference in values between a FGR of four and eight for Δ_2.

The STE model is least affected by numerical errors by virtue of its construction (Eq. 6.14). The VTE model, in the continuous limit, is identical to the STE model. However, in discretized form, the VTE approach is more susceptible to numerical errors. This is mainly due to the production term that contains the product of the scalar turbulent diffusivity and the square of the scalar gradient (Eq. 6.19).

Overlaying the variance evolution of the FGR = 8 cases for VTE and STE models, as seen in Fig. 7.9, it can be seen that the profiles are nearly simi-

lar. Given that the STE model is relatively insensitive to numerical errors, this shows that the VTE model needs even higher FGRs to achieve convergence.

While volume-averaged quantities provide a statistical measure for comparison, it is instructive to look at the distribution of subfilter variance in the domain. Figure 7.10 shows the evolution of the subfilter variance with time. The dynamic model has a characteristically different PDF compared to the VTE and STE models. In this sense, the dynamic model predicts predominantly small variance values throughout the domain, while the VTE and STE models show distinct peaks that move from higher to lower variance values with time. The PDF of the dynamic model depends entirely on the scalar distribution since it has no direct time dependence. The STE and VTE models, although linked to the mixture fraction equation through the production and/or dissipation terms, also contain a time-dependence through the time derivative in the transport equation (Eq. 6.14 and 6.18). Thus, it is not surprising that the PDFs are different. From the combustion standpoint, however, this difference has very profound implications. The dynamic model indicates that the subfilter scalar distribution is more uniform or that the scalar is molecularly mixed to a greater extent. This could either accelerate chemical reactions in regions where the flame is fully stable or lead to extinction through increased mixing.

Figure 7.11 shows the effect of the FGR on the prediction of scalar variance distribution. For the dynamic model, lower FGRs lead to lower variances, which is reflected in the increase of the PDF value at small variances. Consis-

tent with the increase in the mean variance followed by decay, the PDF shifts to the right between one and two seconds, followed by a leftward shift between two and four seconds. The STE model, similar to previous observations, does not show significant variation with FGR. The VTE model shows the largest variation with FGR, shifting the distribution towards higher variance values as the FGR is increased. Figure 7.12 shows the convergence of the VTE and STE PDFs for the largest FGR considered. Although there are differences, it shows that the VTE model produces roughly the same PDF as the STE model.

7.2 Temporal Shear Layer

7.2.1 Configuration Details

In order to investigate the impact of inhomogeneous turbulence on the explicit filtering process, temporally evolving shear layers are simulated for a range of LES resolutions. Figure 7.13 provides schematic of the flow configuration considered here. Scalar values are initialized to one in the core flow and zero in the coflow. The core and the coflow have equal but opposite velocities, providing a stationarity in space. The current study considers a Reynolds number of 20,000 based on core thickness (H) and velocity difference. The computational domain spans $16H \times 12H \times 4H$ in the streamwise, stream-normal, and spanwise directions, respectively. The grid is uniform and equal in each direction with periodic boundary conditions in the streamwise and spanwise directions. The different FGRs and grid sizes used in this study

are provided in Table 7.2.

Table 7.2: Configuration parameters for temporal jet simulations.

FGR	N_x	N_y	N_z
1	128	96	32
2	256	192	64
4	512	384	128

In order to ensure that a turbulent shear layer develops, implicit LES with the same grid resolution as the FGR = 2 case is evolved from the initial conditions until a linear shear layer growth is established. From this data, velocity fields are linearly interpolated to the grid for FGR = 1. For the cases with a non-unity FGR, the velocity field is then interpolated from the FGR = 1 field. This ensures that there is only limited small-scale energy. Note that as seen in the HIT initial conditions, interpolation from the coarser to finer grid will introduce some small-scale energy. Scalar fields are reinitialized in the core to uniform fields with smooth interfaces using a hyperbolic tangent profile, to ensure that subfilter scales are minimized in all initial conditions and that all explicit LES results have comparable mean quantity evolution. These initial profiles are shown in Fig. 7.14. Using the non-dimensionalized time $t^* = t\Delta U/H$, where ΔU is the initial velocity difference, further results show instantaneous and average results at $t^* = 1$, 2 and 4. The statistics shown in this section are obtained by averaging in the periodic directions at a given time instance.

7.2.2 Turbulent Energy Characteristics

The convergence of resolved turbulent and scalar energy (Fig. 7.15) is similar to that observed for the HIT case. There is very little variation with FGR indicating that the large scale mean flow statistics are immune to numerical errors in a non-reacting flow. Turbulent model quantities for viscosity and diffusivity, which depends on the gradient of the velocity field, also shows minimal variation, as seen in Fig. 7.16. This indicates that the determination of the dynamic model coefficient suppresses the effect of numerical errors, an effect discussed elsewhere [34, 35].

7.2.3 Filtered Scalar Dissipation Rate

Figures 7.17 and 7.18 shows instantaneous dissipation rates for the algebraic (Eq. 6.17 and STE (Eq. 6.16) models, respectively. Increasing the FGR clearly increases the magnitude of the gradients for both models, but the structure of the dissipation rate differs between the descriptions. It is also seen that the highest dissipation rates are confined to very thin regions, consistent with the previous observation that dissipation rate is dominated by small-scale behavior (in LES, this would be the filter-scale). The transport equation consistent models predict a more spread-out dissipation rate structure. This is mainly due to the fact that the transport of variance introduces scalar energy in regions away from the shear/mixing layer, which persists for significant time before being dissipated. The dissipation rate, being proportional to variance, reflects this behavior. More importantly, it is seen that even for the STE

model, the dissipation rate remains sensitive to FGR, although the variance itself is relatively insensitive. It could be inferred that the predominant dissipation of variance in the STE model occurs due to small-to-mid range values of dissipation rate. The high dissipation rate structures also tend to evolve at a much faster timescale and may not have a significant impact on the overall reduction of variance.

Another aspect of explicit filtering appears in the scalar dissipation rate plots (Fig. 7.18). For the highest FGR cases and at longer simulation times, there is a noticeable pile-up of small scale energy at scales slightly smaller than the filter scale. This is essentially due to the imperfections of the spatial version of spectral cut-off filter. Since the filter is truncated in physical space, it contains oscillations in the transfer function at high wavenumbers (Fig. 6.1 in Sec. 6.4). These oscillations could also be the result of inadequate subfilter turbulent dissipation, which is modeled using the turbulent viscosity (diffusivity) terms in the momentum (scalar) equations, respectively. With an increase in FGR, the importance of small-scale models increases since numerical diffusion is no longer sufficiently active to augment small-scale dissipation. Regardless, these fluctuations are not sufficiently large to be of concern for the FGRs shown here.

7.2.4 Subfilter Scalar Variance Model Performance

The CDM, VTE and STE models for scalar variance are compared here, building on the analysis of the HIT results. Figure 7.19 shows the spatially-

averaged stream-normal variance of mixture fraction for the CDM. At the earliest time shown, an increase in FGR leads to progressive convergence although there is still some variation between the FGR of two and four cases. However, at later times, the behavior is not smooth with regard to grid refinement. In particular, the highest FGR calculation shows large variations near the center of the domain. This behavior is caused by the dynamic model calculation, which uses differences at the test filter and filter level quantities to estimate the model coefficient. Figure 7.20 shows the model coefficients obtained for the different FGRs at corresponding times to Fig. 7.19. It is seen that the highest FGR case has large coefficient variations near the center of the jet. Even for the HIT case (Fig. 7.8), the CDM resulted in the variance dropping to zero at later times primarily due to the model coefficient becoming zero or negative. Prior studies [44] have shown that the homogeneous direction based averaging used in the dynamic procedure affects model evaluation. Since the spatial averaging used here is arbitrary, it is plausible that other types of averaging (e.g., conditional averaging or optimal estimation [44]) might lead to better results. This aspect has not been explored here.

The VTE model variance (Fig. 7.21) shows a smoother variation with FGR but does not show convergence similar to the HIT configuration. The main issue here is the production term (Fig. 7.22) which is highly sensitive to numerical errors due to the gradient-squared term. Since the dissipation model is proportional to variance (Eq. 6.20), an underprediction of production leads to reduced dissipation as well (Fig. 7.23). It is also seen that at early times,

the dissipation rate is lower than the production rate on average, which leads to an increase in variance, while at later times, this trend is reversed. If the difference between production and dissipation is considered, it could be seen that at lower FGR values, the shift to dissipation dominated variance evolution occurs earlier than for the higher FGR values. In a spatially evolving jet, this would imply faster jet mixing and a shorter flame (provided the dissipation rate is higher than the extinction dissipation rate). Further, the variance values themselves are much lower for the lower FGR simulation, which would further accelerate the modeled combustion process.

The STE model (Fig. 7.24), similar to the HIT case, shows very limited effect of FGR variation, indicating the numerical errors are effectively mitigated by the formulation. At early times, the unity FGR case produces a higher variance near the centerline compared to the other cases. This is mainly due to the under prediction of the resolved dissipation rate (Eq. 6.16) component of the sink term present in the STE model. At later times, as the scalar gradients become smaller, this effect vanishes and the variance is found to increase with FGR.

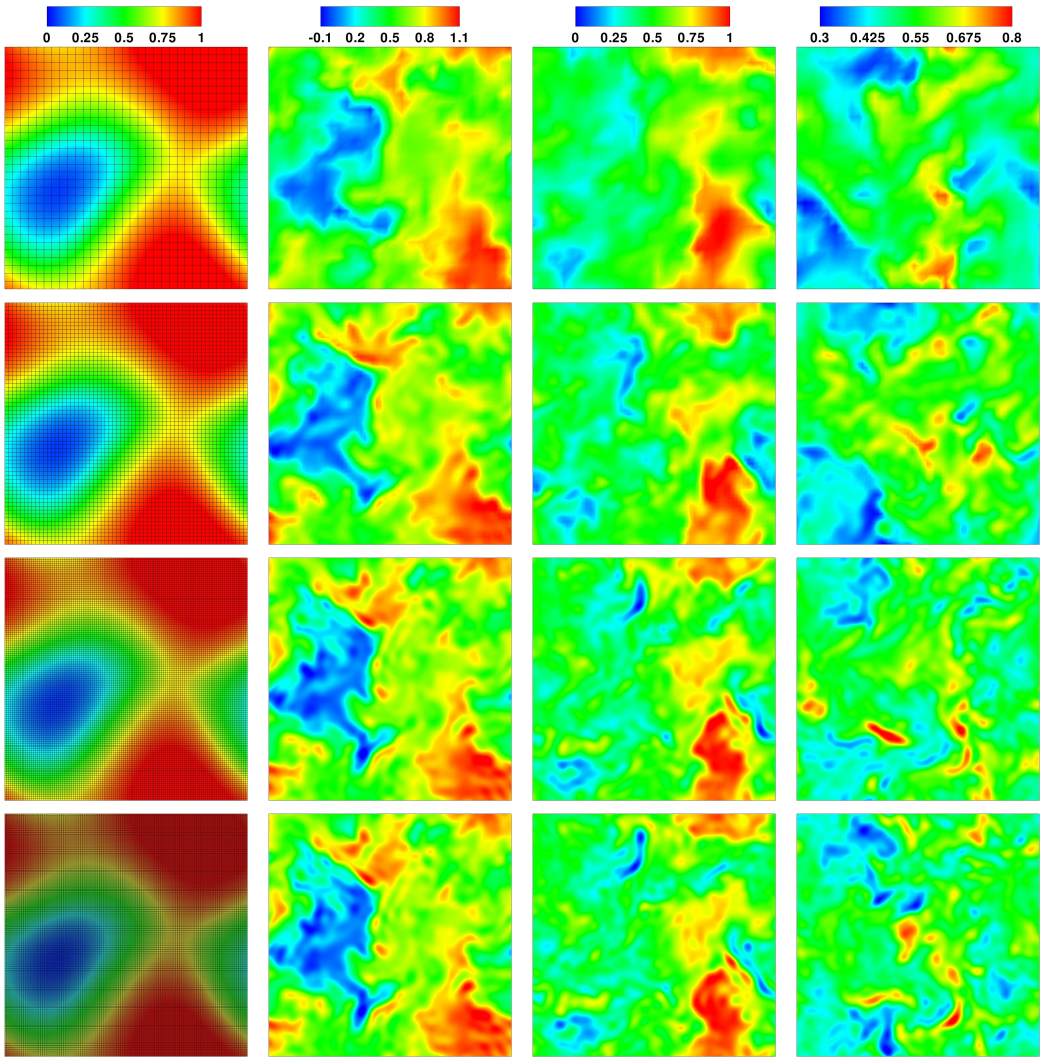

Figure 7.5: Instantaneous contours of mixture fraction at times of zero, one, two and four seconds (left to right) for FGRs of one, two, four and eight (top to bottom) for an effective filter width of $2\pi/32$.

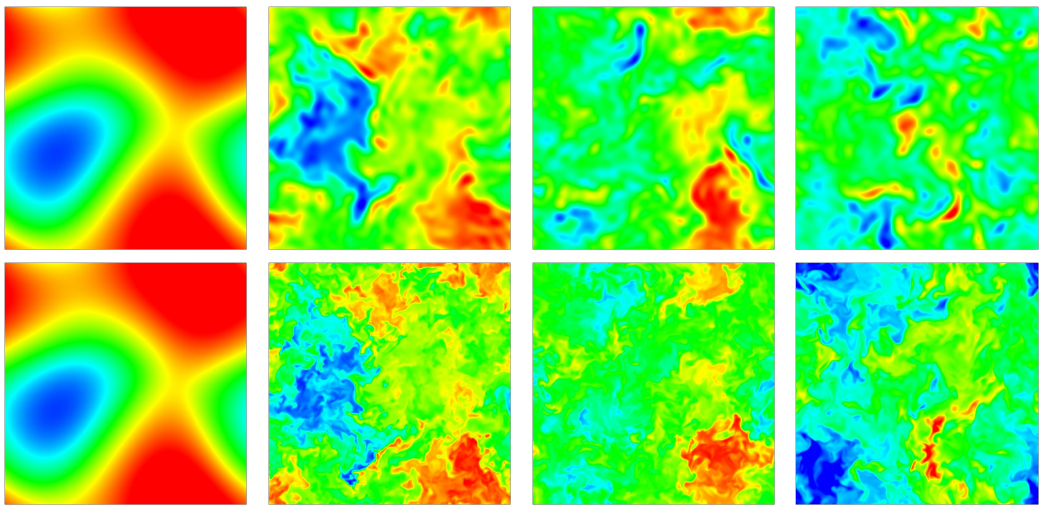

Figure 7.6: Instantaneous contours of mixture fraction at times of zero, one, two and four seconds (left to right) for a filter-to-grid ratio of eight (top) and implicitly filtered LES on the same grid (bottom) for an effective filter width of $2\pi/32$.

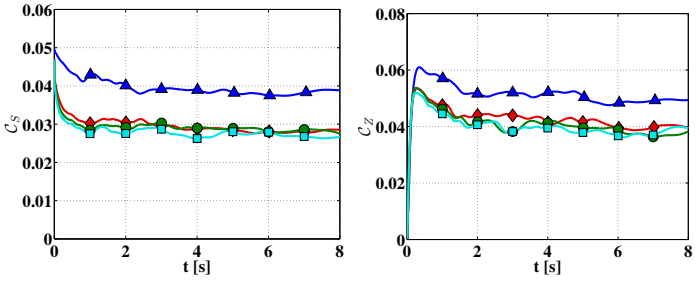

Figure 7.7: Coefficients of Smagorinsky-type eddy viscosity (left) and eddy diffusivity (right) with FGRs of one (blue triangle), two (red diamond), four (green circle) and eight (cyan square) for an effective filter width of $2\pi/32$.

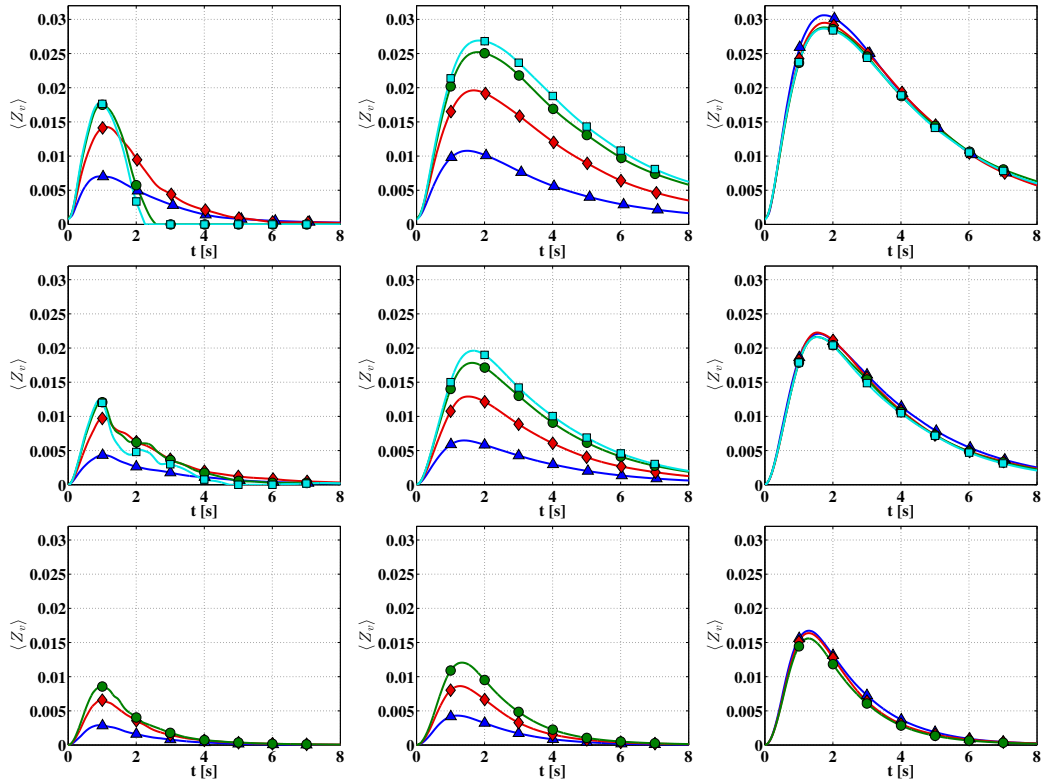

Figure 7.8: Evolution of volume integrated sub filter mixture fraction variance using the CDM (left), VTE (center) and STE (right) at effective filter widths of $2\pi/16$ (top), $2\pi/32$ (middle) and $2\pi/64$ (bottom) with FGRs of one (blue triangle), two (red diamond), four (green circle) and eight (cyan square).

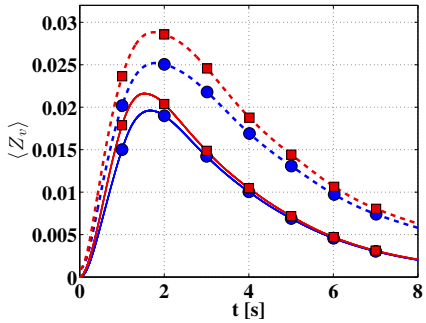

Figure 7.9: Evolution of sub filter variance using VTE (red square) and STE (blue circle) models with a FGR of eight for effective filter widths of $2\pi/16$ (dashed line) and $2\pi/32$ (solid line).

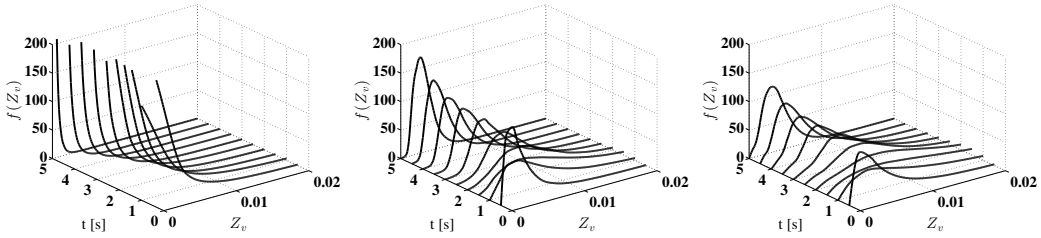

Figure 7.10: Time evolution of distribution of sub filter scalar variance values using CDM (left), VTE (middle) and STE (right) for an effective filter width of $2\pi/32$.

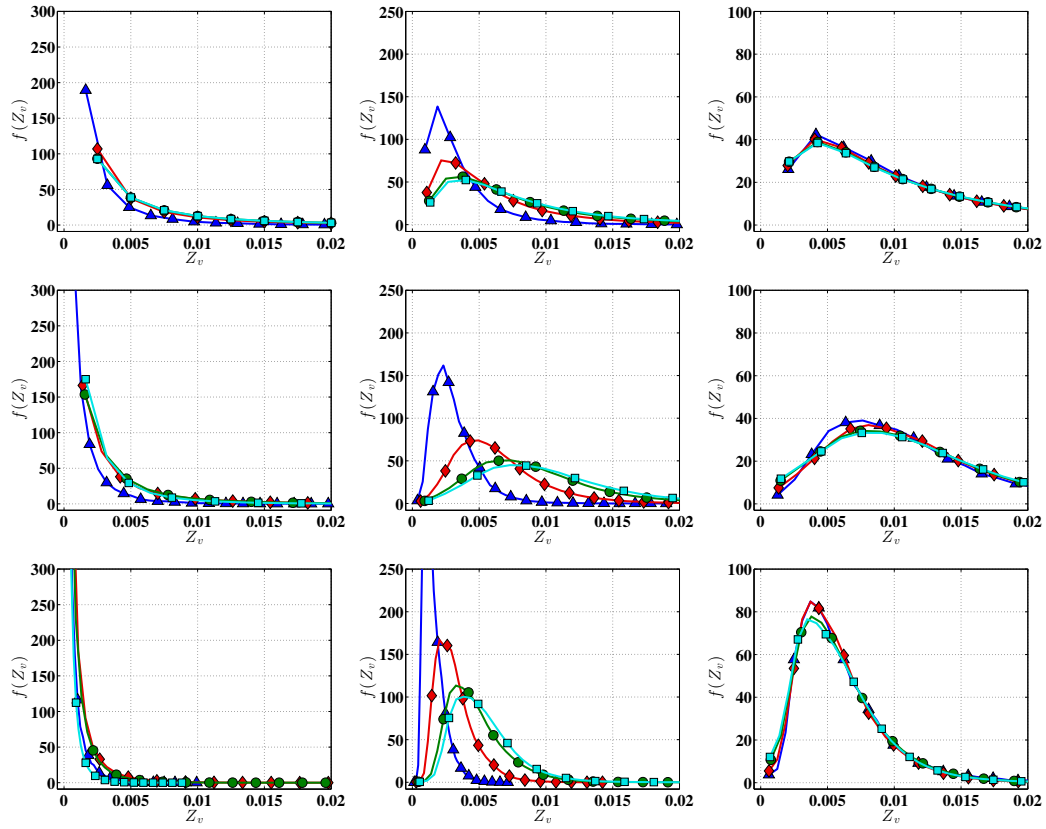

Figure 7.11: Distribution of sub filter scalar variance values using CDM (left), VTE (middle) and STE (right) with FGRs of one (blue triangle), two (red diamond), four (green circle) and eight (cyan square) at time in seconds of one (top), two (middle) and four (bottom) for an effective filter width of $2\pi/32$.

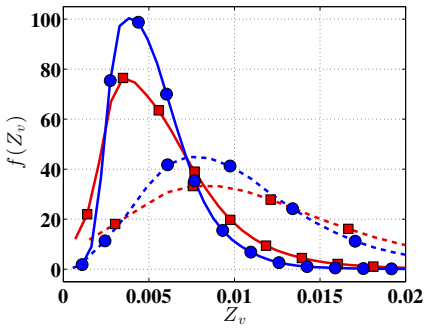

Figure 7.12: Distribution of sub filter scalar variance values using VTE (red) and STE (blue) models with a FGRs of eight. Flow times of two (dashed) and four (solid) seconds are considered.

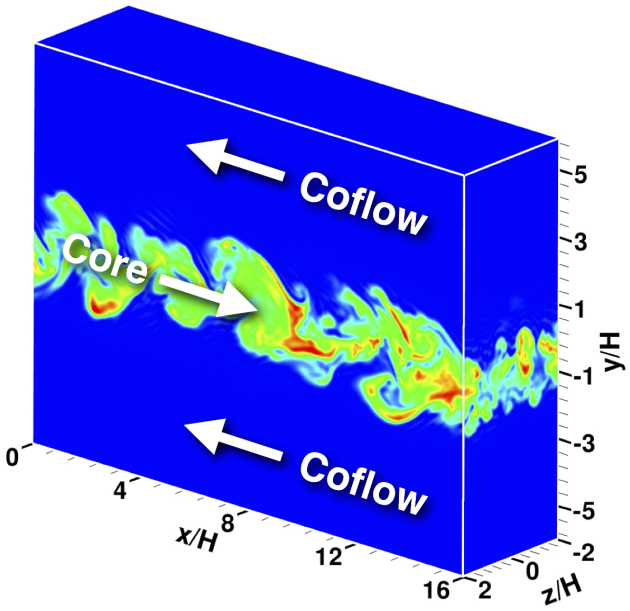

Figure 7.13: Flow configuration for the temporal jet simulations. Instantaneous contours of mixture fraction are displayed.

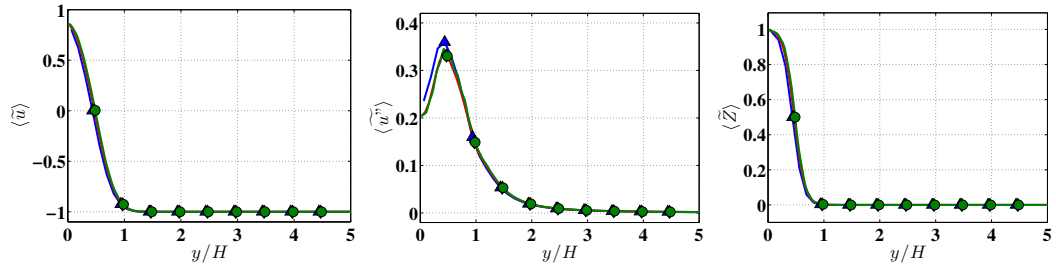

Figure 7.14: Initial conditions used for the explicitly-filtered LES. Average stream-normal profile for stream wise mean velocity (left), rms velocity (center) and filtered mixture fraction (right) for FGR values of one (blue triangle), two (red diamond) and four (green circle).

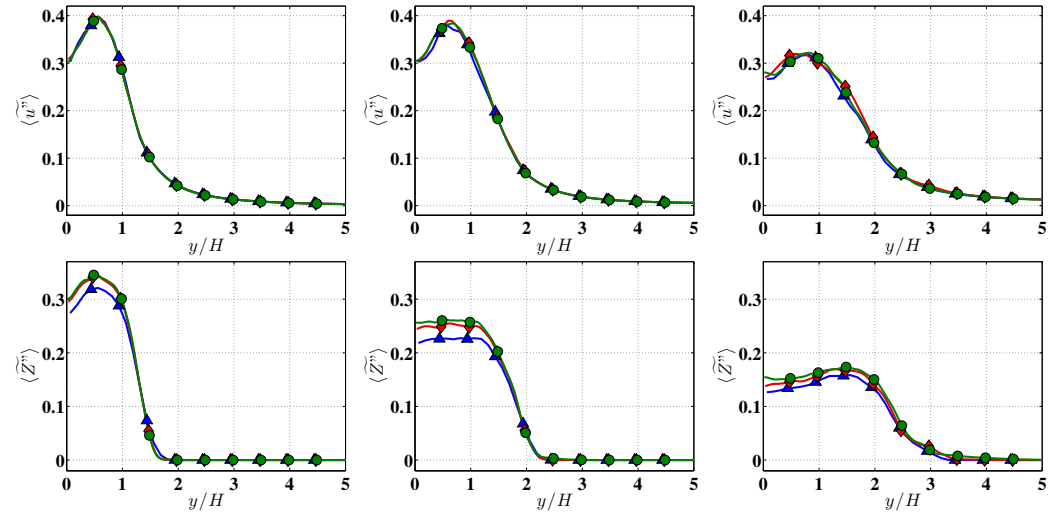

Figure 7.15: Average stream-normal profile of stream wise velocity rms (top) and mixture fraction rms (bottom) at times corresponding to t^* of one, two and four (left to right) for FGR values of one (blue triangle), two (red diamond) and four (green circle).

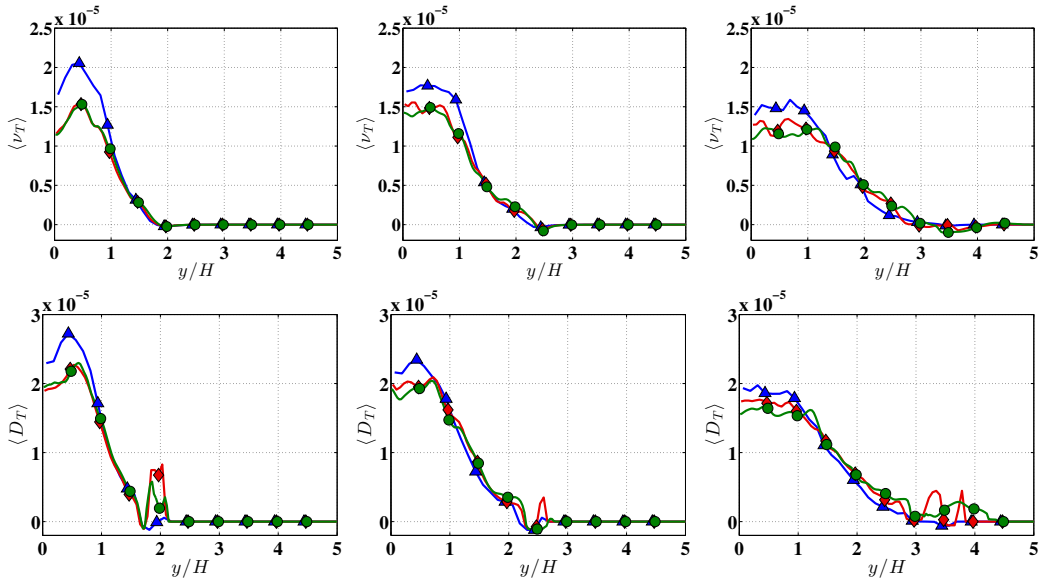

Figure 7.16: Average stream-normal profile of Smagorinsky viscosity (top) and dynamic diffusivity (bottom) at times corresponding to t^* of one, two and four (left to right) for FGR values of one (blue triangle), two (red diamond) and four (green circle).

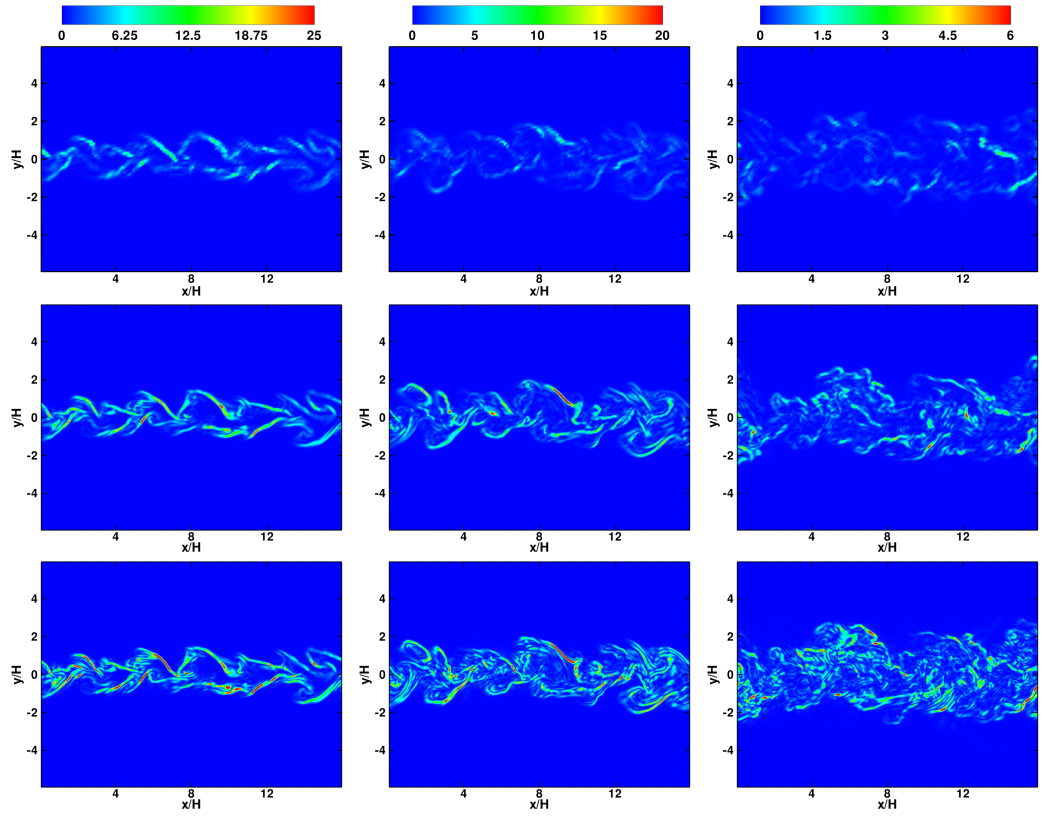

Figure 7.17: Instantaneous contours of filtered scalar dissipation rate using the algebraic model at times corresponding to t^*= 1, 2, 4 (left and right) for FGR= 1, 2, 4 of one, two and four (top to bottom).

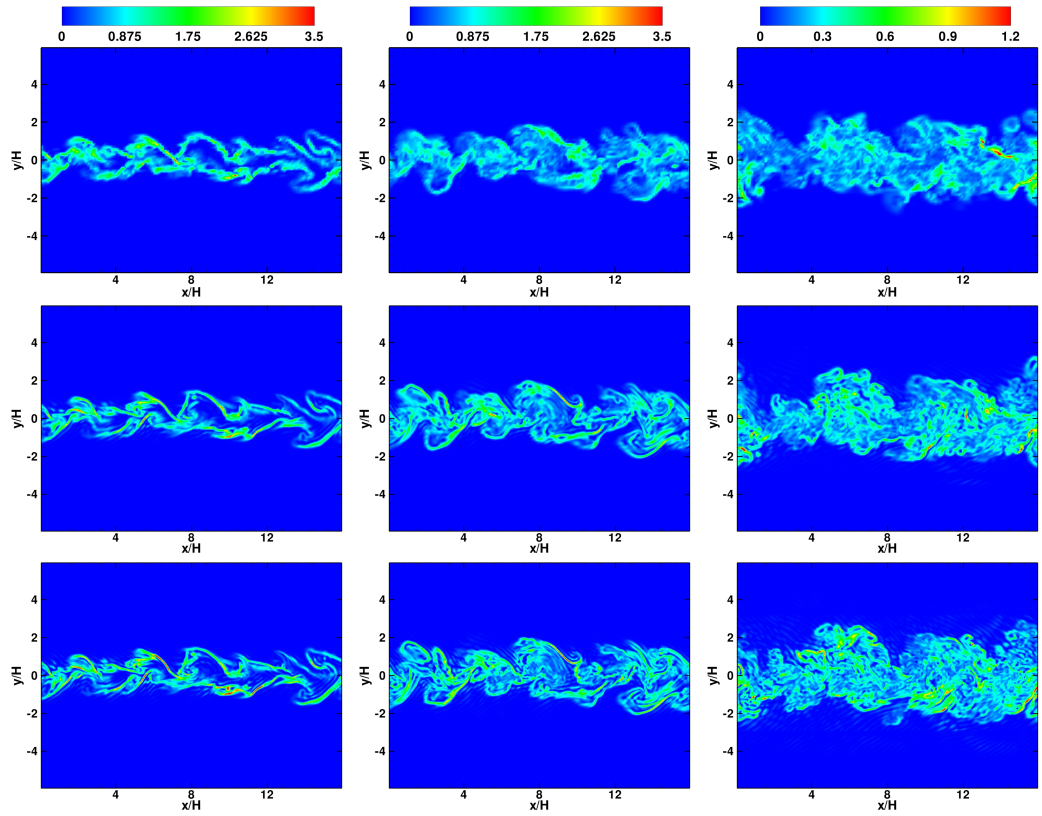

Figure 7.18: Instantaneous contours of filtered dissipation rate using the STE model at times corresponding to t^* of one, two and four (left and right) for FGRs of one, two and four (top to bottom).

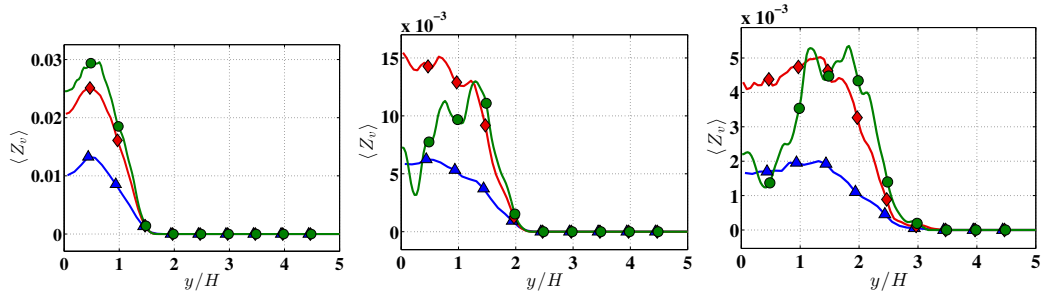

Figure 7.19: Average stream-normal profile of mixture fraction variance using the CDM at times corresponding to t^* of one, two and four (left to right) for FGR values of one (blue triangle), two (red diamond) and four (green circle).

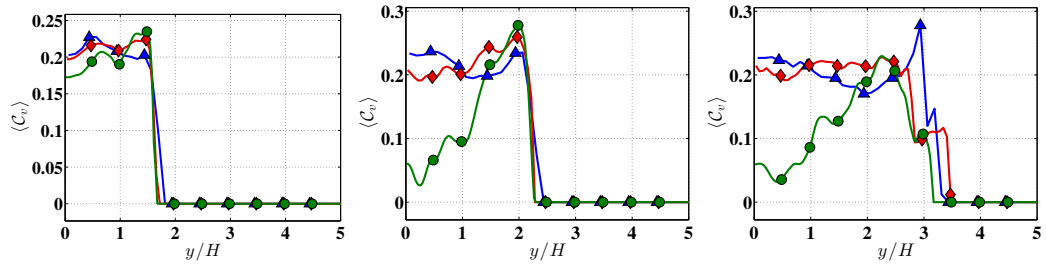

Figure 7.20: Average stream-normal profile of CDM coefficient at times corresponding to t^* of one, two and four (left to right) for FGR values of one (blue triangle), two (red diamond) and four (green circle).

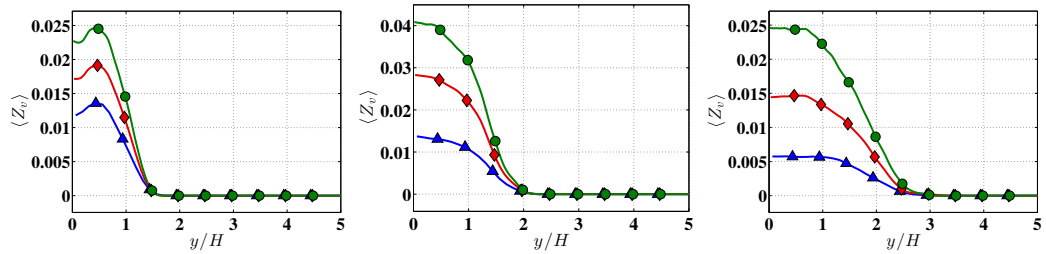

Figure 7.21: Average stream-normal profile of mixture fraction variance using the VTE model at times corresponding to t^* of one, two and four (left to right) for FGR values of one (blue triangle), two (red diamond) and four (green circle).

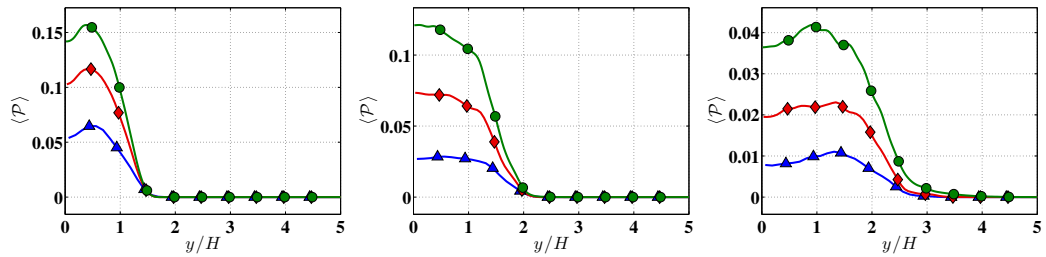

Figure 7.22: Average stream-normal profile of variance production for the VTE model at times corresponding to t^* of one, two and four (left to right) for FGR values of one (blue triangle), two (red diamond) and four (green circle).

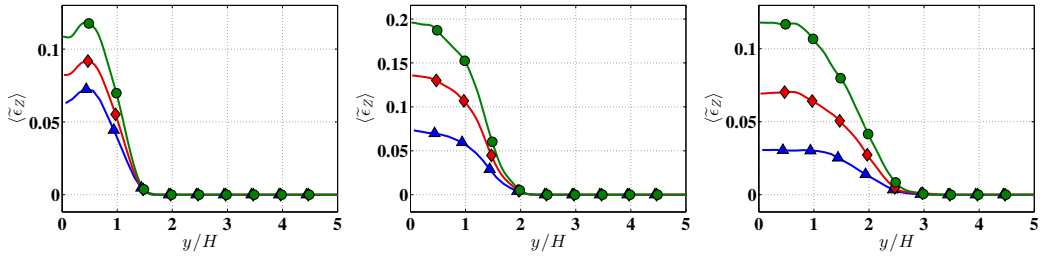

Figure 7.23: Average stream-normal profile of variance dissipation for the VTE model at times corresponding to t^* of one, two and four (left to right) for FGR values of one (blue triangle), two (red diamond) and four (green circle).

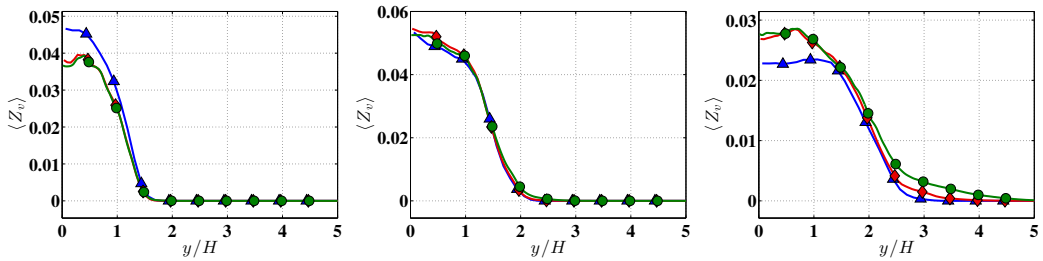

Figure 7.24: Average stream-normal profile of mixture fraction variance using the STE model at times corresponding to t^* of one, two and four (left to right) for FGR values of one (blue triangle), two (red diamond) and four (green circle).

Chapter 8

Conclusions and Future Direction

8.1 PDF Approach for Spray Combustion Studies

The coupling of evaporation, mixing and chemical reactions in spray-laden reacting flows requires a combustion model able to accommodate non-premixed, premixed and partially premixed modes. The transported PDF approach presents an ideal means to achieve this due to the appearance of a closed chemical source term. Previous efforts have been made to utilize this approach for single scalar values. In this work, a transport equation for the high-dimensional scalar joint-PDF was derived for use in an LES context. The numerical algorithms for a Lagrangian Monte-Carlo framework were developed in a manner consistent with conservation in a low-Mach number solver. Verification was conducted using a one-dimensional configuration to exhibit the consistency of the solver and evaluate the rates of convergence. In addition, experimental data shows that the PDF method evolves the time-averaged filtered fields accurately along with lower numerical diffusion compared to the LES-based scalar transport

Secondary analysis was performed using fully-resolved DNS of a spray-laden planar jet flame. This work provided the opportunity to study the range

of combustion regimes present in spray combustion along with an evaluation of model requirements and general performance in a high-fidelity setting. This formulation was shown to be more appropriate than a combustion model tailored to a given single phase combustion regime. The commonly used IEM model closure for the additional conditional micromixing term was shown to be accurate for gaseous flames but not adaptive enough to describe the complexities of spray evolution and reaction, especially in the presence of larger droplets. The LES/PDF method is shown to be signifcantly more accurate than LES filtered scalar transport equations in predicting time-averaged quantities of interest.

Experimental validation and further analysis were performed using two families of jet flames. First was a set of piloted ethanol spray flames. For these flames, the simplicity of the The experimental results were qualitatively reproduced by the LES/PDF approach. It was also found that the lack of sufficient information about the inflow conditions led to large discrepancies in the results. Similar to the experiment, the simulation predicted a long and narrow flame. This was the result of low velocity differences across the jet and the coflow leading to reduced shear-induced jet mixing. The conditional statistics demonstrated the presence of a stratified premixed zone on the rich side of the flame, while the lean-side exhibited a typical non-premixed flame structure.

The auto-igniting methanol spray flames from University of Sydney were studied using a conditional evaporation model based LES/PDF approach.

The simulations indicate that there are two different ignition modes in the spray flames, driven by either the coflow entrainment or the progressive mixing of the evaporated mass in the fuel jet with the carrier air. At the flame base, there is a sudden evaporation of droplets leading to substantial increase in methanol concentration which is subsequently consumed. It was shown that the pairwise interaction model used to couple the spray and PDF solvers captures both these ignition modes. Overall, the LES/PDF approach predicts the structure of the spray flames well, with good quantitative accuracy as compared to experimental data. It is also noticed that subfilter mixing does not alter the mean temperature profiles substantially but the subfilter distribution of the composition vector changes considerably. It is postulated that particles entrained from the coflow and with higher mass dominate the mean temperature calculation, but the variance indicates the presence of a small number of partially burning particles that originate in the main jet and have lower weights. This will explain the lack of temperature sensitivity but appreciable sensitivity of subfilter variance to mixing rates.

As an addendum, the following is an inclusion from experience with comparative analysis from RANS, LES, and LES/PDF approaches applied the Sydney piloted flames through participation in the Turbulent Combustion of Sprays Workshop [115]. The results of these studies provided information regarding general needs in spray combustion modeling beyond those observed from the LES/PDF simulations presented in this dissertation. The following information was gleaned from these comparisons.

- Three different combustion models, namely the flamelet, FPVA, and PDF methods, were considered. It was found that the use of the flamelet model provided the best gas phase temperature predictions near the centerline, which is a direct consequence of the assumptions built into the flamelet description. The fact that the FPVA and PDF methods require mixing of high-temperature fluid with the core of the jet to increase temperature leads us to conclude that the large scale mixing is still not correctly predicted by the simulations. This will in turn affect droplet evaporation and temperature evolution downstream. On the contrary, the higher temperature of the flamelet model causes very high droplet evaporation, which causes drastic underprediction of volume flux.

- The ideal specification of simulation inflow conditions for the Sydney piloted spray flame series remains uncertain. While it seems advantageous to simulate the entire pipe rather than use the exit conditions for specifying the flame inflow conditions, the results do not indicate any major improvement. In fact, by taking the droplet velocity properties directly from the gas phase seems to do as well as explicitly defining them from experimental measurements with regards to predicting the mean droplet properties. The velocity RMS seems to be more sensitive to the inflow conditions.

- The evaporation model is an important component of the modeling setup, but its effect cannot be discerned from this configuration directly.

The main issue is the validity of the evaporation models in the vicinity of the flame, and it is not clear if such a precise question could be answered from the essentially very high level configuration. Nevertheless, this question needs to be explored computationally, mainly through analyzing sensitivity to existing models as a way of interpreting the impact of evaporation models on the results.

- There has been a general bias in the literature with regard to LES vs. RANS modeling approaches, favoring the former due to its ability to represent large scale mixing. There is evidence of this advantage in previous results, however, if one would take into account the cost of the simulations, the LES approach does not seem to deliver vastly improved results that would warrant the unsteady three-dimensional computations. In this sense, significant work must be done for LES modelers to demonstrating the validity of this approach for such complex flow problems.

8.2 Explicit Filtering Studies

In this work, the explicit filtering technique was used to separate the LES filter width from the computational grid. A discrete filter with properties similar to a spectral-cutoff filter was implemented for a range of filter-to-grid ratios (FGRs), with larger FGR values corresponding to higher grid density. Two different configurations, the HIT and the temporal shear layer, were simulated. The explicit filtering operation was found to be effective at removing energy at scales smaller than the prescribed filter size. However, due to the

truncation of the spectral-like filter in physical space, the transfer function exhibits oscillations at large wave numbers. These imperfections did not have a significant impact for the range of the FGRs and filter sizes tested here, but could be of an issue in variable density flows where local fluctuations could lead to numerical instability. An increase in FGR also increases the computational cost of the filtering operation, since the filter stencil increases with grid refinement.

Overall, it was found that numerical errors have significant effect on model performance and could drastically impact simulation of combusting flows. In both flow configurations studied here, large-scale dominated quantities such as the average kinetic energy or scalar energy remain unaffected by numerical errors. In this sense, errors at the small scales did not propagate to larger scales to contaminate the entire solution. Nevertheless, small-scale quantities such as variance and dissipation rate are strongly affected by numerical errors. In variable density reacting flows, such errors at the small scales will alter heat release and may affect the large scale evolution as well.

Given that numerical errors are important in the LES, and are bound to be even more critical in reacting flows due to the dependence on small-scale models, it is important to reduce numerical errors. There are two strategies for minimizing this effect. The simplest option appears to be the construction of models and model formulations that do not depend on gradient-based source terms. The STE model is remarkably resilient to small-scale errors principally due to the fact that it does not contain the gradient-squared source term that

appears in the VTE equation. It has been found that the use of such moment equations lead to robust behavior in supersonic flows as well [55]. In many situations of interest in combustion modeling, including soot transport and conserved-scalar based turbulence-chemistry interaction, it is possible to cast the equations in this low-error form thereby reducing the impact of discretization. However, this is not a general solution and vastly limits the range of models to be used.

The other option is to explore the link between filter width and mesh size, and formulate LES to account for the errors. The explicit filtering approach described here is one such technique, whereby a clear separation of the grid and filter level scales could be made. Clearly, the results presented here for the turbulent mixing cases demonstrated the impact of numerical errors. However, the method is inherently expensive, and the spatial truncation of the spectral-like filter leads to inefficiencies that may not be numerically stable for large-density variation cases. An emerging line of thinking is the notion that concept of filtering has to be revisited. Based on the work of Adrian [116, 117], LES could be thought of as solving a high-Reynolds number flow on a computational grid that is inadequate to support all the scales. In this sense, it is possible to recast the LES equations in the form of a statistical closure problem. Moser and co-workers [118, 119, 120] have extended this view and considered numerical discretization an inherent part of solving the filtered equations. Recently, Pope [121] developed a related but different approach that presents the LES problem is terms of modeling certain conditional

averages.

The methods discussed above has so far been used only in simple flows and there is considerable effort needed to make them mainstream approaches for solving practical flow configurations. Nevertheless, the results presented in this work should at the least provide caution when drawing conclusions from grid-filtered LES.

8.3 Future Direction

8.3.1 Dynamic Conditional Diffusion Modeling

One of the recognized challenges of transported PDF modeling is the unclosed conditional diffusion term. For the majority of PDF studies [21, 122, 123, 124], simplistic models like IEM are utilized and have been shown to be successful for gas phase flames. More advanced modeling approaches have been formulated, such as EMST [125] and modified Curl [126], but due to the additional computational expense, these are not desirable. With this in mind, it is advantageous to improve the accuracy of IEM in order to maintain relative computational efficiency.

As shown in Sect. 3.3.1, mixing in spray laden flows is still well-described by a linear relaxation from the mean. However, it was also shown that a single model coefficient is invalid due to the sparse evaporation source terms. This induces varying mixing intensities and structures. With the strong dependence of even low order moments on the mixing rate, a properly formulated dynamic model is crucial to further advancements in transported PDF methods.

8.3.2 Spray Flame Validation and Configuration Improvements

The comparative study mentioned above has also led to some intuition on the type of data that would be able to shed light on the modeling challenges still relevant to spray combustion.

- The single biggest difference between gas phase and spray flames is the nature of the boundary conditions, due to the challenges associated with generating well-characterized spray populations. Toward improving inflow condition specifications, it would be useful if detailed measurement of the fuel concentration profile as well as droplet evolution inside the development pipe is made available. In order to direct experimental investigations, a thorough numerical sensitivity study to the inflow parameters would also be beneficial. This would highlight parameters which should be the focus for improving droplet inflow specifications. It is clear that in spite of the length of the pipe, the inertia of the droplets continues to play some role in their spatial distribution. In addition, fuel evaporation inside the pipe may not lead to homogeneous mixtures at the nozzle exit, which could severely alter the development of the flame front. Non-uniform droplet distribution will also impact the propagation of the flame in the near-entrance region.

- Given the flow complexity, it would be useful to identity and develop lower-level experiments that only couple a few of the physical phenomena will be useful in building confidence in the predictions. For instance,

the aforementioned pipe information only couples droplet flow to evaporation without the interaction of the turbulent flow. Use of direct numerical simulation (DNS) or such sources of data will help isolate modeling problems.

- In comparing with experiments, it is important that the model is tested on multiple flames in the configuration rather than one. Due to the complexity of the problem, evaluating the sensitivity of the models to flow conditions rather than focusing on the quantitative prediction of a single flame condition is more illuminating.

8.3.3 Explicit Filtering for Variable Density Flows

In this work, explicit filtering has been applied to constant density gas phase mixing in canonical configurations. Overcoming each of these restrictions requires further research.

The first challenge was exemplified in the presence of free shear mixing, where the lack of a sharp spectral filter allows progressive generation of small scales. The spurious energy seen in the contour plots of dissipation rate is not detrimental in these configurations, while the strong non-linearities involved in either the mapping of tabulated chemistry or even direct integration will result in possibly catastrophic fluctuations in temperature and density. One possible solution is the application of an additional dissipative term to remove high frequency energy from a quantity of interest. This dissipative approach has been used in compressible flows, and has been termed hyper viscosity [127]. In

essence, this viscosity (or diffusivity in the case of scalar transport) is proportional to high order derivatives of the field of interest and in itself is isolated to high frequency content. The challenges in applying this approach to explicit filtering are two-fold. One is the nature of pressure correction in low-Mach number flows, which tends to diffuse high frequency content, possibly negating the ability to isolate the desired dissipation and instead laminarizing the entire field of interest. Secondly, previous implementation of this approach was to dissipate energy at the grid scale, thus allowing simple grid-based scaling. In explicit filtering, the length scale at which energy needs to be removed changes with FGR, making a universal length scale and model coefficient difficult to characterize.

The second step to applying explicit filtering to more practical applications is the need for boundary condition specification. The challenge is to provide a boundary condition free of sub filter scales while remaining accurate with respect to the sharp interfaces between inflows (i.e. jet and coflow). Previous efforts have been made to address this issue, involving grid-based LES in the near field to allow shear layers to sufficiently diffuse as to remove sub filter scales. This was shown to be relatively successful, though application is limited to uni-directional flows. As shown by Kaul and Raman [35], early mixing times are also when the largest numerical errors are present due to significant high-frequency content. This implies the need for explicit filtering throughout the flow evolution.

Appendices

Appendix A

PDF Transport Equation

The use of a transport equation for the joint-PDF of the thermochemical composition is vital to PDF methods. This appendix provides a derivation of the composition-sensible enthalpy joint-PDF transport equation from first principles.

Based on the definition of the PDF in Eq. 2.30, filtered values of any field of interest $Q(\boldsymbol{\phi})$ can be written

$$\widetilde{Q(\boldsymbol{\phi})} = \frac{1}{\overline{\rho}} \int Q(\boldsymbol{\psi}) P d\boldsymbol{\psi} \tag{A.1}$$

where $\boldsymbol{\psi}$ represents the sample space variable corresponding to the composition vector $\boldsymbol{\phi}$ and $\overline{\rho}$ is the filtered value of density. In a similar fashion, the filtered non-linear convective term can be written as

$$\begin{aligned} \widetilde{\boldsymbol{u}Q(\boldsymbol{\phi})} =& \frac{1}{\overline{\rho}} \int B(\boldsymbol{\psi}) \boldsymbol{v} f_{\boldsymbol{v},\boldsymbol{\psi}} d\boldsymbol{v} d\boldsymbol{\psi} \\ & \frac{1}{\overline{\rho}} \int B(\boldsymbol{\psi}) \widetilde{\boldsymbol{u}|\boldsymbol{\psi}} P d\boldsymbol{\psi} \end{aligned} \tag{A.2}$$

where $\boldsymbol{v}$ is the sample space variable representing the velocity field $\boldsymbol{u}$, $f_{\boldsymbol{v},\boldsymbol{\psi}}$ is the joint PDF of velocity and composition. Going forward, additional useful identities are

$$\overline{\rho}\widetilde{\boldsymbol{u}|\boldsymbol{\psi}} = \int \boldsymbol{v} f_{\boldsymbol{v},\boldsymbol{\psi}} d\boldsymbol{v} d\boldsymbol{\psi} \tag{A.3}$$

$$\overline{\rho} f_{\boldsymbol{v},\boldsymbol{\psi}} = P f_{\boldsymbol{v}|\boldsymbol{\psi}} \tag{A.4}$$

Using this framework, the filtered transport equation for $Q(\boldsymbol{\phi})$ can be formulated as

$$\frac{\partial \overline{\rho}\widetilde{Q(\boldsymbol{\phi})}}{\partial t} + \frac{\partial \overline{\rho} u_i \widetilde{Q(\boldsymbol{\phi})}}{\partial x_i} = \int Q(\boldsymbol{\psi}) \left(\frac{\partial F}{\partial t} + \frac{\partial \widetilde{u_i|\boldsymbol{\psi}} P}{\partial x_i} \right). \tag{A.5}$$

The constraint of continuity allows the use of the chain rule to obtain

$$\begin{aligned} \frac{D\widetilde{Q(\boldsymbol{\phi})}}{Dt} &= \frac{\partial \widetilde{Q(\boldsymbol{\phi})}}{\partial \boldsymbol{\phi}} \frac{D\boldsymbol{\phi}}{Dt} \\ &= \frac{\partial \widetilde{Q(\boldsymbol{\phi})}}{\partial \boldsymbol{\phi}} A(\boldsymbol{\phi}, \boldsymbol{x}) \end{aligned} \tag{A.6}$$

where $A(\boldsymbol{\phi}, \boldsymbol{x})$ represents all right hand side terms in Eq. 2.4 and 2.6 and $\boldsymbol{x}$ is the spatial coordinate. Expanding this expression results in

$$\begin{aligned} \frac{D\widetilde{Q(\boldsymbol{\phi})}}{Dt} &= \frac{1}{\overline{\rho}} \int \frac{\partial Q(\boldsymbol{\psi})}{\partial \boldsymbol{\psi}} A(\boldsymbol{\psi}, \boldsymbol{x}) f_{\boldsymbol{\psi},\boldsymbol{y}} d\boldsymbol{\psi} d\boldsymbol{y} \\ &= \frac{1}{\overline{\rho}} \int Q(\boldsymbol{\psi}) \frac{\partial}{\partial \boldsymbol{\psi}} \widetilde{A|\boldsymbol{\psi}} d\boldsymbol{\psi} \end{aligned} \tag{A.7}$$

Here, $\boldsymbol{y}$ is the sample space variable representing $\boldsymbol{x}$ and $f_{\boldsymbol{\psi},\boldsymbol{y}}$ is the multi-point joint PDF of $\boldsymbol{\psi}$. From this point, Eq. 2.32 can be combined to obtain the final result shown in Eq. 2.32.

To simulate round jet flames, it is advantageous to use the PDF transport equations posed in the cylindrical coordinate system. Here, we provide the formulation developed by [128] for the cylindrical-coordinate PDF transport equation. Note that transport in composition space is not affected by the transformation. The transport equation for rF_L [128], where F_L is the

mass-weighted PDF, is as follows:

$$\frac{\partial r F_L}{\partial t} + \frac{\partial}{\partial r}\left[\left(A_r + \frac{B}{r}\right) r F_L\right] + \frac{\partial}{\partial \theta}\left(\frac{A_\theta}{r} r F_L\right) + \frac{\partial}{\partial z}\left(A_z r F_L\right) + \frac{\partial^2}{\partial r^2}\left(B\, r F_L\right) + \frac{\partial^2}{\partial \theta^2}\left(\frac{B}{r^2} r F_L\right) + \frac{\partial^2}{\partial z^2}\left(B\, r F_L\right) = -\frac{\partial}{\partial \psi_i}\left[\left(\widetilde{\mathcal{M}_i|\boldsymbol{\psi}} + S_i\left(\boldsymbol{\psi}\right)\right) r F_L\right], \tag{A.8}$$

where $B = D_T$. A_r, A_θ, and A_z are given by

$$A_r = \widetilde{u}_r + \frac{1}{\overline{\rho}}\frac{\partial}{\partial r}\left(\overline{\rho} B\right) \tag{A.9}$$

$$A_\theta = \widetilde{u}_\theta + \frac{1}{r\overline{\rho}}\frac{\partial}{\partial \theta}\left(\overline{\rho} B\right) \tag{A.10}$$

$$A_z = \widetilde{u}_z + \frac{1}{\overline{\rho}}\frac{\partial}{\partial z}\left(\overline{\rho} B\right). \tag{A.11}$$

Appendix B

Filtered Moment Transport Equations

The transport equation for any scalar ϕ_α in a N-species spray-combustion system is written as

$$\frac{\partial \rho \phi_\alpha}{\partial t} + \frac{\rho u_i \phi_\alpha}{\partial x_i} = \frac{\partial}{\partial x_i}\left(\rho D \frac{\partial \phi_\alpha}{\partial x_i}\right) + \dot{\omega}_\alpha + \dot{S}_\alpha, \tag{B.1}$$

where the velocities and the scalar mass fractions represent unfiltered quantities corresponding to the microscopic transport equation. In relation to the scalar transport equation presented in the text (Eq. 2.4), the evaporation source-term has been rewritten such that $\dot{S}_\alpha = \phi_\alpha^f \dot{S}^m$, where ϕ_α^f is the mass fraction for each species in a fuel droplet. ω_α denotes the chemical source term. The equation for n-th moment of the scalar (also termed as a pure moment) is obtained by multiplying the above equation by ϕ_α^{n-1} and using continuity equation (Eq. 2.8).

$$\begin{aligned}\frac{\partial \rho \phi_\alpha^n}{\partial t} + \frac{\partial \rho u_i \phi_\alpha^n}{\partial x_i} &= \frac{\partial}{\partial x_i}\left(\rho D \frac{\partial \phi_\alpha^n}{\partial x_i}\right) ... \\ &... + n\phi_\alpha^{n-1}\dot{\omega}_\alpha - n\rho D \frac{\partial \phi_\alpha}{\partial x_i}\frac{\partial \phi_\alpha^{n-1}}{\partial x_i} + n\phi_\alpha^{n-1}\dot{S}_\alpha - (n-1)\phi_\alpha^n \dot{S}_\alpha.\end{aligned} \tag{B.2}$$

It can be easily verified that when $n = 2$, and in the absence of spray source term, the above equation reduces to the second moment transport equation

[35]. For $n \geq 2$, the dissipation-like term in the above equation can be re-written as follows:

$$n\rho D\frac{\partial\phi_\alpha}{\partial x_i}\frac{\partial\phi_\alpha^{n-1}}{\partial x_i} = n(n-1)\phi_\alpha^{n-2}\rho D\frac{\partial\phi_\alpha}{\partial x_i}\frac{\partial\phi_\alpha}{\partial x_i}, \tag{B.3}$$

where the term on the right hand side is similar to the moment of the scalar multiplied by dissipation rate of scalar.

The filtered-form of the pure-moment equation is obtained by applying the filtering operation (Eq: 6.1) to Eq. B.2.

$$\begin{aligned}\frac{\partial\overline{\rho}\widetilde{\phi_\alpha^n}}{\partial t} + \frac{\partial\overline{\rho}\widetilde{u}_i\widetilde{\phi_\alpha^n}}{\partial x_i} &= \frac{\partial}{\partial x_i}\left(\overline{\rho}(D+D_t)\frac{\partial\widetilde{\phi_\alpha^n}}{\partial x_i}\right) ... \\ &... + n\widetilde{\phi_\alpha^{n-1}\dot{\omega}_\alpha} - \frac{n(n-1)}{2}\overline{\rho}\widetilde{\phi_\alpha^{n-2}\chi_{ii}} + n\widetilde{\phi_\alpha^{n-1}\dot{S}_\alpha} - (n-1)\widetilde{\phi_\alpha^n\dot{S}_\alpha},\end{aligned} \tag{B.4}$$

where $\chi_{ij} = 2D\frac{\partial\phi_\alpha}{\partial x_i}\frac{\partial\phi_\beta}{\partial x_j}$.

The cross-moments, $\widetilde{\phi_\alpha^n\phi_\beta^m}$ can be obtained by first summing the product of ϕ_α^n transport equation with ϕ_β^m and the product of ϕ_β^m transport equation with ϕ_α^n. Filtering the resulting equation leads to

$$\begin{aligned}\frac{\partial\overline{\rho}\widetilde{\phi_\alpha^n\phi_\beta^m}}{\partial t} + \frac{\partial\overline{\rho}\widetilde{u}_i\widetilde{\phi_\alpha^n\phi_\beta^m}}{\partial x_i} &= \frac{\partial}{\partial x_i}\left(\overline{\rho}(D+D_t)\frac{\partial\widetilde{\phi_\alpha^n\phi_\beta^m}}{\partial x_i}\right) ... \\ &... + \left(n\widetilde{\phi_\beta^m\phi_\alpha^{n-1}\dot{\omega}_\alpha} + m\widetilde{\phi_\alpha^n\phi_\beta^{m-1}\dot{\omega}_\beta}\right) - \frac{n(n-1)}{2}\overline{\rho}\widetilde{\phi_\beta^m\phi_\alpha^{n-2}\chi_{ii}} ... \\ &... - \frac{m(m-1)}{2}\overline{\rho}\widetilde{\phi_\alpha^n\phi_\beta^{m-2}\chi_{jj}} - nm\overline{\rho}\widetilde{\phi_\alpha^{n-1}\phi_\beta^{m-1}\chi_{ij}} ... \\ &... + \phi_\beta^m\left(n\phi_\alpha^{n-1} - (n-1)\phi_\alpha^n\right)\dot{S}_\alpha ... \\ &... + \phi_\alpha^n\left(m\phi_\beta^{m-1} - (m-1)\phi_\beta^m\right)\dot{S}_\beta,\end{aligned} \tag{B.5}$$

where only k is a repeated index. In the above equation, for $n < 2, m < 2$, the third and fourth terms on the right hand side involving χ disappear.

The above moment transport equations could be derived starting by multiplying the PDF transport equation (Eq. 2.32) by $\psi_\alpha^n \psi_\beta^m$ and integrating over the composition space. In order to simplify the resulting multi-dimensional integration, the following relations need to be used:

$$\int_{-\infty}^{\infty} \psi^n \frac{\partial}{\partial \psi} \left(\widetilde{Q|\psi} P \right) d\psi = -n \int \psi^{n-1} \widetilde{Q|\psi} P d\psi = -n \widetilde{\phi^{n-1} Q}, \tag{B.6}$$

where Q is any quantity.

$$\int_{-\infty}^{\infty} \psi_\alpha^n \psi_\beta^m \frac{\partial^2}{\partial \psi_\alpha^2} \left(\widetilde{\chi_{ii}|\boldsymbol{\psi}} P \right) = n(n-1) \phi_\alpha^{n-1} \widetilde{\phi_\beta^m} \chi_{ii} \tag{B.7}$$

The energy transport equation has a slightly different form due to the nature of the source terms. By multiplying the PDF equation by e and e^2, the following transport equation for energy moments can be obtained.

$$\frac{\partial \overline{\rho} \widetilde{h}}{\partial t} + \frac{\partial \overline{\rho} \widetilde{u}_j \widetilde{h}}{\partial x_j} = \frac{\partial}{\partial x_j} \left(\overline{\rho} \left(D + D_T \right) \frac{\partial \widetilde{h}}{\partial x_j} \right) + \widetilde{\omega}_h + \widetilde{\dot{S}^h}, \tag{B.8}$$

which is given in Eq. 2.6 and

$$\frac{\partial \overline{\rho} \widetilde{\phi_h^2}}{\partial t} + \frac{\partial \overline{\rho} \widetilde{u}_j \widetilde{\phi_h^2}}{\partial x_j} = \frac{\partial}{\partial x_j} \left(\overline{\rho} \left(D + D_T \right) \frac{\partial \widetilde{\phi_h^2}}{\partial x_j} \right) + \widetilde{\phi_h \omega_h} - \chi_{hh} + 2 \widetilde{\phi_h \dot{S}^h} - \widetilde{h^2 \dot{S}^m}, \tag{B.9}$$

Appendix C

Discrete filter coefficients

The symmetric fourth order commutation filter coefficients for each filter-to-grid ratio are provided below. For a FGR of one, the stencil is a single value $w_0 = 1.0$.

For a FGR of two, the coefficients are

$w_0 = 0.4982139, \quad w_{\pm1} = 0.2823359, \quad w_{\pm2} = -1.298893 \times 10^{-4},$

$w_{\pm3} = -0.03131293$

For a FGR of four, the coefficients are

$w_0 = 0.2470827, \quad w_{\pm1} = 0.2171517, \quad w_{\pm2} = 0.1426843, \quad w_{\pm3} = 0.05928336,$

$w_{\pm4} = -1.251308 \times 10^{-5}, \quad w_{\pm5} = -0.02257883, \quad w_{\pm6} = -0.01743326,$

$w_{\pm7} = -2.636139 \times 10^{-3}$

For a FGR of eight, the coefficients are

$w_0 = 0.1251459, \quad w_{\pm1} = 0.1210064, \quad w_{\pm2} = 0.1092010, \quad w_{\pm3} = 0.09144446,$

$w_{\pm4} = 0.07021041, \quad w_{\pm5} = 0.04825201, \quad w_{\pm6} = 0.02809933, \quad w_{\pm7} = 0.01164511,$

$w_{\pm8} = -9.772352 \times 10^{-5}, \quad w_{\pm9} = -7.031323 \times 10^{-3},$

$w_{\pm10} = -9.818915 \times 10^{-3}, \quad w_{\pm11} = -9.602602 \times 10^{-3},$

$w_{\pm12} = -7.676925 \times 10^{-3}, \quad w_{\pm13} = -5.200319 \times 10^{-3},$

$w_{\pm14} = -3.003746 \times 10^{-3}$

For a FGR of 16, the coefficients are

$w_0 = 0.0621322, \quad w_{\pm1} = 0.0616324, \quad w_{\pm2} = 0.0601511, \quad w_{\pm3} = 0.0577403,$

$w_{\pm4} = 0.0544844, \quad w_{\pm5} = 0.0504957, \quad w_{\pm6} = 0.0459093, \quad w_{\pm7} = 0.0408765,$

$w_{\pm8} = 0.0355584, \quad w_{\pm9} = 0.301185, w_{\pm10} = 0.0247155, \quad w_{\pm11} = 0.0194971,$

$w_{\pm12} = 0.0145939, \quad w_{\pm13} = 0.0101155, \quad w_{\pm14} = 6.14674 \times 10^{-3},$

$w_{\pm15} = 2.74574 \times 10^{-3}, \quad w_{\pm16} = -5.62051 \times 10^{-5}, \quad w_{\pm17} = -2.25387 \times 10^{-3},$

$w_{\pm18} = -3.86594 \times 10^{-3}, \quad w_{\pm19} = -4.93181 \times 10^{-3}, \quad w_{\pm20} = -5.50762 \times 10^{-3},$

$w_{\pm21} = -5.56618 \times 10^{-3}, \quad w_{\pm22} = -5.47049 \times 10^{-3}, \quad w_{\pm23} = -5.01273 \times 10^{-3},$

$w_{\pm24} = -4.36648 \times 10^{-3}, \quad w_{\pm25} = -3.60469 \times 10^{-3}, \quad w_{\pm26} = -2.79242 \times 10^{-3},$

$w_{\pm27} = -1.98455 \times 10^{-3}, \quad w_{\pm28} = -1.22450 \times 10^{-3}, \quad w_{\pm29} = -5.43698 \times 10^{-4}$

Bibliography

[1] A. N. Kolmogorov. A refinement of previous hypotheses concerning the local structure of turbulence in viscous incompressible fluid for high Reynolds numbers. *Journal of Fluid Mechanics*, 13:82–85, 1962.

[2] T. Poinsot and D. Veynante. *Theoretical and Numerical Combustion*. R. T. Edwards, Philadelphia, USA, 2001.

[3] N. Peters. Laminar diffusion flamelet models in non-premixed turbulent combustion. *Progress in Energy and Combustion Science*, 10:319–339, 1984.

[4] Norbert Peters. *Turbulent Combustion*. Cambridge University Press, 2000.

[5] J. Jimenez, A. Linan, M. M. Rogers, and F. J. Higuera. *A Priori* testing of subgrid models for chemically reacting non-premixed turbulent flows. *Journal of Fluid Mechanics*, 349:149–171, 1997.

[6] A. W. Cook, J. J. Riley, and G. Kosály. A laminar flamelet approach to subgrid-scale chemistry in turbulent flows. *Combustion and Flame*, 109:332–341, 1997.

[7] A. Kempf, R. P. Lindstedt, and J. Janicka. Large-eddy simulation of bluff-body stabilized nonpremixed flame. *Combustion and Flame*, 144(1-2):170–189, 2006.

[8] H. Pitsch and N. Peters. A consistent flamelet formulation for non-premixed combustion considering differential diffusion effects. *Combustion and Flame*, 144:26–40, 1998.

[9] H. Pitsch. Unsteady flamelet modeling of differential diffusion in turbulent jet diffusion flames. *Combustion and Flame*, 123:358–374, 2000.

[10] P. E. Desjardin and S. H. Frankel. Large eddy simulation of a non-premixed reacting jet: Application and assessment of subgrid-scale combustion models. *Physics of Fluids*, 10:2298–2314, 1998.

[11] GM Goldin and S Menon. A comparison of scalar pdf turbulent combustion models. *Combustion and Flame*, 113(3):442–453, MAY 1998.

[12] M. R. Sheikhi, T. G. Drozda, P. Givi, and S. B. Pope. Velocity-scalar filtered density function for large eddu simulation of turbulent flows. *Physics of Fluids*, 15(8):2321–2337, 2003.

[13] F. A. Jaberi, P. J. Colucci, S. James, P. Givi, and S. B. Pope. Filtered mass density function for large-eddy simulation of turbulent reacting flows. *Journal of Fluid Mechanics*, 401:85–121, 1999.

[14] P. J. Colucci, F. A. Jaberi, and P. Givi. Filtered density function for large eddy simulation of turbulent reacting flows. *Physics of Fluids*, 10(2):499–515, 1998.

[15] S. B. Pope. A monte-carlo method for the pdf equations of turbulent reactive flow. *Combustion Science and Technology*, 25:159–174, 1981.

[16] H Mobus, P Gerlinger, and D Bruggemann. Scalar and joint scalar-velocity-frequency monte carlo pdf simulation of supersonic combustion. *Combustion and Flame*, 132:3–24, 2003.

[17] Feng Gao and Edward E. O'Brien. A large-eddy simulation scheme for turbulent reacting flows. *Physics of Fluids*, 5(6):1282, 1993.

[18] K. Luo, H. Pitsch, M. G. Pai, and O. Desjardins. Direct numerical simulations and analysis of three-dimensional n-heptane spray flames in a model swirl combustor. *Proceedings of the Combustion Institute*, 33(Part 2):2143–2152, 2011.

[19] J. Reveillon and L. Vervisch. Analysis of weakly turbulent dilute-spray flames and spray combustion regimes. *Journal of Fluid Mechanics*, 537:317–347, 2005.

[20] H. Pitsch. Large-eddy simulation of turbulent combustion. *Annual Review of Fluid Mechanics*, 38:453–482, 2006.

[21] V. Raman, H. Pitsch, and R. O. Fox. A consistent hybrid LES-FDF scheme for the simulation of turbulent reactive flows. *Combustion and Flame*, 143(1-2):56–78, 2005.

[22] W. K. Bushe and H. Steiner. Conditional moment closure for large eddy simulation of non-premixed turbulent reacting flows. *Physics of Fluids*, 11:1896–1906, 1999.

[23] Antonios Triantafyllidis and Epaminondas Mastorakos. Implementation Issues of the Conditional Moment Closure Model in Large Eddy Simulations. *Flow Turbulence and Combustion*, 84(3, SI):481–512, APR 2010. Conference on DNS and LES of Reactive Flows, Maastricht, Netherlands, Oct, 2008.

[24] H. W. Ge, I. Duewel, H. Kronemayer, R. W. Dibble, E. Gutheil, C. Schulz, and J. Wolfrum. Laser-based experimental and Monte Carlo PDF numerical investigation of an ethanol/air spray flame. *Combustion Science and Technology*, 180(8):1529–1547, 2008.

[25] Hai-Wen Ge and Eva Gutheil. Simulation of a turbulent spray flame using coupled PDF gas phase and spray flamelet modeling. *Combustion and Flame*, 153(1-2):173–185, APR 2008.

[26] C. D. Pierce and P. Moin. Progress-variable approach for large-eddy simulation of non-premixed turbulent combustion. *Journal of Fluid Mechanics*, 504:73–97, 2004.

[27] H. Pitsch and H. Steiner. Large-eddy simulation of a turbulent piloted methane/air diffusion flame (Sandia flame D). *Physics of Fluids*, 12(10):2541–2554, 2000.

[28] P Givi. Filtered density function for subgrid scale modeling of turbulent combustion. *AIAA Journal*, 44(1):16–23, JAN 2006.

[29] V. Raman and H. Pitsch. A consistent LES/filtered-density function formulation for the simulation of turbulent flames with detailed chemistry. *Proceedings Proceedings of the Combustion Institute*, 31:1711–1719, 2006.

[30] W. P. Jones, S. Lyra, and S. Navarro-Martinez. Large Eddy Simulation of a swirl stabilized spray flame. *Proceedings of the Combustion Institute*, 33(Part 2):2153–2160, 2011.

[31] F. X. Demoulin and R. Borghi. Modeling of turbulent spray combustion with application to diesel like experiment. *Combustion and Flame*, 129:281–293, 2000.

[32] Mikael Mortensen and Robert W. Bilger. Derivation of the conditional moment closure equations for spray combustion. *Combustion and Flame*, 156(1):62–72, JAN 2009.

[33] WP Jones and DH Sheen. A probability density function method for modelling liquid fuel sprays. *Flow Turbulence and Combustion*, 63(1-4):379–394, 2000.

[34] C. M. Kaul, V. Raman, G. Balarac, and H. Pitsch. Numerical errors in the computation of subfilter scalar variance in large eddy simulations. *Physics of Fluids*, 21(5), MAY 2009.

[35] C. M. Kaul and V. Raman. A posteriori analysis of numerical errors in subfilter scalar variance modeling for large eddy simulation. *Physics of Fluids*, 23(3), MAR 2011.

[36] D Carati, GS Winckelmans, and H Jeanmart. On the modelling of the subgrid-scale and filtered-scale stress tensors in large-eddy simulation. *Journal of Fluid Mechanics*, 441:119–138, AUG 25 2001.

[37] O.V. Vasilyev, T.S. Lund, and P. Moin. A general class of commutative filters for les in complex geometries. *Journal of Computational Physics*, 146(1):82–104, October 1998.

[38] TS Lund. The use of explicit filters in large eddy simulation. *Computers & Mathematics with Applications*, 46(4):603–616, AUG 2003.

[39] J Gullbrand and FK Chow. The effect of numerical errors and turbulence models in large-eddy simulations of channel flow, with and without explicit filtering. *Journal of Fluid Mechanics*, 495:323–341, NOV 25 2003.

[40] S.T. Bose, P. Moin, and D. You. Grid-independent large-eddy simulation using explicit filtering. *Physics of Fluids*, 22(10), OCT 2010.

[41] Tellervo T. Brandt. Usability of explicit filtering in large eddy simulation with a low-order numerical scheme and different subgrid-scale models. *International Journal of Numerical Methods in Fluids*, 57(7):905–928, JUL 10 2008.

[42] L. Goodfriend, F. K. Chow, M. Vanella, and E. Balaras. Large-eddy simulation of decaying isotropic turbulence across a grid refinement interface using explicit filtering and reconstruction. *Journal of Turbulence*, 14(12):58–76, DEC 1 2013.

[43] Senthilkumaran Radhakrishnan and Josette Bellan. Explicit filtering to obtain grid-spacing-independent and discretization-order-independent large-eddy simulation of compressible single-phase flow. *Journal of Fluid Mechanics*, 697:399–435, APR 25 2012.

[44] Colleen M. Kaul, Venkat Raman, Edward Knudsen, Edward S. Richardson, and Jacqueline H. Chen. Large eddy simulation of a lifted ethylene flame using a dynamic nonequilibrium model for subfilter scalar variance and dissipation rate. *Proceedings of the Combustion Institute*, 34(1):1289–1297, 2013.

[45] S. Menon and N.Patel. Subgrid modeling for simulation of spray combustion in large-scale combustors. *AIAA Journal*, 44(4):709–723, 2006.

[46] J. K. Dukowicz. A particle-fluid numerical model for liquid sprays. *Journal of Computational Physics*, 35:229–253, 1980.

[47] N. Okongo and J. Bellan. Consistent large-eddy simulation of a temporal mixing layer laden with evaporating drops. part1. direct numerical simulation, formulation and a priori analysis. *Journal of Fluid Mechanics*, 499:1–47, 2004.

[48] A. Leboissetier, N. Okongo, and J. Bellan. Consistent large-eddy simulation of a temporal mixing layer laden with evaporating drops. part2. a posteriori modeling. *Journal of Fluid Mechanics*, 523:37–78, 2005.

[49] R. W. Bilger. Conditional moment closure for turbulent reacting flow. *Physics of Fluids*, 5(2):436–444, February 1993.

[50] E. Hawkes and R. Cant. A flame surface density approach to large-eddy simulation of premixed turbulent combustion. *Proceedings of Combustion Institute*, 28:51–58, 2000.

[51] S. B. Pope. *Turbulent Flows*. Cambridge University Press, 2000.

[52] D. K. Lilly. A proposed modification of the Germano subgrid-scale closure method. *Physics of Fluids A*, 4:633–635, 1992.

[53] P. Moin, K. Squires, W. Cabot, and S. Lee. A dynamic subgrid-scale model for compressible turbulence and scalar transport. *Physics of Fluids A*, 3:2746–2757, 1991.

[54] A. T. Hsu, Y.-L. P. Tsai, and M. S. Raju. Probability density function approach for compressible turbulent flows. *AIAA Journal*, 32(7):1407–1415, 1994.

[55] Pratik Donde, Heeseok Koo, and Venkat Raman. A multivariate quadrature based moment method for LES based modeling of supersonic combustion. *Journal of Computational Physics*, 231(17):5805–5821, JUL 1 2012.

[56] Heeseok Koo, Pratik Donde, and Venkat Raman. A quadrature-based LES/transported probability density function approach for modeling supersonic combustion. *Proceedings of the Combustion Institute*, 33(Part 2):2203–2210, 2011.

[57] G. M. Faeth. Evaporation and combustion of sprays. *Progress in Energy and Combustion Science*, 9(1-2):1–76, 1983.

[58] J BELLAN and K HARSTAD. Analysis of the convective evaporation of nondilute clusters of drops. *International Journal of Heat and Mass Transfer*, 30(1):125–136, JAN 1987.

[59] W. A. Sirignano. *Fluid Dynamics and Transport of Droplets and Sprays*. Cambridge University Press, 1999.

[60] RS Miller, K Harstad, and J Bellan. Evaluation of equilibrium and non-equilibrium evaporation models for many-droplet gas-liquid flow simulations. *International Journal of Multiphase Flow*, 24(6):1025–1055, SEP 1998.

[61] MC YUEN and LW CHEN. Heat-transfer measurements of evaporating liquid droplets. *International Journal of Heat and Mass Transfer*,

21(5):537–542, 1978.

[62] M RENKSIZBULUT and MC YUEN. Experimental-study of droplet evaporation in a high-temperature air stream. *Journal of Heat Transfer*, 105(2):384–388, 1983.

[63] S.S. Sazhin, T. Kristyadi, W.A. Abdelghaffar, and M.R. Heikal. Models for fuel droplet heating and evaporation: Comparative analysis. *Fuel*, 85:1613–1630, 2006.

[64] S. Subramaniam and S. B. Pope. Comparison of mixing model performance for nonpremixed turbulent reactive flow. *Combustion and Flame*, 117:732–754, 1999.

[65] S. B. Pope. A Monte Carlo method for the PDF equations of turbulent reactive flow. *Combustion Science and Technology*, 25:159–174, 1981.

[66] S. Subramaniam and S. B. Pope. Comparison of mixing model performance for non-premixed turbulent reactive flow. *Combustion and Flame*, 117:732, 1999.

[67] R. O. Fox. *Computational Models for Turbulent Reacting Flows*. Cambridge University Press, 2003.

[68] J. Villermaux. Micromixing phenomena in stirred reactors. In *Encyclopedia of Fluid Mechanics*, chapter 27. Gulf, Houston, TX, 1986.

[69] K. Akselvoll and P. Moin. Large eddy simulation of turbulent confined coannular jets. *Journal of Fluid Mechanics*, 315:387–411, 1996.

[70] Charles D. Pierce. *Progress-variable approach for large-eddy simulation of turbulence combustion*. PhD thesis, Stanford University, 2001.

[71] Olivier Desjardins, Guillaume Blanquart, Guillaume Balarac, and Heinz Pitsch. High order conservative finite difference scheme for variable density low Mach number turbulent flows. *Journal of Computational Physics*, 227(15):7125–7159, JUL 20 2008.

[72] M. Herrmann, G. Blanquart, and V. Raman. A bounded quick scheme for preserving scalar bounds in large-eddy simulations. *AIAA Journal*, 44(12):2879–2880, 2006.

[73] R. O. Fox. Large-Eddy-Simulation Tools for Multiphase Flows. *Annual Review of Fluid Mechanics*, 44:47–76, 2012.

[74] Nora Okong'o, Anthony Leboissetier, and Josette Bellan. Detailed characteristics of drop-laden mixing layers: Large eddy simulation predictions compared to direct numerical simulation. *Physics of Fluids*, 20(10), OCT 2008.

[75] V. Raman, H. Pitsch, and R. O. Fox. Eulerian transported probability density function sub-filter model for large-eddy simulation of turbulent combustion. *Combustion Theory and Modelling*, 10(3):439–458, 2006.

[76] S. B. Pope. PDF methods for turbulent reactive flows. *Progress in Energy and Combustion Science*, 11:119–192, 1985.

[77] D. Roekaerts. Use of a Monte Carlo PDF method in a study of the influence of turbulent fluctuations on selectivity in a jet-stirred reactor. *Applied Scientific Research*, 48:271, 1991.

[78] H. Mobus, P. Gerlinger, and D. Bruggemann. Comparison of Eulerian and Lagrangian Monte Carlo PDF method for turbulent diffusion flames. *Combustion and Flame*, 124:519–534, 2001.

[79] R. Mustata, L. Valiño, C. Jiménez, WP Jones, and S. Bondi. A probability density function eulerian monte carlo field method for large eddy simulations: application to a turbulent piloted methane/air diffusion flame (sandia d). *Combustion and Flame*, 145(1-2):88–104, 2006.

[80] V. Raman and H. Pitsch. LES/filtered-density-function simulation of turbulent combustion. In *4th Joint Meeting of the U.S. Sections of the Combustion Institute*. The Combustion Institute, Philadelphia, PA, 2005.

[81] V Raman, RO Fox, AD Harvey, and DH West. CFD analysis of premixed methane chlorination reactors with detailed chemistry. *Industrial and Engineering Chemistry Research*, 40(23):5170–5176, NOV 14 2001. 8th Conference on Novel Reactor Engineering for the New Millennium, BARGA, ITALY, JUN 24-29, 2001.

[82] S. B. Pope. Computationally efficient implementation of combustion chemistry using in-situ adaptive tabulation. *Combustion Theory Modelling*, 1:41, 1997.

[83] Y. Z. Zhang and D. C. Haworth. A general mass consistency algorithm for hybrid particle/finite-volume pdf methods. *Journal of Computational Physics*, 194:156–193, 2004.

[84] Metin Muradoglu, Patrick Jenny, Stephen B. Pope, and David A. Caughey. A consistent hybrid finite-volume/particle method for the PDF equations of turbulent reactive flows. *Journal of Computational Physics*, 154:342–371, 1999.

[85] J. Xu and S. B. Pope. Assessment of numerical accuracy of PDF/Monte Carlo methods for turbulent reacting flows. *Journal of Computational Physics*, 152:192–230, 1999.

[86] Y.C. Chen, S.H. Starner, and A.R. Masri. A detailed experimental investigation of well-defined, turbulent evaporating spray jets of acetone. *International Journal of Multiphase Flow*, 32:389–412, 2006.

[87] Y. Baba and R. Kurose. Analysis of flamelet modelling for spray combustion. *Journal of Fluid Mechanics*, 612:45–79, 2008.

[88] C.K. Westbrook and F. L. Dryer. Chemical kinetic modeling of hydrocarbon combustion. *Progress in Energy and Combustion Science*, 10:1–57, 2003.

[89] H. Yamashita, M. Shimada, and T. Takeno. A numerical study on flame stability at the transition point of jet diffusion flames. *Proceedings of the Combustion Institute 26*, 1:27–34, 1996.

[90] A. R. Masri and J. D. Gounder. Turbulent Spray Flames of Acetone and Ethanol Approaching Extinction. *Combustion Science and Technology*, 182(4-6):702–715, 2010.

[91] S. H. Starner, J. Gounder, and A. R. Masri. Effects of turbulence and carrier fluid on simple, turbulent spray jet flames. *Combustion and Flame*, 143(4):420–432, 2005.

[92] Chemical-Kinetic Mechanisms for Combustion Applications, 2011. Mechanical and Aerospace Engineering (Combustion Research), University of California at San Diego (http://combustion.ucsd.edu).

[93] K. Lakshminarasimhan, M. D. Ryan, N. T. Clemens, and O. A. Ezekoye. Mixing characteristics in strongly forced non-premixed methane jet flames. *Proceedings of the Combustion Institute*, 31(Part 1):1617–1624, 2007.

[94] Liuyan Lu and Stephen B. Pope. An improved algorithm for in situ adaptive tabulation. *Journal of Computational Physics*, 228(2):361–386, FEB 1 2009.

[95] W. O'Loughlin and A. R. Masri. A new burner for studying auto-ignition in turbulent dilute sprays. *Combustion and Flame*, 158(8):1577–1590, AUG 2011.

[96] William O'Loughlin and Assaad R. Masri. The Structure of the Auto-Ignition Region of Turbulent Dilute Methanol Sprays Issuing in a Vitiated Co-flow. *Flow Turbulence and Combustion*, 89(1):13–35, JUL 2012.

[97] V. Raman, R. O. Fox, and A. D. Harvey. Hybrid finite-volume / transported PDF simulations of a partially premixed methane-air flame. *Combustion and Flame*, 136:327–350, 2004.

[98] V. Raman and H. Pitsch. Large-eddy simulation of bluff-body stabilized non-premixed flame using a recursive-refinement procedure. *Combustion and Flame*, 142(4):329–347, 2005.

[99] C. D. Pierce and P. Moin. A dynamic model for subgrid-scale variance and dissipation rate of a conserved scalar. *Physics of Fluids*, 10:3041–3044, 1998.

[100] Cecile Pera, Julien Reveillon, Luc Vervisch, and Pascale Domingo. Modeling subgrid scale mixture fraction variance in LES of evaporating spray. *Combustion and Flame*, 146(4):635–648, SEP 2006.

[101] Santanu De and Seung Hyun Kim. Large eddy simulation of dilute reacting sprays: Droplet evaporation and scalar mixing. *Combustion and Flame*, 160(10):2048–2066, OCT 2013.

[102] Colin Heye, Venkat Raman, and Assaad R. Masri. LES/probability density function approach for the simulation of an ethanol spray flame.

Proceedings of the Combustion Institute, 34(1):1633–1641, 2013.

[103] RP Lindstedt and MP Meyer. A dimensionally reduced reaction mechanism for methanol oxidation. *Proceedings of the Combustion Institute*, 29(1):1395–1402, 2002.

[104] Vinayaka N. Prasad, Assaad R. Masri, Salvador Navarro-Martinez, and Kai H. Luo. Investigation of auto-ignition in turbulent methanol spray flames using Large Eddy Simulation. *Combustion and Flame*, 160(12):2941–2954, DEC 2013.

[105] S. Ghosal and P. Moin. The basic equations for the les of turbulent flows in complex geometry. *Journal of Computational Physics*, 118:24–37, 1995.

[106] B. Merci, D. Roekaerts, T. W. J. Peeters, and E. Dick. The impact of the turbulence model and inlet boundary conditions on calculation results for reacting flows. In *Proceedings of the Fifth International Workshop on Measurement and Computation of Turbulent Non-premixed Flames*, pages 226–227, Delft, The Netherlands, 2000.

[107] *Sixth International Workshop on Measurement and Computation of Turbulent Non-premixed Flames*, Sapporo, Japan, 2002.

[108] Colleen M. Kaul and Venkatramanan Raman. Analysis of a dynamic model for subfilter scalar dissipation rate in large eddy simulation based

on the subfilter scalar variance transport equation. *Combustion Theory and Modelling*, 17(5):804–834, OCT 1 2013.

[109] G. Balarac, H. Pitsch, and V. Raman. Development of a dynamic model for the subfilter scalar variance using the concept of optimal estimators. *Physics of Fluids*, 20:035114, 2008.

[110] C. Jimenez, F. Ducros, B. Cuenot, and B. Bedat. Subgrid scale variance and dissipation of a scalar field in large eddy simulations. *Physics of Fluids*, 13:1748, 2001.

[111] Charles D. Pierce. *Progress-variable approach for large-eddy simulation of turbulence combustion*. PhD thesis, Stanford University, 2001.

[112] B. P. Leonard. A stable and accurate convective modelling procedure based on quadratic upstream interpolation. *Computational Methods in Applied Mechanics*, 19:59–98, 1979.

[113] C Rosales and C Meneveau. Linear forcing in numerical simulations of isotropic turbulence: Physical space implementations and convergence properties. *Physics of Fluids*, 17, 2005.

[114] D. You and P. Moin. A dynamic global-coefficient subgrid-scale eddy-viscosity model fro large-eddy simulation in complex geometries. *Physics of Fluids*, 19(6):065110, 2007.

[115] Bart Merci and Eva Gutheil. *Experiments and Numerical Simulations of Turbulent Combustion of Diluted Sprays*. Springer, 2014.

[116] R. J. Adrian. On the role of conditional averages in turbulence theory. In *S. Zahin, G. Patterson (Eds.), Turbulence in Liquids*, Princeton, NJ, 1977. Science Press.

[117] R. J. Adrian. Stochastic estimation of sub-grid scale motions. *Applied Mechanics Reviews*, 43:214–218, 1990.

[118] J. A. Langford and R. D. Moser. Optimal LES formulations for isotropic turbulence. *Journal of Fluid Mechanics*, 398:321, 1999.

[119] P. S. Zandonade, J. A. Langford, and R. D. Moser. Finite-volume optimal large-eddy simulation of isotropic turbulence. *Physics of fluids*, 16(7):2255–2271, 2004.

[120] Robert D. Moser, Nicholas P. Malaya, Henry Chang, Paulo S. Zandonade, Prakash Vedula, Amitabh Bhattacharya, and Andreas Haselbacher. Theoretically based optimal large-eddy simulation. *Physics of Fluids*, 21(10), OCT 2009.

[121] Stephen B. Pope. Self-conditioned fields for large-eddy simulations of turbulent flows. *Journal of Fluid Mechanics*, 652:139–169, JUN 10 2010.

[122] Haifeng Wang and Stephen B. Pope. Lagrangian investigation of local extinction, re-ignition and auto-ignition in turbulent flames. *Combustion Theory and Modelling*, 12(5):857–882, 2008.

[123] Kuochen Tsai and Rodney O. Fox. Modeling multiple reactive scalar mixing with the generalized IEM model. *Physics of Fluids*, 7(11):2820–2830, November 1995.

[124] D. C. Haworth and S. H. El Tahry. Probability density function approach for multidimensional turbulent flow calculations with application to in-cylinder flows in reciprocating engines. *AIAA Journal*, 29:208–218, 1991.

[125] A. R. Masri, S. Subramaniam, and S. B. Pope. A mixing model to improve pdf simulation of turbulent diffusion flames. *Twenty-Sixth Symposium (International) on Combustion*, 26:49, 1996.

[126] J. Janicka, W. Kolbe, and W. Kollmann. Closure of the transport equation for the probability density function of turbulent scalar fields. *Journal of Non-Equilibrium Thermodynamics*, 4:47–66, 1979.

[127] A. W. Cook and W. H. Cabot. Hyperviscosity for shock-turbulence interactions. *Journal of Computational Physics*, 203:379–385, 2005.

[128] S. James, J. Zhu, and M. S. Anand. Lagrangian PDF transport method for simulations of axisymmetric turbulent reacting flows. In *43rd AIAA Aerospace Sciences Meeting and Exhibit*, number 156, 2005.